STAND-OFF DETECTION OF ORGANIC COMPOUNDS ON MARS USING ULTRAVIOLET RAMAN SPECTROSCOPY AND TIME-RESOLVED LASER-INDUCED FLUORESCENCE

EVAN J. ESHELMAN

A DISSERTATION SUBMITTED TO
THE FACULTY OF GRADUATE STUDIES
IN PARTIAL FULFILMENT OF THE REQUIREMENTS
FOR THE DEGREE OF
DOCTOR OF PHILOSOPHY

GRADUATE PROGRAM IN PHYSICS AND ASTRONOMY
YORK UNIVERSITY
TORONTO, ONTARIO
APRIL 2016

Abstract

Recent discoveries of organic carbon and methane on Mars have continued to motivate the search for complex organics on the Martian surface. Instrumentation that directly identifies and characterizes organic carbon is a high priority for the Mars 2020 rover, the successor to the Curiosity rover. Although no Raman instrument has been used in a planetary setting other than Earth, Mars 2020 will contain both SHERLOC, a 248 nm Raman instrument, and a 532 nm Raman system as part of the SuperCam instrument.

A 266 nm Raman spectrometer incorporating time-resolved fluorescence capabilities was developed at York University in order to investigate the performance of an ultraviolet Raman system in detecting organic material on Mars. A range of pure organic compounds, mineral-organic mixtures, and complex Mars analogue rocks from extreme environments on Earth were selected for study. This diverse sample suite allowed investigations that established the detection capabilities of the instrument using controlled samples, and demonstrated the potential for 2D mapping across rough unprepared surfaces to detect traces of organics embedded in a complex mineral matrix. While visible excitation wavelengths suffer from interfering fluorescence that can overwhelm the Raman signal, 266 nm was found to reduce or remove fluorescence in the Raman window in all samples that were tested, increasing the sensitivity to organic carbon.

Many organic compounds exhibit strong fluorescence outside the Raman window when excited with 266 nm radiation. This fluorescence was investigated to determine if it could improve the ability to detect organic material. A method was developed for measuring fluorescence lifetimes with sub-ns precision, and the fluorescence decay profiles of a wide range of aromatic organic molecules were characterized. Incorpo-

rating time-domain capabilities improved both the ability to discriminate between organic compounds and the ability to separate organic from mineral fluorescence.

A 266 nm excitation was found to provide significant fluorescence removal from the Raman spectra of a wide range of unprepared Mars-relevant samples by energetically separating the Raman and fluorescence signals. Incorporating time-resolved fluorescence capabilities was accomplished with minor modification to the instrument, and resulted in an improvement in the ability to detect organic material due to the relative strength of fluorescence emission compared to Raman scattering. The capabilities investigated in this work may be useful when interpreting the measurements that will be returned from the Mars 2020 mission, and for developing the next generation of flight instruments.

Dedication

To my family, for their encouragement and support.

Acknowledgements

I would like to express my great appreciation to my research supervisor Dr. Michael Daly for his guidance and support. Completing this degree was an enriching and rewarding experience, attributable to Dr. Daly's encouragement and dedication to growing the project to its potential. I am particularly grateful as well for the support of my co-supervisor Dr. Gregory Slater, who contributed essential geochemical knowledge, provided an extensive sample suite, and offered use of his own lab facilities to support the project.

I must give special thanks to George Nikolakakos, with whom I had near daily discussions regarding experimental technique, Raman theory, and a range of other topics. George's friendship and support were invaluable in making this degree a fulfilling experience.

I would also like to thank several people without whose support I would likely not have pursued post-graduate studies. Thanks to Dr. Joe Snyder and Dr. Murray Campbell, who both encouraged my career as a physicist, and thanks to Marion and Richard Posner, for always encouraging intellectual growth and creativity.

Finally, I would like to thank my parents, Lisa and Jim, and my sister Anna, for their constant encouragement to pursue this degree and their continued support and inspiration.

Contents

List of Tables

List of Figures

Preface

Sections of the following chapters of this dissertation have been adapted from previously published peer reviewed papers:

Chapter 2,3:

Eshelman, E., Daly, M. G., Slater, G., Dietrich, P. & Gravel, J.-F., An ultraviolet Raman wavelength for the in-situ analysis of organic compounds relevant to astrobiology. Planetary and Space Science 93, 65-70 (2014).

Skulinova, M., Lefebvre, C., Sobron, P., Eshelman, E., Daly, M., Gravel, J.-F., Cormier, J.-F., Châteauneuf, F., Slater, G., Zheng, W., Koujelev, A., Léveillé, R. Time-resolved stand-off UV-Raman spectroscopy for planetary exploration (2014) Planetary and Space Science, 92, pp. 88-100.

Chapter 4:

E. Eshelman, M. G. Daly, G. Slater, P. Dietrich, and E. Cloutis. Time-resolved detection of aromatic compounds on planetary surfaces by ultraviolet laser induced fluorescence and Raman spectroscopy (2015) Planetary and Space Science, 119, pp. 200-207

The results presented in Section 5.5 were obtained through a collaboration with Svetlana Shkolyar and Jack Farmer of the School of Earth and Space Exploration at Arizona State University.

1 Introduction

This thesis concerns the development of an ultraviolet laser spectrometer intended to search for organic compounds on Mars. Designed for a rover platform, the instrument would collect Raman scattered light from targets at stand-off distances of several meters and the resulting spectra would be analyzed to identify and characterize organic material if present. A breadboard ultraviolet system meeting the specifications of a putative flight instrument was constructed at York University and astrobiologically relevant organic samples were selected for study in order to investigate the performance of an ultraviolet excitation. Subsequent work investigated the potential for combining Raman and time-resolved fluorescence measurements in order to maximize the chance for detecting signs of life.

1.1 Summary of major findings

Chapter 1 presents an overview of Raman and fluorescence theory and discusses the history of Mars, covering habitability and discussing organic compounds relevant to astrobiology. The ultraviolet Raman instrumentation developed for this work is discussed in Chapter 2, along with the instrument parameters and data analysis methods used to obtain and analyze Raman spectra.

Chapter 3 presents the fluorescence spectra of several organic compounds obtained at various ultraviolet excitations to determine at what wavelength fluorescence is minimized in the Raman window. A 266 nm excitation was found to result in a strong Raman signal with significant fluorescence reduction. A 266 nm excitation was also found to provide low-fluorescence Raman spectra when examining unprepared surfaces on Mars representative samples containing organics embedded in a complex mineral matrix.

Chapter 4 demonstrates that time-resolved fluorescence measurements, traditionally a laboratory technique, may be adapted to a rover platform intended for Mars organic detection. In addition to measuring fluorescence lifetimes of organics with accuracies under 0.5 ns, short-lived organic fluorescence was able to be separated from long-lived mineral fluorescence, increasing the ability to detect organic carbon.

Chapter 5 builds on the results from Chapter 4, and presents time-resolved fluorescence measurements of a suite of PAHs. Time-domain capabilities were found to increase the ability to distinguish between individual organics, and the results support the incorporation of fluorescence capabilities into ultraviolet Raman instruments. Leveraging the strengths of each technique was found to potentially result in a more rapid and sensitive detection of organic material.

The findings in this work can inform the results obtained by SHERLOC, the combined ultraviolet Raman and fluorescence spectrometer that is part of the Mars 2020 instrument suite, and propose techniques to be incorporated into future flight instruments.

1.2 The search for life on Mars

A potential timeline for the development of life on Mars begins during the Noachian period, which occurred 4.2 to 3.8 billion years ago. During this time Mars had abundant surface water, which altered the geomorphology and chemical environment on a planetary scale [50]. Evidence of this warm and wet period in Mars' history is observable from orbit, in the form of ancient river deltas and channels present in Noachian-age terrain [13]. Exploration of the Martian surface by the Curiosity rover has also revealed evidence of an aqueous past, with the discovery of aqueous minerals and observation of rounded pebbles in an ancient Martian streambed within the base

of Gale crater [34]. Isometric dating of the lowest stratigraphic layer of the crater, a mudstone clay-rich base, supports a formation date in the late Noachian and therefore the presence of abundant surface water during this period [34]. The detection of Fe and Mg-rich phyllosilicates also supports an aqueous past, as these minerals form on Earth in regions with substantial water sources [13].

If life evolved on Mars it may have done so during this period. The abundance of water and clay minerals would have provided the environmental and chemical reservoirs needed to support life [12]. Clay minerals have layering properties that can act as a catalyst, allowing amino acids and other fundamental building blocks of life to organize into more complex compounds. For example, organics including RNA, the precursor to life on Earth, can self-assemble on montmorillonite substrates [13]. While it is unknown what form life on Mars could take, it is assumed to require the same fundamental compounds as on Earth, with C, H, N, O, P, and S content [45].

The early habitable conditions of Mars did not persist. Beginning in the late Noachian and continuing into the Hesperian era from about 3.8 to 3.0 billion years ago, the surface temperature and atmospheric temperature decreased, and the previously abundant surface water was confined to permafrost and polar ice [18, 12]. Evidence of this transitional period is present in the sedimentary record, due to the presence of evaporative sulfate minerals, and due to the quantity of clay minerals that remained on the surface during this period. The fact that clays, which formed during the Noachian remained on the surface in large quantities until the present day indicates that there was less abundant surface water in the time period after their formation [12]. In addition to this mineralogical evidence, geomorphological evidence also supports the transition to a dry and cold planet. Channel and valley formation began to slow during this period, and the remaining channels indicate a source of water consistent with an increasingly arid environment [13]. If life evolved on Mars

it may have been restricted during this transition to environments such as porous sulfates and clays that provided protection against the increasingly inhospitable environment.

Today, in the Amazonian period, the weak atmosphere of Mars results in a significant ultraviolet flux on the surface. Cosmic rays in particular are sufficiently energetic to penetrate two to three meters below the surface, and would destroy trace organics over geological timescales [34]. The relatively low estimation for total carbon content on Mars, between 1 and a few tens of ppm by weight [43], suggests that investigations for organics should occur in the areas that had high habitability potential during periods with abundant surface water, and also currently have high preservation potential for retaining organic material. Locations with ancient sedimentary processes that have been exposed within a few tens of millions of years from the present, including regions with sulfates and clays, are therefore considered high priority astrobiological targets [6, 83]. Today, traces of life or remnants of biosignatures may be preserved in such locations and life may even continue to survive underground or in salty brines[116].

In December 2014 NASA announced the detection of the first organic compounds discovered on the Martian surface [39]. Several chlorinated compounds were identified, including the aromatic chlorobenzene, at a concentration of 150-300 ppb by weight [38], although it is unclear whether chlorine was a component of the in-situ molecules or was added from perchlorates in the soil during the baking procedure in the Sample Analysis at Mars (SAM) oven. Organic compounds do not necessarily require a biological source to form. For example, polycyclic aromatic hydrocarbons (PAHs), composed of aromatic rings and known to form in space [21], are expected on the Martian surface [23]. While amino acids, nucleotides, alkanes, proteins, and PAHs may form through non-biological means, the detection of such compounds can

be an indicator of regions where biological activity is present. More definitive indications of life are termed biosignatures [28]. On Mars, any surface-based life form is presumed to have built-in protection against UV radiation [22], directly in the form of a photoprotective pigment, e.g. parietin, scytonemin, or indirectly in the form of an antioxidant such as a carotenoid, useful to repair damage caused by radiation. Discovery of any of these compounds would be a strong indication of life on the Martian surface [29].

An estimated $2.4 \times 10^5 kg$ of organic material is delivered to Mars from space each year from meteorite impacts, yet this organic material has not yet been observed on the surface. In the absence of a photoprotective pigment, the significant UV surface flux of $2 \times 10^7 erg - m^{-2} yr^{-1}$ would degrade this organic material over time. Studies of simple PAHs have shown that such organic compounds, considered relatively stable due to the six-carbon ring structure, have a half-life of only a few hours under radiation conditions similar to Mars [23]. In addition, ultraviolet radiation can interact with the small amount of water that exists in the Martian atmosphere, possibly resulting in hydrogen peroxide, NaO, and CaO_2. These oxidants would degrade many organic compounds swiftly. Models incorporating the ultraviolet flux and oxidation processes, suggest that there is sufficient attenuation in the subsurface to allow the preservation of organic material on geological timescales at a depth of only two to three meters [31].

Whether or not life exists in the universe on planets other than Earth is one of the top-level questions driving space exploration. If life did evolve on Mars, it is possible that traces of that life may be preserved today in settings accessible to planned and future landed missions. The exploration of Mars, from orbiters to landers and rovers, has increasingly produced evidence that Mars had not only an aqueous past, but also the conditions and chemical energy reservoirs necessary to support

life. Consequently, upcoming exploration objectives will transition from searching for habitable environments to directly searching for traces of organic compounds and possible biosignatures within those environments.

1.3 Review of organic compounds relevant to astrobiology

While the search for life on Mars is based on evidence of past habitability, current habitable environments, and indications of organics on the surface, Martian astrobiology is still a speculative field. Organic compounds can be divided into several categories according to their presumed likelihood on Mars, working under the assumption that life on Mars is carbon based, and that it contains the same fundamental building blocks as life on Earth. A summary of organic compounds organized by astrobiological relevance and complexity is presented in Table 1. The term 'organic compound' has no strict definition, however the term most commonly refers to chemical compounds containing carbon, or compounds containing at least one C-H bond. Organics are relevant to astrobiology as all known forms of life on Earth are composed of and require organic compounds. Other forms of life, e.g. silicon-based, are not considered strong candidates for non-terrestrial life due to various physical limitations.

1.4 Raman theory

Raman spectroscopy is a laser-based technique that provides information concerning the molecular bonds in a sample with the term 'Raman' referring to the manner in which a photon exchanges energy with a molecule during an interaction. As the energy of a photon is proportional to its frequency, a photon that is inelastically scattered (Raman scattered) from a molecule will have a shift in frequency due to the loss in energy. This process contrasts with elastic (Rayleigh) scattering where no

Type	Example molecules	Description
Building blocks of life, e.g. (a) PAHs, (b) fatty acids, (c) nucleobases, (d) amino acids	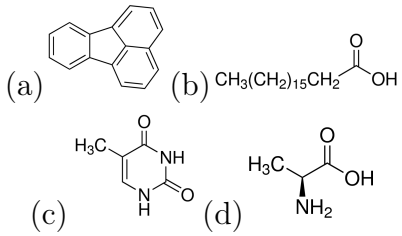	Simple organics can form in space and are present in some types of meteorites including carbonaceous chondrites. The estimated flux of organic material on Mars due to meteorite impacts is $2.4 \times 10^5 kg$ per year.
Geologically stable organics	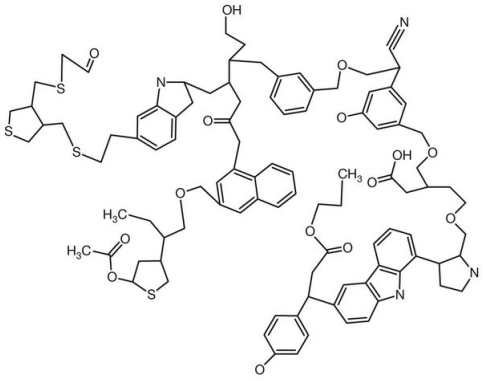	If Mars hosted life at some point in the past, remnants of that life may be preserved today in forms similar to kerogens, shale, or other geologically stable clusters of amorphous carbon rings.
Possible biosignatures	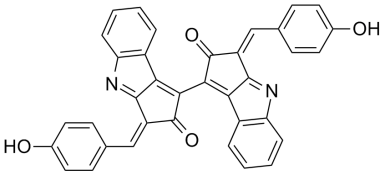	Some molecules, including chlorophyll and scytonemin, would provide stronger evidence of active life on Mars today. These include molecules that would enable bacteria to survive in the harsh Martian climate.
Microorganisms, endoliths	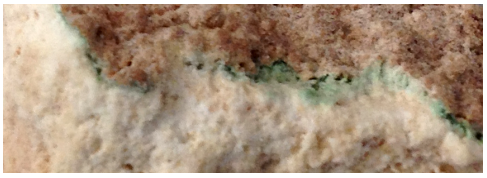	Life on Mars, if present today, may take the form of bacteria evolved to survive the dry, cold, and radiative environment. Endolithic microbes on Earth are possible analogues to this type of life.

Table 1: Organic compounds arranged by approximate astrobiological relevance and complexity.

energy is exchanged and the scattered photon has the same frequency as the incident photon. As the laser wavelengths typically selected for Raman instrumentation are not energetic enough to promote electrons to excited electronic states, the energy exchange results in a transition to some vibrational mode of the ground electronic state of the molecule. A Raman spectrum therefore consists of sharp peaks at locations that correspond to the energies of vibrational frequencies, and offers a 'fingerprint' of the particular compound under observation, whether that compound is in a solid, liquid, or gaseous state. Typically, molecules at rest at room temperatures and below are in the ground vibrational mode, and therefore the exchange in energy will result in a transition to a higher vibrational mode (usually the first vibrationally excited mode), and the scattered photon will have an energy that is less than the incident photon, termed 'Stokes' scattering. In cases where the molecule is initially in an excited vibrational state, a transition can occur where the scattered photon will have more energy than the incident photon, and is termed 'anti-Stokes' scattering.

Raman scattering was first observed by Sir C. V. Raman in 1928, five years after the effect had been proposed in 1923 by Adolf Smekal. Raman, along with K. S. Krishnan, published a short article titled 'A New Type of Secondary Radiation' in a 1928 edition of the journal *Nature*, and stated:

> *... we should expect ... in the case of ordinary light two types of scattering, one determined by the normal optical properties of the atoms or molecules, and another representing the effect of their fluctuations from their normal state* [79].

Raman was able to observe this new type of scattering by focusing sunlight onto a liquid sample and employing color filters to detect the 'modified' scattered radiation, as it was termed. The article also noted the significantly lower intensity of the in-

elastic scattering compared to other known luminescence mechanisms. The relative weakness of Raman scattering, with cross sections that can be four to six orders of magnitude less than either Rayleigh scattering or fluorescence, restricted application of the technique until high-powered lasers and sensitive detectors became available in the mid-to-late 20th century.

Raman shift is measured with the non-SI unit of wavenumber, or cm^{-1}, and is often notated with ν. As the important quantity is the degree to which the scattered light is shifted from the incident light, the excitation wavelength is conventionally assigned a wavenumber of 0 cm^{-1}, and the Raman shift is then defined as a change in wavenumber from the incident wavelength. The intensity axes of Raman spectra are often normalized or presented in arbitrary units, as measurements of absolute scattering cross sections are challenging and influenced by many experimental variables.

As Raman scattering is due to vibrations induced in a molecule or crystal lattice, the number of Raman bands in a spectrum will be closely tied to the number of possible vibrations allowed by the molecular structure. As atoms exhibit three degrees of freedom in space, a molecule will exhibit 3N degrees of freedom, where N is the number of atoms in the structure. Subtracting translational and rotational degrees of freedom, molecules will therefore exhibit 3N-5 or 3N-6 vibrational modes, depending on the linearity of the structure. The simplest cases are diatomic homonuclear molecules such as O_2 or N_2, which have one possible vibration along the bond axis. As an example, Equation 1, the classical formula for two masses joined by a spring, may be applied as a simple model to determine the vibrational frequency ν of a diatomic system using the force constant K and the reduced mass of the system μ, where the reciprocal of the reduced mass is equal to the sum of the reciprocal masses of the two atoms involved.

$$\nu = \frac{1}{2\pi}\sqrt{K\left(\frac{1}{\mu}\right)} \tag{1}$$

For oxygen and nitrogen, using masses of 14 *amu* and 16 *amu* respectively, and force constants of 10 $mdyne/\mathring{A}$ and 20 $mdyne/\mathring{A}$ respectively (the approximate force constants for double and triple bonds), vibrational frequencies of about 1450 cm^{-1} for oxygen and 2200 cm^{-1} for nitrogen may be obtained. This rough approximation is close to the experimental values of 1550 $cm^{-1}$and 2320 cm^{-1} for diatomic oxygen and nitrogen respectively. In this example, the difference between the calculated and observed band positions is due to the approximate values of the force constants, not the assumption of classical oscillation of the system.

A sample Raman spectrum of gypsum ($CaSO_4 \cdot 2H_20$) is presented in Figure 1. This spectrum is what could be expected from an instrument observing a gypsum vein on the Martian surface. Wavenumber, or Raman shift, is plotted against intensity. Each peak corresponds to a certain molecular vibration in the gypsum. The Raman active vibrations in gypsum are due to bending and stretching of the sulfate ion [8], as well as stretching of the O-H bonds in the chemically bound water. There are six Raman bands located at 1144, 1019, 681, 623, 501, and 422 cm^{-1}, as well as two bands above 3000 cm^{-1} (not shown). These peaks may be assigned to vibrations, shown in Figure 1, using the qualitative rules that bending vibrations typically occur at lower energies than stretching vibrations, and X-H vibrations (e.g. C-H, O-H, and N-H) occur at higher wavenumbers than other types of bond stretches [60].

Figure 1 also contains a table with a conventional description of the Raman-active vibrations of the system. The symmetry of each vibration is denoted by a Mulliken symbol. For the purposes of vibrational spectroscopy, the Mulliken symbols relate to degeneracy, with A denoting singly degenerate modes, E denoting doubly degenerate

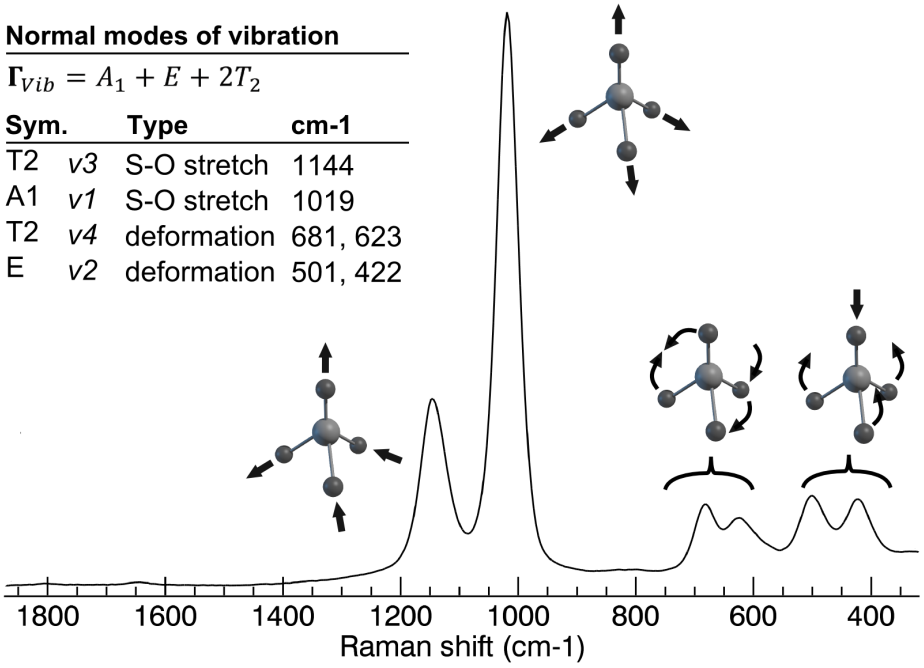

Figure 1: Raman spectrum of an example Raman spectrum (gypsum) including a table of Mulliken symbols and molecular vibration diagrams.

modes, and T denoting triply degenerate modes. Raman vibrations can often be accompanied by additional labels denoted by v followed by a subscript, and denote fundamental vibrations.

While a full theoretical overview of the Raman effect is beyond the scope of this work, it is useful to provide a brief discussion of the aspects of theory that are useful for an experimentalist - namely, the physical origins of spectral features including peak positions, intensities, polarizations, and how these features relate to molecular bonds in a sample.

1.4.1 Origin of Raman scattering

The resulting motion of a molecule in the presence of a laser beam is due to the electron cloud deforming with a frequency equal to the laser frequency, modulated by much slower nuclear motion (vibration) in response to the distorted cloud of electric charge. The electron cloud in the molecular system acts as a dipole with the charge across the molecule varying in time, and the total oscillation of the molecule will contain several frequencies. In addition to an oscillation with a frequency equal to the incident electric field (corresponding to Rayleigh scattering), for each possible vibrational mode there will be an additional pair of frequencies corresponding to Stokes and anti-Stokes Raman scattering. A brief derivation of these frequencies is presented in the remainder of this section. Throughout this work scalar quantities are indicated by non-bold symbols, and vectors and tensors by bold symbols.

The strength of the induced electric dipole $\boldsymbol{p}$ of a molecule when it is exposed to an external electric field is equal to the product of the incident electric field vector $\boldsymbol{E}$ and the molecular polarizability, given by the polarizability tensor $\boldsymbol{\alpha}$, shown in Equation 2.

$$\boldsymbol{p} = \boldsymbol{\alpha} \cdot \boldsymbol{E} \tag{2}$$

This polarizability is a function of the geometry of the molecule, and can therefore be expressed in terms of normal coordinates. Expanding the polarizability tensor in a Taylor series results in Equation 3 for a given polarizability tensor coordinate L and normal mode k for a normal coordinate Q_k. The subscript L of $\boldsymbol{\alpha}$ refers to the tensor components, which can be written in Cartesian coordinates as a second-rank tensor to describe the interaction between the polarizability and the incident electric field. The tensor treatment allows the interaction of the two vectors involved (the electric

field and the polarizability) to be calculated regardless of their relative orientations or symmetries. The sum over k occurs over all vibrational modes, for example in a diatomic molecule k would equal one and the sum would reduce to a single term. Q_k describes the normal coordinate in terms of the magnitude of the normal coordinate modulated during nuclear motion, shown in Equation 4. The total polarizability is the sum of the polarizability at equilibrium and a term containing polarizability derivatives with respect to normal coordinates, describing the change in polarizability of the molecule during vibration. It is this second term from which the Raman tensor is derived. Higher order terms are ignored, which is justified by an assumption of harmonic motion of the oscillator [62]. Higher powers of the series are important when incorporating effects from Fermi resonances and determining allowed overtone transitions, but they are neglected here for simplicity.

$$\alpha_L = (\alpha_L)_0 + \sum_k \left(\frac{\partial \alpha_L}{\partial Q_k}\right)_0 Q_k + \dots \tag{3}$$

The second term contains what is known as the polarizability derivative tensor. As the value of Q_k changes with time over the course of vibration, Q_k may be written as

$$Q_k = Q_{k0} \cos(\omega_k t + \delta_k) \tag{4}$$

where ω_k is the frequency of nuclear motion, Q_{k0} is the polarizability at rest, and δ_k is the phase of the vibration. Similarly, the electric field vector $\boldsymbol{E}$ also has a frequency dependence and changes in time as

$$\boldsymbol{E} = \boldsymbol{E}_0 \cos(\omega_1 t) \tag{5}$$

where ω_1 is the frequency of the electric field. Combining Equations 3 and 2 and inserting the two relations above results in an expression for the polarizability of the vibrations molecule of the form

$$\boldsymbol{p} = \boldsymbol{\alpha}_0 \boldsymbol{E}_0 \cos(\omega_1 t) + \left(\frac{\partial \alpha_L}{\partial Q_k}\right)_0 \boldsymbol{E}_0 \cos(\omega_1 t)\, Q_{k0} \cos(\omega_k t + \delta_k) \tag{6}$$

Equation 6 may be rewritten as the sum of three electric dipole vectors that are functions of three distinct frequencies.

$$\boldsymbol{p}_{\text{tot}} = \boldsymbol{p}_{\text{Rayleigh}}(\omega_1) + \boldsymbol{p}_{\text{anti-Stokes}}(\omega_1 + \omega_k) + \boldsymbol{p}_{\text{Stokes}}(\omega_1 - \omega_k) \tag{7}$$

The physical principle that allows for Raman scattering (from a classical perspective) is the fact that an oscillating dipole will emit radiation in the form presented in Equation 8

$$I \propto N I_0 w_1^4 p^2 \sin(\theta) \tag{8}$$

where N is the number of molecules observed, I_0 is the intensity of the incident radiation, ω_1 is the frequency of the incident radiation, p is the amplitude of the dipole, and θ is the angle that the incident light makes with the axis of the dipole. The three dipole vectors in Equation 7 will therefore result in Rayleigh scattered radiation, as well as Stokes and anti-Stokes Raman scattering. Raman intensities will be non-zero when the derivative of the polarizability at the equilibrium position is non-zero, a requirement known as the Raman selection rule.

Several additional observations may be made from Equation 8 that relate directly to observed properties of Raman scattering. The strength of the Raman scattering depends on how well aligned the incident electromagnetic field produced by the laser

is with the axis of the deformation of the electron cloud (the dipole axis). This insight may be experimentally observed in the Raman spectra of some crystals, where vibrations can propagate as phonons due to the ordered structure. Changing the orientation of the crystal relative to the laser can change the relative heights of the Raman peaks that are observed [8]. This effect is not often seen in organic material, as the many organic molecules within the field of view of a Raman instrument are usually randomly (isotropically) oriented relative to the laser. A second observation is that the intensity of the Raman scattering is non-linearly dependent on the frequency of the incident radiation. An excitation of 266 nm produces Raman scattering with 16 times the intensity compared to an excitation of 532 nm.

1.4.2 Assigning Raman bands to vibrations

For simple molecules, or molecules that can be subdivided into smaller functional groups, assigning Raman bands to molecular vibrations can be accomplished qualitatively if the type of vibration (e.g. stretching, bending, torsion) can be determined. This can be accomplished using group theory, a technique that takes advantage of molecular symmetry to simplify the calculation of normal modes of a molecule. By considering the symmetry of a molecule, the number of possible vibrations can be calculated and qualitatively arranged according to the vibration type and matched to an experimentally obtained Raman spectrum. A sample Raman spectrum of the amino acid L-alanine is presented in Figure 2. The Raman region between approximately 1000 and 1800 cm^{-1}can contain a large number of characteristic bands due to organic molecules, and no vibrations due to minerals are typically observed in this region.

To explicitly and quantitatively calculate the frequencies of each vibration in cm^{-1}, group theory is insufficient and an approach may be applied developed by E. Wilson,

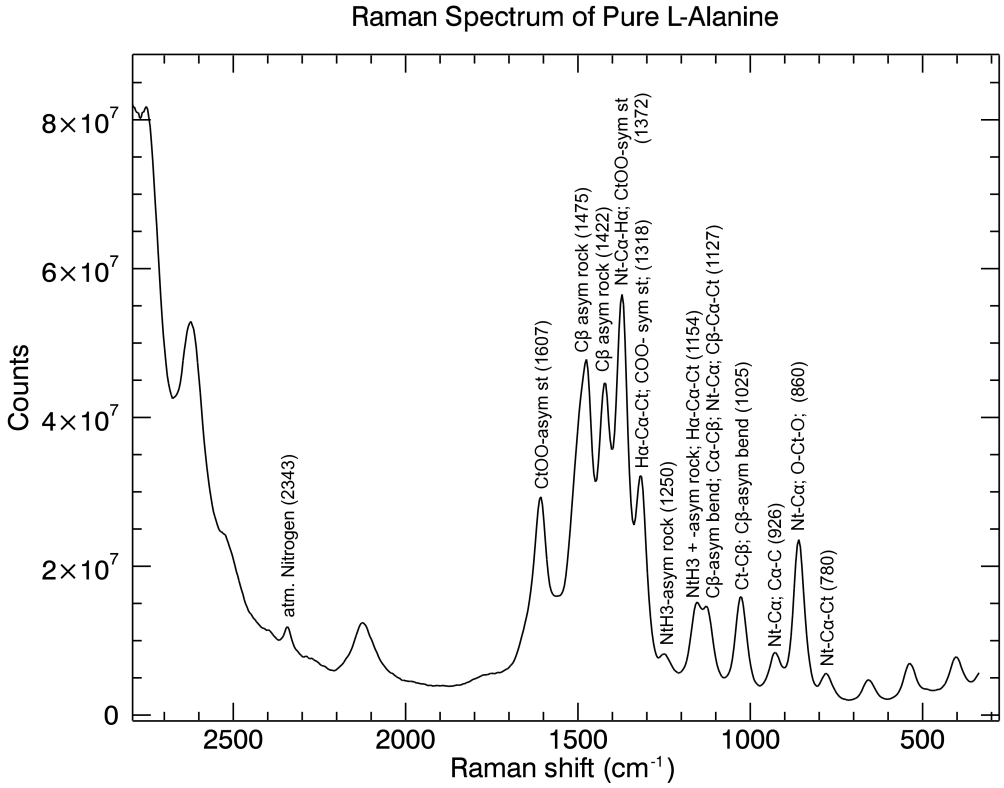

Figure 2: Raman spectrum of the amino acid L-alanine, showing the diversity of information in the organic fingerprint region between 1000 and 1600 cm^{-1}.

termed the FG method [114]. The FG method uses a classical oscillator model to decouple the vibrations of a molecule into separate motions, with the number of oscillators equal to $3N - 6$, the number of vibrations. A decoupling approach is necessary as it is not possible to simply apply a harmonic oscillator relation to every set of connected atoms in a molecule due to the influence on the motion by the neighboring atoms in the molecule. The FG method is applied by constructing two matrices, an **F** matrix containing a description of the potential energy of the system, and a **G** matrix describing the kinetic energy of the system. In order to decouple the vibrations, these matrices must be constructed in terms of symmetry coordinates. Symmetry coordinates are combinations of internal coordinates (coordinates given to stretching and bending motions of the atoms in a molecule) chosen such that the combination results in a coordinate with one of the symmetries of the point group to which the molecule belongs.

The F and G matrices may then be constructed as

$$\mathbf{F} = \mathbf{U}\mathbf{f}\mathbf{U}^{'} \tag{9}$$

and

$$\mathbf{G} = \mathbf{U}\mathbf{g}\mathbf{U}^{'} \tag{10}$$

where the elements of **U** are composed of the coefficients of all symmetry coordinates corresponding to a certain Mulliken symbol. The matrix **f** is an $n \times n$ matrix containing force constants of the system, analogous to K in Equation 1, where n is the number of internal coordinates. The matrix **g** is also an $n \times n$ matrix, where the elements of **g** contain information regarding the kinetic energy and depend on the atomic masses and lengths of the involved atomic bonds at rest, as well as the geome-

tries of the atoms involved in the interaction between the two internal coordinates. As atomic masses and bond lengths are well known, and the number of atoms involved in the interaction generally fall into a limited number of permutations, the elements of the **g** matrix can usually be obtained from tables available in the literature.

With complete **F** and **G** matrices, the vibrational frequencies for all modes of a certain Mulliken symbol can be determined by calculating a secular determinant of the form in Equation 11.

$$|\mathbf{GF} - \mathbf{I}\lambda| = \begin{vmatrix} \sum_l \mathbf{G}_{1l}\mathrm{F}_{l1} - \lambda & \sum_l \mathbf{G}_{1l}\mathbf{F}_{l2} & \dots & \sum_l \mathbf{G}_{1l}\mathbf{F}_{ln} \\ \sum_l \mathbf{G}_{2l}\mathbf{F}_{l1} & \sum_l \mathbf{G}_{2l}\mathbf{F}_{l2} - \lambda & \dots & \sum_l \mathbf{G}_{2l}\mathbf{F}_{ln} \\ \dots & \dots & \dots & \dots \\ \sum_l \mathbf{G}_{nl}\mathbf{F}_{l1} & \sum_l \mathbf{G}_{nl}\mathbf{F}_{l2} & \dots & \sum_l \mathbf{G}_{nl}\mathbf{F}_{ln} - \lambda \end{vmatrix} \tag{11}$$

The secular determinant will have the form of an n order polynomial, where n is the number of vibrations that share the Mulliken symbol used to form the **U** matrix. The roots of the polynomial, λ, are the vibrational frequencies where the wavenumber ν is related to λ by

$$\lambda = 4\pi^2 c^2 \nu^2. \tag{12}$$

Equations 9 - 12 may be repeated for each **U** matrix, resulting in a complete set of vibrational frequencies for the molecule. In principle, this is a straightforward method to calculate Raman frequencies. However, the application of this method is limited by the difficulty in obtaining the force constants needed to construct the **f** matrix. Calculating force constants requires computer modeling using either density functional theory or other *ab-initio* methods, incorporating quantum mechanical models of electronic states. Force constants may be measured by working backwards

from the experimentally measured positions of Raman bands, but if the spectrum is unknown or complex it will not be clear which force constant should be attributed to which vibration. In practice, most force constants, and therefore most elements of the **f** matrix, will be assumed to be zero, as the atomic motion during a vibration will be most influenced by the closest few neighboring atoms, and relatively unaffected by atoms further away, and a computer (or supercomputer) will be used to calculate the few force constants assumed to be most impactful to the system.

The classical theory of Raman scattering correctly predicts the frequency dependence of Raman scattering, as well as the dependence on the derivative of the polarizability tensor. However, a quantum mechanical model is required to determine the vibrational frequencies. In the quantum mechanical model, the classical normal coordinate amplitude is quantized, and the derivative of the polarizability is related to the vibrational frequencies of the molecular system [62].

1.4.3 Raman intensities and depolarization ratios

To calculate Raman intensities, it is desirable to express the components of the polarizability derivative tensor in Equation 3 in cartesian coordinates, used by most computer modeling software . Converting from normal coordinates to cartesian coordinates, the Raman tensor for a normal mode k is given by Equation 13 [81].

$$\hat{\boldsymbol{R}}_k = \frac{\partial \alpha_L}{\partial Q_k} = \frac{1}{\sqrt{\mu_k}} \sum_{n=1}^{3N} \phi_n^k \left(\frac{\partial \alpha_L}{\partial \xi^n} \right) \tag{13}$$

where μ_k is the reduced mass of the mode, and ϕ_k^n is the physical displacement of the atoms during the vibration. Cartesian coordinates are indicated by ξ^n. An example of this expansion is provided below for the S atom in the sulfate ion

$$\hat{\boldsymbol{R}}_k = \frac{1}{\sqrt{\mu_k}} \left[S_x \left(\frac{\partial \alpha}{\partial x_S} \right) + S_y \left(\frac{\partial \alpha}{\partial y_S} \right) + S_z \left(\frac{\partial \alpha}{\partial z_S} \right) + \ldots \right] \tag{14}$$

The reduced mass, polarizability derivative tensor components, and geometric displacements are all accessible in the output of calculations performed by most modeling programs. From the Raman tensor the Raman activity, which is proportional to intensity, and the depolarization ratio of the band may be calculated using the tensor invariants. The depolarization ratio describes the ratio between the components of the scattered radiation that are emitted with perpendicular and parallel polarizations compared to the incoming radiation. The two Raman tensor invariants of interest are the reduced matrix trace α and the anisotropy γ, where α_{ij} are components of $\hat{\boldsymbol{R}}_k$.

$$\bar{\alpha} = \frac{1}{3} \left[\alpha_{xx} + \alpha_{yy} + \alpha_{zz} \right] \tag{15}$$

$$\bar{\gamma^2} = \frac{1}{2} \left[\left(\alpha_{xx} - \alpha_{yy} \right)^2 + \left(\alpha_{yy} - \alpha_{zz} \right)^2 + \left(\alpha_{zz} - \alpha_{xx} \right)^2 \right] + 3 \left[\alpha_{xy}^2 + \alpha_{xz}^2 + \alpha_{yz}^2 \right] \tag{16}$$

Solving for α and γ and converting to angstroms yields the Raman activity R_k in units of $\mathring{A}^4/amu$, and depolarization ratio ρ, following the two relations in Equations 17 and 18. The Raman activity describes the intensity of Raman scattering averaged over all orientations of the molecule, and is proportional to absolute differential cross-section, given in units of cm^2/sr. The conversion to cross-section is described by Ru et al. [81].

$$R_k = \frac{45\bar{\alpha}^2 + 7\bar{\gamma}^2}{45} \tag{17}$$

$$\rho_k = \frac{3\bar{\gamma}^2}{45\bar{\alpha}^2 + 4\bar{\gamma}^2} \tag{18}$$

1.5 Fluorescence lifetime theory

When a photon is incident on a molecule, there are several possible types of interactions in addition to Raman scattering that can occur with different probabilities. These interactions are shown in Figure 3. As previously discussed, the photon may be elastically scattered, in which case there is no shift in the frequency of the photon. The photon may also be absorbed by the molecule. This occurs when the incident photon has sufficient energy to promote an electron to a higher energy orbital in the molecule. In this case, no scattering occurs. After a period of time, this electron can return to the ground electronic state, emitting a photon in the process. The pathways which result in the various interactions are summarized in Table 2.

While Rayleigh scattering occurs at the excitation wavelength, fluorescence emission is Stokes-shifted to longer wavelengths, the emission bands are often very broad, spanning tens of nanometers. The cross section of fluorescence is much greater than the cross section for Raman scattering, and even relatively weak fluorescence can overwhelm Raman spectra. Nearly all laser induced fluorescence occurs above 270 nm, due to the types of transitions involving bonding and non-bonding electrons that can occur with typical laser photon energies. X-ray fluorescence can result from exciting inner-shell electrons, but x-ray lasers are necessary to drive this process. As the Raman window will move with the laser wavelength, an ultraviolet excitation below 270 nm can remove nearly all fluorescence from the Raman window. Strong fluorescence will still be generated by the ultraviolet laser pulse, but will be located outside of the Raman window.

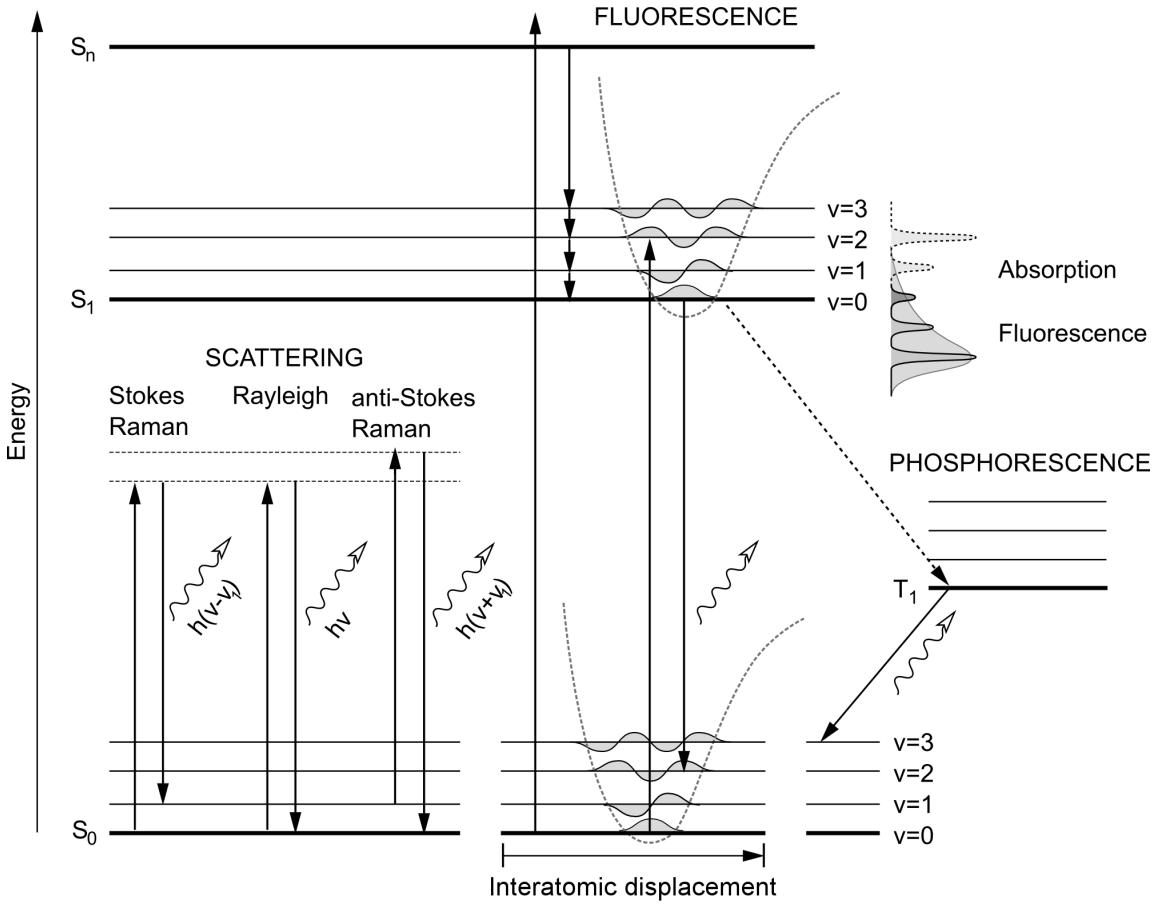

Figure 3: Jablonski diagram depicting the luminescence mechanisms of Raman and Rayleigh scattering, fluorescence, and phosphorescence. Depictions of the nuclear wavefunctions involved in absorption and fluorescence are overlaid on the fluorescence transitions.

Interaction	Mechanism	Timescale
Rayleigh (scattering)	The molecule is promoted to a virtual state and returns to the ground state without a change in frequency	fs-ps
Raman (scattering)	The molecule is promoted to a virtual state and quickly returns to an excited vibrational state (typically the first excited state) with a change in frequency	fs-ps
Fluorescence (luminescence)	The molecule is promoted to an excited electronic state by a photon of sufficient energy. Internal conversion (possibly by overlapping excited state vibrational levels) results in a fast conversion to the ground vibrational level of the first excited state. After some time the molecule returns to the ground electronic state emitting a photon. As energy is lost due to internal conversion, fluorescence occurs at lower energies than the incident photon.	ns
Phosphorescence (luminescence)	The molecule is promoted to an excited electronic state by a photon of sufficient energy. A rare event occurs where the electron spin becomes aligned with the ground state electron, and therefore the transition back to the electronic ground state becomes forbidden. Phosphorescence lifetime can be as long as minutes or hours.	>ms

Table 2: Summary of luminescence mechanisms

1.5.1 Origin of exponentially decaying emission

A significant component of this work involves investigating the potential for a dual Raman and fluorescence instrument. The properties of the instrument, discussed later, additionally allow for ns-scale time-resolved measurements. This time resolution is sensitive enough to measure the fluorescence decay for many organic and mineral compounds. Fluorescence spectra are simpler than Raman spectra visually, however the interpretation of fluorescence features and decay lifetimes is not straightforward. This section provides an overview of the origin of the exponential decay observed from fluorescing molecules, and discusses several variables that can affect fluorescence. This overview is intended to provide some context to the possible benefits and limitations of applying a technique in-situ on a planetary surface that has been traditionally restricted to controlled laboratory environments.

Fluorescence from molecules can be treated similarly to fluorescence from single atoms [97]. In single atoms, the probability of spontaneous emission from an excited state to the ground state, derived by Einstein in 1917, is a random process with a rate governed by

$$\frac{1}{\tau_0} = A_{u\to l} = C\tilde{v}_{ul}^2 \int \epsilon d\tilde{v} \tag{19}$$

Where $A_{u\to l}$ is the Einstein coefficient for spontaneous emission from an upper to lower state, which is equivalent to the inverse of the lifetime τ_0. $\tilde{v}_{ul}$ is the frequency of the transition in wavenumbers, and ϵ is the molar extinction coefficient. The rate of spontaneous emission is proportional to the strength of the absorption, calculated by integrating ϵ over the absorption band. Strickler and Berg proposed a modification to this formula in 1962 [97] that considered broad bands, such as those seen in molecular systems.

$$\frac{1}{\tau_0} = A_{u0\to l} = C\left\langle \tilde{v}_f^{-3}\right\rangle_{\mathrm{Av}}^{-1} \int \frac{\epsilon}{\tilde{v}} d\tilde{v} \tag{20}$$

The term $\left\langle \tilde{v}_f^{-3}\right\rangle^{-1}$ replaces the atomic emission wavenumber, and is an average value of the emission spectrum, while the integral occurs over the absorption spectrum of the molecule. As fluorescence nearly always occurs from the first excited state S_1 to the ground state S_0, features in the absorption spectrum arising from transitions to higher energy states are ignored in the calculation. The factor C contains a number of constants, $8 \times 2303\pi cn^2 \Re^{-1} \frac{g_l}{g_u}$, including the speed of light, the index of refraction, Avogadro's number, and the degeneracies of the states respectively. These factors are condensed here to highlight the differences between atomic and molecular fluorescence.

Equation 20 reduces to Equation 19 if the transition is sharp, as expected in atomic fluorescence. If the transition is sharp, $\tilde{v}$ is a constant and the denominator can be removed from the integral. By comparing these two equations the similarities between atomic and molecular fluorescence decay can be seen. Similar to atomic fluorescence, the lifetime decay of molecules is not an independent quantity, but may be calculated from the experimentally obtained absorption and emission spectra.

It can be seen that the strength of the absorption (the integrated absorption) is inversely related to the lifetime. Strongly absorbing molecules will exhibit shorter lifetimes. In application, this equation works well for certain classes of molecules, and is less well suited for others. Polycyclic aromatic hydrocarbons (PAHs) are well described by this formula, and tend to have lifetimes in the 1 to 10 ns range [97], however this relation has been observed to not hold as accurately if the PAH contains substitutions or side groups. The relation can also fail in application as it does not account for changes in the geometry of the excited state, or interactions with

a solvent or the local environment. Molecular fluorescence is complicated by both the complexity of the molecule and the interaction with surrounding molecules, but Equation 20 can be applied as an approximate first-order description of the origin of the exponential decay that is observed from fluorescing molecules.

1.5.2 Factors affecting fluorescence lifetimes

The measured fluorescence lifetime will almost never agree with the value calculated from Equation 20 except under the strictest of experimental conditions. The measured fluorescence lifetime, τ_m, is affected by any mechanism that will allow for the radiationless transition of energy to the ground state. These non-radiative mechanisms are called quenching factors, and the measured lifetime is related to the sum of all non-radiative pathways by Equation 21.

$$\tau_0 = \frac{\tau_m}{Q} \tag{21}$$

Q is the quantum yield, the ratio of emitted to absorbed photons, which will be reduced from a maximum value of 1.0 by any non-radiative pathways available to depopulate the excited state [59]. Many types of interactions can result in quenching, with implications for lifetime measurements performed in-situ. Collisional quenching can occur if the molecule comes into contact with another molecule. For example, a common quencher of nearly all fluorescence is oxygen which can reduce measured fluorescence lifetimes [59]. As the Martian atmosphere is thin and contains a low concentration of oxygen relative to Earth, about 0.1%, the difference in oxygen content may be sufficient to result in changes in the fluorescence lifetimes of longer-lived compounds. Another possible source of quenching when investigating samples in-situ is resonance energy transfer (RET). If the energy levels of two adjacent molecules

overlap, a dipole-dipole coupling can result in a radiationless decay pathway for any excited electrons in a molecule of interest. Measurements performed on a planetary surface on a relatively uncharacterized and complex sample would likely have to account for an unpredictable quenching environment.

1.5.3 $\pi \rightarrow \pi^*$ transitions

For many organic compounds, including aromatic compounds and compounds with conjugated carbon chains, the gap between the highest occupied molecular orbital (HOMO) and the lowest unoccupied molecular orbital (LUMO) occurs between a π bonding orbital and a π^* antibonding orbital, each composed of two atomic p orbitals. The π orbital has a lower energy and is involved in the molecular bond, while the π^* orbital has a higher-energy and contains an orbital node between the involved atoms, weakening the bond. These transitions generally have high absorption coefficients, and therefore tend to fluoresce strongly [23]. Some molecules, particularly substituted aromatics, can have lower energy gaps between a non-bonding electron and an antibonding state, and therefore an $n - \pi^*$ transition can be the cause of fluorescence, or can be excited alongside a $\pi - \pi^*$ transition. These transitions have lower absorption coefficients, and can produce weaker fluorescence. The energy gap for $\pi - \pi^*$ and $n - \pi^*$ transitions in aromatics may be overcome by ultraviolet excitation, and therefore many aromatics can strongly absorb in the ultraviolet and produce strong fluorescence. For compounds containing conjugated carbon chains, the energy gap for the $\pi - \pi^*$ decreases as the length of the carbon chain increases. A four-carbon chain consisting of conjugated π bonds will have a peak absorption around 215 nm, a six-carbon chain will absorb around 260 nm. Beta-carotene contains an 11-carbon chain with conjugated bonds, and absorbs around 470 nm.

1.6 Ultraviolet absorption

As absorption of a photon is a competing process with Raman scattering, compounds that absorb in the ultraviolet can exhibit weaker Raman scattering, as absorption of photons will result in less available Raman scatterers. If a compound exhibits significant absorption at the excitation wavelength, there will be a non-linear relationship between the Raman intensity and concentration. Equation 22 presents the Beer-Lambert law describing the intensity $I(l)$ of a laser as a function of the distance penetrated l into a sample.

$$I(l) = I_0 e^{-2.303(l\epsilon_0 C)} \tag{22}$$

The intensity decreases from the initial intensity I_0, dependent on the extinction coefficient ϵ_0 and the concentration of the sample C. At high absorption values, less radiation will penetrate into the sample. For Raman scattering collected with a backscatter geometry, as is used in this work, Equation 22 can be extrapolated to calculate the Raman backscatter intensity expected from a sample that contains a strongly absorbing species. This result, originally derived by D. Shriver et al. [87] and reformulated by Wo et al.[115], is presented below in Equation 23.

$$I_x = \frac{I_0 J_x C_x}{2.303C(\epsilon_l + \epsilon_x)} \left(1 - e^{-2.303(\epsilon_l + \epsilon_x)Cl}\right) \tag{23}$$

The scattering intensity at a Raman line x is given by I_x, I_0 is the incident intensity, and J_x is the Raman cross section. The concentrations of the Raman species and absorbing species (if not the same) are given by C_x and C respectively, and the absorption coefficient at the laser excitation frequency and Raman scattering frequency are given by ϵ_l and ϵ_x. There are two relevant cases of this equation to

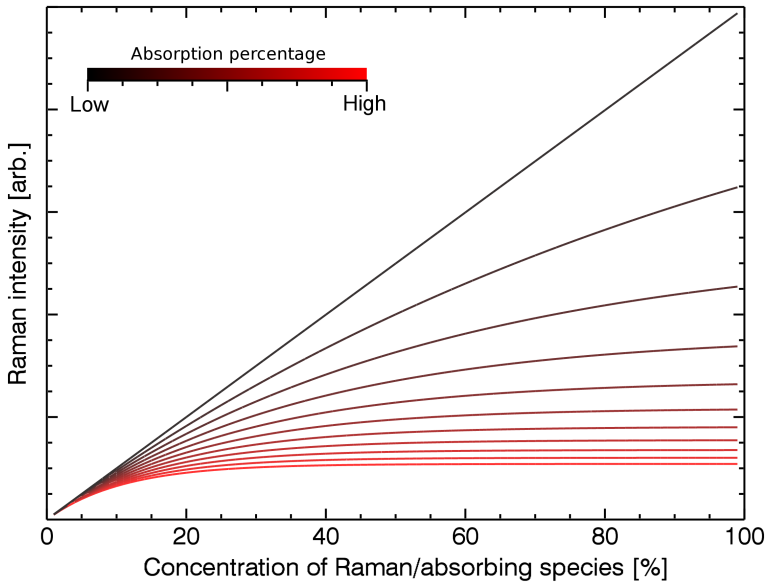

Figure 4: Raman intensity in the presence of an absorbing species at various concentrations, modeled from Equation 23. At high absorbance, the Raman intensity reaches a plateau with increasing concentration.

consider. If the absorption coefficients of the sample are low, the right hand side of the equation will be linear with respect to the sample concentration as $e^x \cong 1 + x$ for small values of x. As expected, at low absorption values the Raman signal increases linearly with sample concentration. However, at high absorption values, the Raman intensity will be a constant (if the Raman species is responsible for the absorption) as $e^{-x} \cong 0$ for large values of x. In this case, the sample will exhibit a Beer-Lambert relationship only until a certain concentration is reached, at which time the intensity will plateau.

A model of Raman intensity versus concentration for various qualitative absorbance values based on Equation 23 is presented in Figure 4, demonstrating the non-linear relationship that can be observed in samples with high absorption. This decrease in signal can in some cases be more than offset by the fourth-power fre-

quency dependence of scattering intensity, or by resonance Raman scattering wherein certain Raman bands will be strongly amplified when the laser excitation is close to an electronic transition in the molecule [62]. By matching the laser frequency to an electronic transition, the vibrational modes associated with that transition can be enhanced. This figure is not used directly in the data analysis in this work, but is presented to note the potential impact of highly absorbent compounds on obtaining a strong Raman signal. The compound thymine (a nucleobase and integral component of DNA) serves as an example of how resonance enhancement can mitigate the effects of ultraviolet absorption. Thymine has an absorption band directly at 266 nm, and resonance enhancement is observed in the primary Raman bands of the compound [36].

Figure 5 presents Raman spectra of thymine in aqueous water solutions at varying concentrations. Due to resonance enhancement, the primary bands of thymine may be observed in concentrations approaching a ppb level, a several order of magnitude improvement compared to traditional Raman sensitivities. As the concentration of thymine is increased, the Raman peaks become more intense (Figure 5 right). However, after the concentration reaches a certain threshold, the observed intensity does not change. The silica peak of the cuvette is marked with a red asterisk, and serves as a peak against which the spectra can be normalized. The concentration of the thymine can be increased up to the point of saturation in water with no further increase in intensity. Resonance enhancement is beneficial to observe low levels of the compound, but at a certain concentration the competing process of absorption can result in the signal intensity reaching a plateau [115].

Ultraviolet Raman wavelengths therefore are potentially more complex than visible wavelengths. As increasing photon energies begin to result in electronic transitions, ultraviolet Raman wavelengths must contend with absorption, fluorescence,

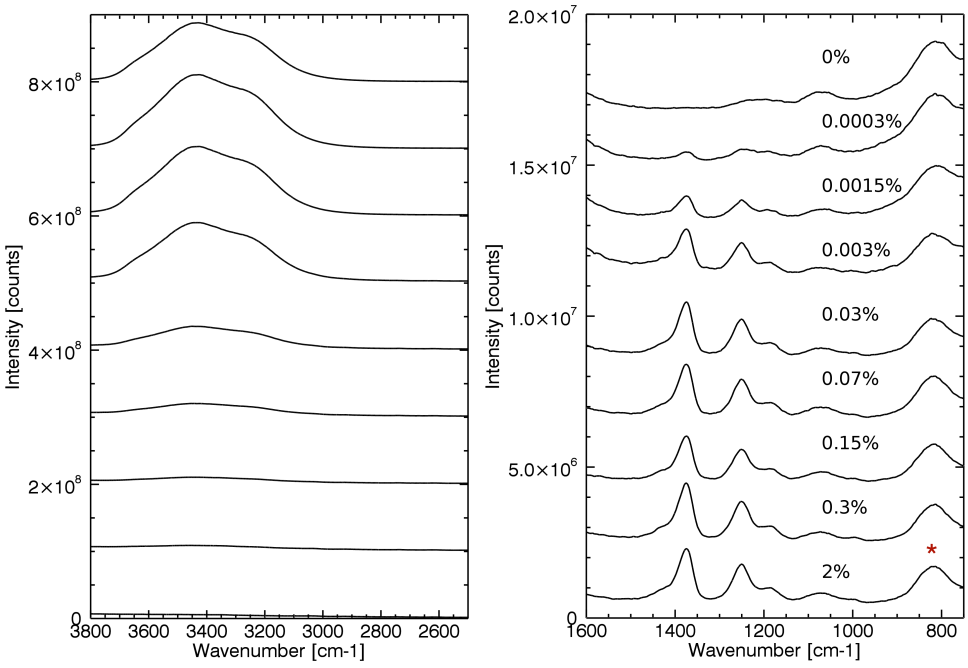

Figure 5: Raman intensity of thymine in an aqueous solution at varying concentrations (right). A red asterisk indicates the Si-O-Si stretch of the cuvette peak against which the thymine peaks can be normalized. The O-H stretching region containing the water signal is presented (left). As thymine strongly absorbs at the laser wavelength, the signal strength reaches a plateau as concentration is increased of the form presented in Figure 4.

and pre-resonance and resonance effects that result in changes in the observed spectra. Some organics that display poor Raman scattering in the ultraviolet compared to longer wavelengths are affected by this tradeoff between resonance enhancement and absorption. Aromatic molecules can exhibit this behavior, as the enhancement of breathing and C=C modes can be offset by absorption due to the presence of ring structures. During the course of this research, several organic compounds, all containing six-membered carbon rings, were found to display very weak Raman scattering at 266 nm, while the same compounds exhibited strong scattering at longer wavelengths including 532 nm. Appendix 8.4 contains the Raman spectra of these compounds obtained at a variety of ultraviolet wavelengths.

1.7 Raman and fluorescence instrumentation for Mars

Instrumentation that is capable of trace organic detection and characterization at or approaching single-ppm sensitivity is required to conduct astrobiological science investigations, and Raman spectroscopic instruments have been identified by NASA as offering the greatest potential for organic detection within a rover platform [2]. The potential benefits of a Raman instrument include stand-off detection at distances on the order of meters away from a rover, rapid and non-destructive measurements, sensitivity to low concentrations of a wide range of organic molecules and biosignatures, and the ability to conclusively fingerprint molecules [e.g. 3, 4, 5, 6].

While a Raman instrument has never flown in space, Mars 2020, the successor to the Curiosity rover, will contain as part of the rover instrument payload both a 248 nm Raman instrument intended for organic detection, as well as a 532 nm Raman system. ExoMars, a rover mission under development by the European Space Agency (ESA) planned to launch in 2018, will also incorporate a 532 nm Raman system. With launch

deadlines set, the field of Raman spectroscopy in a planetary setting is now highly active and many uncertainties concerning instrument performance remain, especially the ability to detect organics in conditions and distributions that may be present on Mars.

The choice of laser wavelength for a Raman instrument is not straightforward, and ultraviolet, visible, and near-IR excitations each offer advantages and the trade-offs must be balanced to meet the specific science objectives of the mission. Each spectral range offers benefits, but no one range is ideal to observe all compounds. Carotenoids show resonance at 488 and 514 nm, and excitation near this region offers the best chance to identify these definitive biomarkers, but most other organic compounds fluoresce strongly in this region. Long wavelengths near 1064 nm offer low fluorescence, but require long exposure times. For identifying the most diverse range of biomarkers as well as mineral content, an excitation of 785 nm is preferred by some authors, but rarely do comparison studies examine excitation wavelengths below 270 nm in the ultraviolet. This is possibly due to the fact that visible and near-IR instrumentation can share many instrumental components, while ultraviolet instrumentation generally requires dedicated optics and detectors with appropriate UV sensitivities. Detectors that are sensitive in the ultraviolet are generally exhibit low quantum efficiencies in the visible to near-IR. Excitation in the UV results in resonance for many organics, good mineralogical analysis, and no fluorescence, but at the cost of a high photon energy that could damage organic material or result in significant absorption in the sample.

1.7.1 Ultraviolet excitation - 355 nm and below

Obtaining high quality data with a Raman system operating in the ultraviolet is more challenging from an instrumental perspective than in other regions of the electromag-

netic spectrum. Optics in the instrument must have the correct optical coatings to ensure good reflectivity in the region close to the short excitation wavelength, and obtaining comparable resolution to visible and near-IR instrumentation is more difficult due to the shorter wavelength range across the Raman window. Despite the engineering challenges associated with UV Raman spectroscopy, there are significant benefits that are especially applicable to imaging of biomolecules and other organic compounds.

The intensity of the Raman scattering increases as the fourth power of the frequency of the incident light, resulting in a significant increase in the number of photons that are Raman shifted at a 266 nm excitation compared to 1064 nm. Therefore, at shorter wavelengths, stronger Raman signals can be obtained for the same laser power. It is also possible for organic compounds to exhibit resonance when excited with ultraviolet radiation, boosting the signal further [80]. Organic nitrites and nitrates, as well as C-H, C-N, C=O, C=C, NH_x, NO_x, SO_x, ClO_4, OH and PO bonds all exhibit this resonance effect to varying degrees [40, 73] when excited with radiation with wavelengths between 220 and 270 nm. The spectra of nucleotides, a class of organic molecule that compose the nucleic acids found in DNA, are best obtained at UV wavelengths where resonance enhancement causes the Raman peak height to increase several order of magnitudes [68]. Polycyclic aromatic hydrocarbons and other aromatic compounds containing six-membered carbon rings also generally experience resonance enhancement of ring-breathing modes when excited in the ultraviolet, and additionally exhibit strong characteristic fluorescence that may be useful in addition to the Raman scattered light.

1.7.2 Visible excitation - 422 nm to 633 nm

While selecting an excitation in the visible to near-IR range can result in strong fluorescence, lasers with an excitation of 532nm are frequently selected for Raman application in the laboratory and for field studies. This is partially due to cost and convenience, but also because in a laboratory environment many of the factors that cause fluorescence are controlled or eliminated through careful sample preparation. Samples of biomolecules and types of minerals that represent the surface composition of Mars were imaged by Marshall et al. [67] at 532 nm, and the authors conclude that, compared to other choices of excitation, 532 nm is preferred for detecting the presence of organic compounds of definite biological origin. At this wavelength, carotenoids, a type of definitive biosignature, experience strong resonance with the laser at certain transitions, and despite fluorescence in this region from other organic compounds, the carotenoids can be clearly detected [66, 84]. Antioxidants such as carotenoids require a biological source, in contrast to some proteins, amino acids, PAHs and non-organic minerals, and are assumed to be fairly prolific in the presence of life. The detection of carotenoids on Mars would be a definitive sign of life.

532 nm lasers are often employed when conducting field work with astrobiological objectives. The Atacama Desert, home to extremophile microbes that survive in the most Mars like conditions on Earth, has been used as an analogue location to test a variety of in-situ Raman techniques using instrumentation incorporating green excitation. The resonance effect with the pigments in the bacteria can overcome strong background fluorescence and result in a very sensitive probe of low levels of organic content. Much of the work presenting 532 nm as a choice for in-situ investigations relies on this resonance effect to mitigate fluorescence. More recently, work done by groups including Blacksberg et al. [14] have incorporated short laser

pulses combined with fast gating of the detector to reduce the fluorescence background and improve the utility of 532 nm as an excitation for a wider range of organic compounds.

1.7.3 Near-IR and beyond - 785 to 1064 nm

Fluorescence from both organic and mineral sources is observed over a wide range from the visible to IR, and is generated by excitations including 466, 532, 633, 785, and 852nm. The effect is strong enough at these excitations to overwhelm the weak Raman signal for some organic compounds. In the near-IR at 1064 nm, the fluorescence is significantly reduced [50, 64], as the photon energy falls below the levels generally needed to drive electronic transitions in molecules. With no interfering fluorescence, 1064 nm would seem to be a promising candidate for obtaining Raman spectra similarly to ultraviolet excitation. 1064 nm has been used to obtain Raman spectra of long-chain alkanes, PAHs, carotenoids, salts of organic acids, and terpenes, demonstrating that the infrared can be useful in characterizing a wide range of organics [50]. The authors concluded that Raman spectroscopy using a 1064 nm excitation is a non-destructive method of identifying potential locations where life, or the byproducts of life, may be present. 1064 nm has also been shown to perform well for mineral targets in addition to organic compounds [107].

Several comparative studies exist in the literature ranking the performance of visible and IR wavelengths. Examining biosignatures of terrestrial extremophiles from Antarctica, Villar et al. [106] compared multiple excitations of 1064, 785, 633, 514, and 488nm. While 1064nm provides fluorescence-free spectra of organic compounds, samples require several hours of data collection in order to overcome the fourth-power intensity dependence on laser frequency. In some cases where comparative studies made recommendations as to the most effective laser wavelength, 785 nm was

suggested as a middle ground to the benefits of both visible and IR wavelengths. However, generally UV wavelengths have been excluded from broad comparative studies. Further, 785 nm is not commonly preferred in the literature when a Raman instrument is applied to a specific study. For example, studies of endoliths typically prefer 532 nm, where resonance with various pigments is expected. The general preference of 532 nm compared to 785 nm may additionally be due to the fact that until recently field-appropriate 785 nm lasers were not available commercially. There is not a single ideal wavelength that encompasses all astrobiological objectives. Instead, a wavelength must be selected to meet specific science requirements, and the limitations of that wavelength must be understood and, where possible, mitigated with engineering or analysis tradeoffs.

1.7.4 Recent applications in Martian astrobiology

With two Raman instruments flying to Mars in 2020, a significant amount of research is ongoing into the performance of Raman systems in Martian environments. Raman instruments, including stand-off prototypes and handheld units, have been able to detect organics in pure form [72, 85] and in trace quantities in mineral matrices representative of Martian environments [109, 86, 102], often employing techniques such as Raman mapping and database matching to locate and classify organic and mineral spectral signatures [103, 101]. While the existence of life on Mars is unknown, a Raman instrument is capable of detecting a wide spectrum of organic material including PAHs and aromatics, geologically preserved organic material, and more complex biosignatures including active microbial colonies. The specifications of instruments that provide the best chance of detecting life continue to be investigated [37, 51].

1.8 Contribution to the field of study

Interference from fluorescence can significantly constrain detection of organic material during Raman analysis of in situ samples. A stand-off Raman spectrometer operating on Mars would likely obtain spectra containing signatures from a complex matrix of organics (if present) and minerals, and the ability to detect organic material would be limited when fluorescence overlaps with Raman bands. We demonstrate in this work that moving to a 266 nm excitation can significantly reduce this fluorescence, while retaining the ability to detect a wide range of organics. In all cases investigated, Raman spectra at 266 nm demonstrate that fluorescence is either removed or reduced to a magnitude approximately equal to the intensity of the Raman scattering.

As fluorescence quantum yields can be several magnitudes greater than Raman scattering, a combined Raman and fluorescence instrument may be more sensitive to organic carbon than a Raman instrument alone if organic fluorescence can be discriminated from mineral fluorescence. In this work a method was developed for measuring fluorescence lifetimes of unprepared samples. While not achieving the time resolution of time correlated single photon counting (TCSPC) or other traditional lifetime measurement techniques, this method may be performed in-situ on a planetary surface without greatly adding to the complexity of a Raman instrument. This ability allows discriminating mineral from organic fluorescence, as short lifetimes ($<$ 10 ns) are considered a strong indication of organic material. The diversity of fluorescence lifetimes observed in PAHs and mineral samples strongly motivates future work in this area, as fluorescence lifetimes may provide more information about a sample beyond identifying the presence of organics.

With an ultraviolet Raman system arriving on Mars in 2020, the work done in support of this degree is relevant to the current field by demonstrating that a 266 nm

excitation is sufficient to observe Raman bands without fluorescence. This work is additionally relevant by presenting the ultraviolet Raman spectra of a range of organic and mineral samples, developing analytical techniques to extract as much quantitative information from 2D Raman maps as possible, and for proposing capabilities, such as sub-ns time-resolved fluorescence imaging, that would be beneficial for successive generations of flight instruments intended for Mars or other planetary surfaces.

2 Measurement and analysis methods

This chapter describes in detail the design of the instrumentation used to complete this work. The bulk of the research was conducted with a 266 nm Raman spectrometer developed at York University, designed to meet the specifications of a putative flight instrument. The breadboard configuration of the instrument permitted modifications to meet the needs of a particular experiment. Some work was completed using a separate 355 nm instrument, with a similar design in terms of the detector, spectrometer, and operational concept. This chapter also provides a detailed overview of the analytical techniques used to analyze single spectra and large spectral datasets.

Methodologies for reporting the instrument capabilities are traceable to conventions defined by the International Union of Pure and Applied Chemistry (IUPAC) when possible. For example, instrument resolution is presented using the IUPAC defined 50% speak width spectral resolution, and the instrument limit of detection is defined using the IUPAC limit of detection in analysis [70]. As the field of Raman spectroscopy applied to astrobiology is relatively new, conventions are sometimes acquired from IUPAC or the field of fluorescence spectroscopy which is more established. The samples that were selected for study fall into categories identified as having high astrobiological relevance by groups including the Mars Exploration Program Analysis Group (MEPAG) [54].

2.1 266 nm instrumentation

York University's 266 nm Raman system is operated under Professor Michael Daly's Planetary Instrumentation Laboratory (PIL) in the Department of Earth and Space Sciences. The instrument is a custom-built non-commercial system constructed on an optical table in a breadboard configuration.

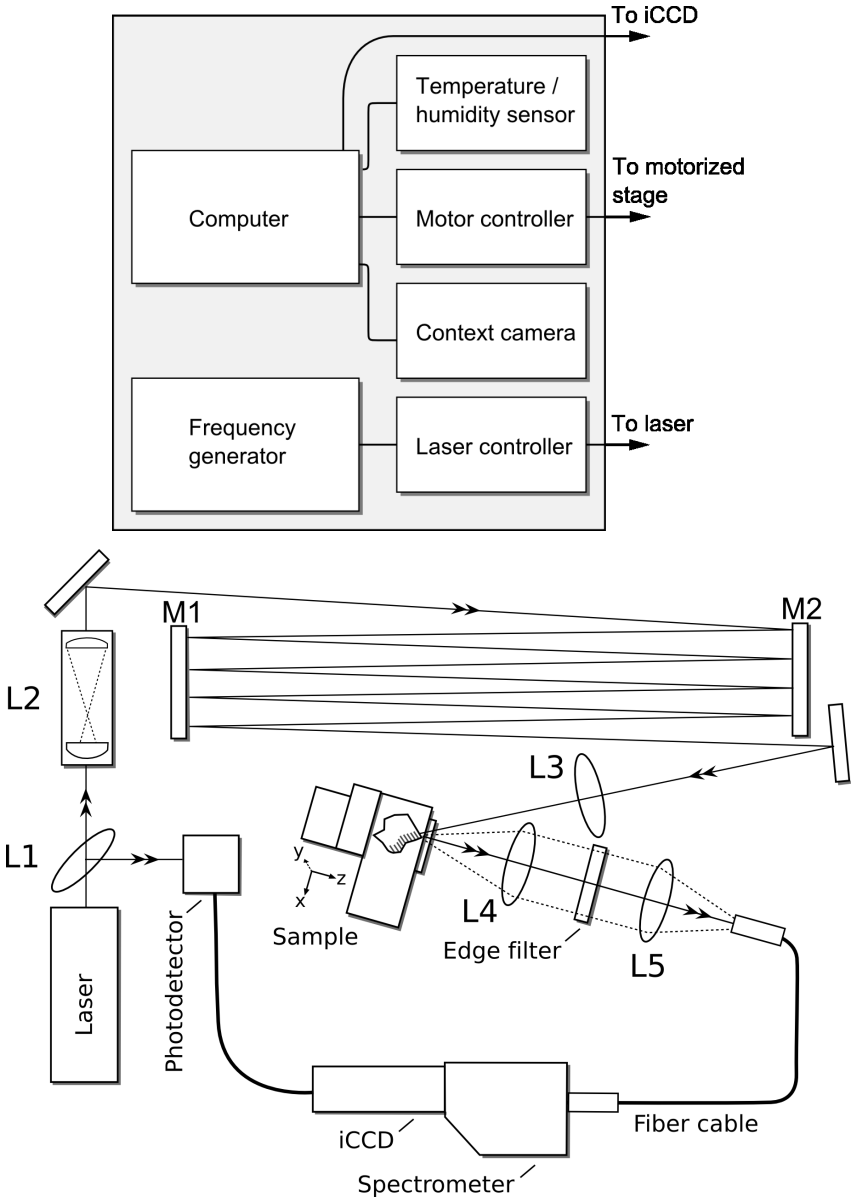

Figure 6: 266 nm Raman spectrometer instrument diagram. Top: control electronics block diagram showing the frequency generator used to trigger the laser, and the instrumentation controlled by a computer. Bottom: A small percentage of light exiting the laser is used to trigger a photodetector (L1). The beam is expanded (L2) and directed (M1, M2, L3) to a sample stage. Scattered light is collected (L4, L5) and sent to the detector.

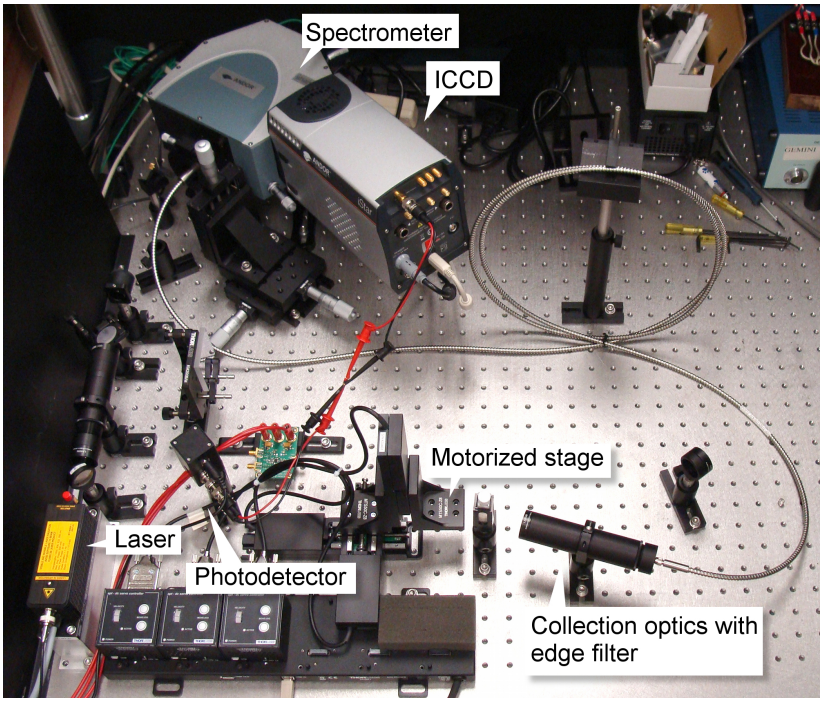

Figure 7: 266 nm Raman spectrometer breadboard

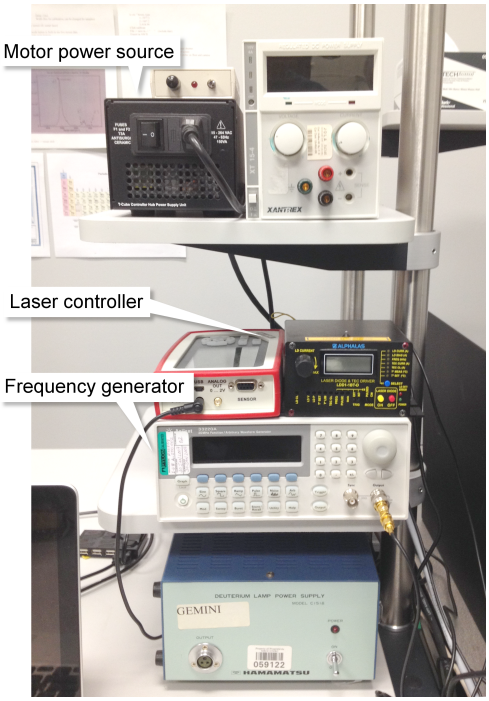

Figure 8: 266 nm Raman spectrometer control electronics picture

The 266 nm Raman spectrometer was designed with the rough requirements of a putative flight instrument, primarily considering the laser power, spot size, and angular resolution when operating in a mapping mode. This design, while not achieving the micrometer-scale spatial resolution of a typical Raman microscope, allows investigation into the type of response that could be expected from a stand-off, rover mounted instrument with similar specifications. The instrument schematic is shown in Figure 6. Excitation is provided by an ALPHALAS diode-pumped solid state Nd:YAG laser with a 0.6 ns pulse width and 1.4 μJ of energy per pulse. The 1.064 μm fundamental wavelength is frequency quadrupled using two separate frequency-doubling crystals to obtain the desired 266 nm radiation. The laser is pulsed at 5 kHz, resulting in an average power of 2 mW of 266 nm radiation incident on the sample. Power losses are primarily due to the imperfect reflectivity of the laser-line mirrors (M1, M2) that add approximately 8 m to the laser path, necessary to compensate for the 35 ns delay between the trigger pulse arriving at the iCCD and the intensifier tube switching open. The beam profile is slightly elliptical at the sample, with a 16/84 knife-edge width of 0.6 mm by 0.9 mm, adjustable down to tens of microns.

Exiting the laser, the light is split by a quartz beam sampler (L1), with 1% of the signal directed onto a photodetector which is used to trigger the iCCD gate (see Figure 7). The remainder of the light is beam expanded (L2) for safety and to decrease the beam divergence. The light is focused (L3) onto the sample, which is positioned on a 3-axis motorized stage. The scattered light is collected in a 160^{o} backscatter geometry, collimated (L4) through an edge filter to remove the intense Rayleigh band, and focused (L5) onto an optical fiber. The edge filter uses a thin-film Ion-Beam-Sputtered (IBS) deposition to block radiation below the cutoff value. Approximately 0.14 sr. of the scattered radiation is captured using this optical configuration. The 127 optical fibers in the fiber cable are aligned into a slit with an active area of 0.07

x 8.38 mm and coupled directly to the entrance of the spectrometer, maximizing the throughput of the system.

Light exiting the fiber cable is focused into a grating spectrometer (Andor Shamrock 163) with a 163 mm focal length and a focal ratio of f/3.6. A 2400 l/mm grating with a 300 nm blaze allows for an observation window between 286 cm^{-1} and 3805 cm^{-1}, with a central resolution better than 30 cm^{-1}. A finely ruled rating is required to compensate for the short UV wavelength and achieve an acceptable resolution. This observation window contains the primary Raman bands of organics, most minerals, and higher-wavenumber modes, which include C-H and O-H stretching frequencies above 3000 cm^{-1}. The Raman signal is detected by an intensified CCD (Andor iStar 334T) coupled to the spectrometer and cooled to -38^{o}C using a thermoelectric cooler that is itself water cooled with a coolant temperature of 15^{o}C. The light path through the spectrometer and detector is shown in Figure 9. Light entering the detector is directed onto an Ø18 mm photocathode, generating photoelectrons which are amplified in an intensifier tube containing a microchannel plate. A phosphor converts the intensified electron cloud into visible photons detectable by a 1024 x 1024 pixel CCD with 13 μm pixels. The iCCD provides nanosecond scale gating by controlling the voltage across the intensifier, allowing for reduction of both ambient light and reduction of fluorescence, which typically has a longer lifetime than Raman scattering. This gating is possible because a strong voltage gradient is required to direct photoelectrons from the photocathode to the microchannel plate (MCP). When the gate is closed, the voltage gradient is reversed, and no photoelectrons will enter the MCP. This gating process is described in more detail in Appendix 8.1.

A 5-10 ns gate width was determined to maximize the Raman signal-to-noise ratio. All Raman spectra in the subsequent sections are presented without fluorescence subtraction to emphasize the reduction of fluorescence at UV wavelengths, unless

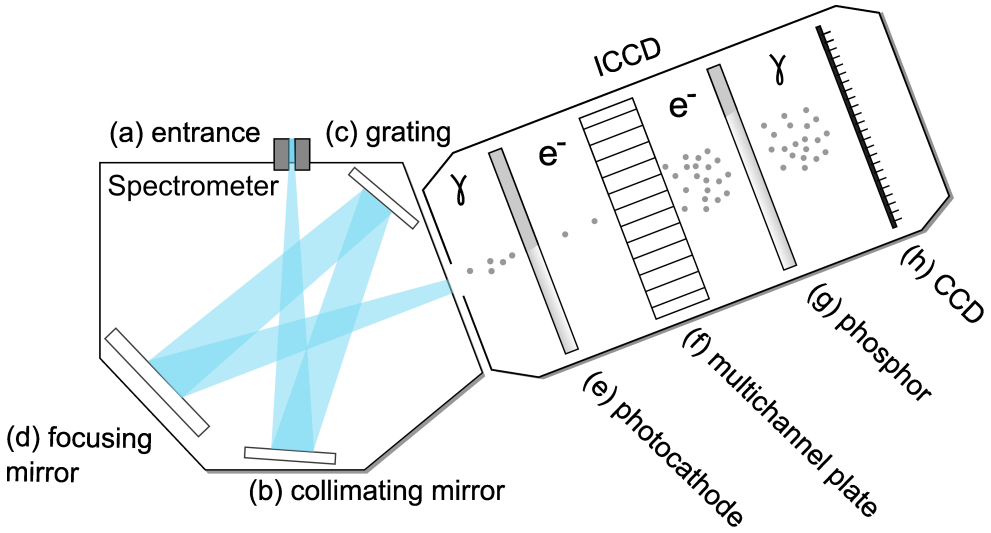

Figure 9: Light path through the spectrometer and ICCD. Light entering the spectrometer (a) is collimated (b) and separated by wavelength by a diffraction grating (c). A focusing mirror (d) directs light to the entrance of the ICCD. Incoming photons are converted into photoelectrons (e), amplified through a microchannel plate (f), and converted back to visible wavelength photons (g) before striking the CCD (h).

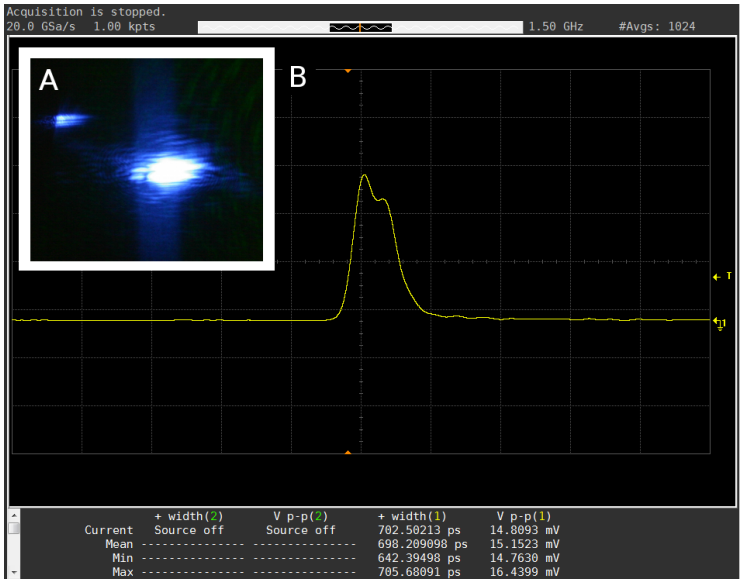

Figure 10: (A) Laser beam profile and (B) temporal pulse shape.

indicated. Spectra were typically processed by performing a background correction to remove the low levels of ambient UV light and detector noise. Background correction was performed by obtaining a spectrum with the laser running but blocked from hitting the sample, with an accumulation time equal to that of the desired measurement. Subtracting the background spectrum from the final acquisition therefore removed any contribution from ambient noise or dark current.

On Earth, virtually no background radiation exists between 266 and 300 nm, as the ozone layer absorbs most ultraviolet radiation from the sun. On Mars, higher levels of background will exist, and therefore a Raman instrument may potentially encounter higher background noise than on Earth. An order of magnitude estimation of this effect can be calculated. First, the throughput of the instrument was determined by measuring the spectral peak due to the laser. The number of photons in each pulse was calculated by measuring the average power at the sample, then multiplying by the repetition rate of the laser in Hz and accounting for the energy per photon at 266 nm. In order to determine the number of photons scattered within the solid angle observed by the system, a 99% reflectance Spectralon standard was used to generate diffuse scattering. The number of photons scattered within the solid angle observed by the detector was compared against the number of photons that ultimately reached the CCD per pulse, measured by converting counts to photons using sensitivity curves provided by the detector manufacturer. The relation between counts and photons is described in Appendix 8.1.

With an approximate value for the instrument throughput, the number of background photons on Mars that would reach the detector was calculated using the known ultraviolet flux on the Martian surface. The ultraviolet flux at the surface of Mars between 266 and 296 nm was determined using a value of 586 W/m^2 for the solar irradiance at Mars[20]. The number of photons that would reach the CCD

was determined by integrating over the region 266 nm to 300 nm and converting to number of photons. Assuming the field of view of the instrument is on the order of an upper bound for the laser spot, $4\,mm^2$, there may be approximately 1 to 5 background photons incident on each pixel column in the CCD per pulse on Mars, assuming a fast gate is used. For comparison, a moderately strong Raman band may result in greater than several tens to hundreds of Raman scattered photons per pulse incident on each column of pixels.

2.1.1 Calibration

Calibration of the wavenumber axis (x-axis) was performed using powdered L-alanine as a standard. To perform the calibration, an alanine spectrum was recorded and the pixel locations of four peaks were used to generate a quadratic fit to the known peak positions in wavenumbers. As the Raman window with a 266 nm excitation extends to approximately 296 nm, more common calibration sources including Hg-Ar lamps do not provide sufficient peaks that span the observation window. Several common Raman standards, such as polystyrene and naphthalene, absorb in the ultraviolet and exhibit weak Raman scattering at 266 nm and could not be used for calibration. L-alanine peak positions were previously measured, using the same L-alanine sample, with a 355 nm Raman instrument that had been calibrated with a Hg-Ar lamp. For the fluorescence measurements presented in Chapters 4 and 5, the larger window of observation permitted calibration using a Hg-Ar lamp.

A NIST calibrated deuterium lamp provided a flat broadband UV source in the region between 266 nm and 296 nm for a spectral intensity calibration (y-axis calibration). The intensity calibration primarily accounted for the effect of the edge filter, which has less than 50% transmittance below 400 cm^{-1}, but also accounted for other factors including variations in the sensitivity of the CCD, and any instrumental

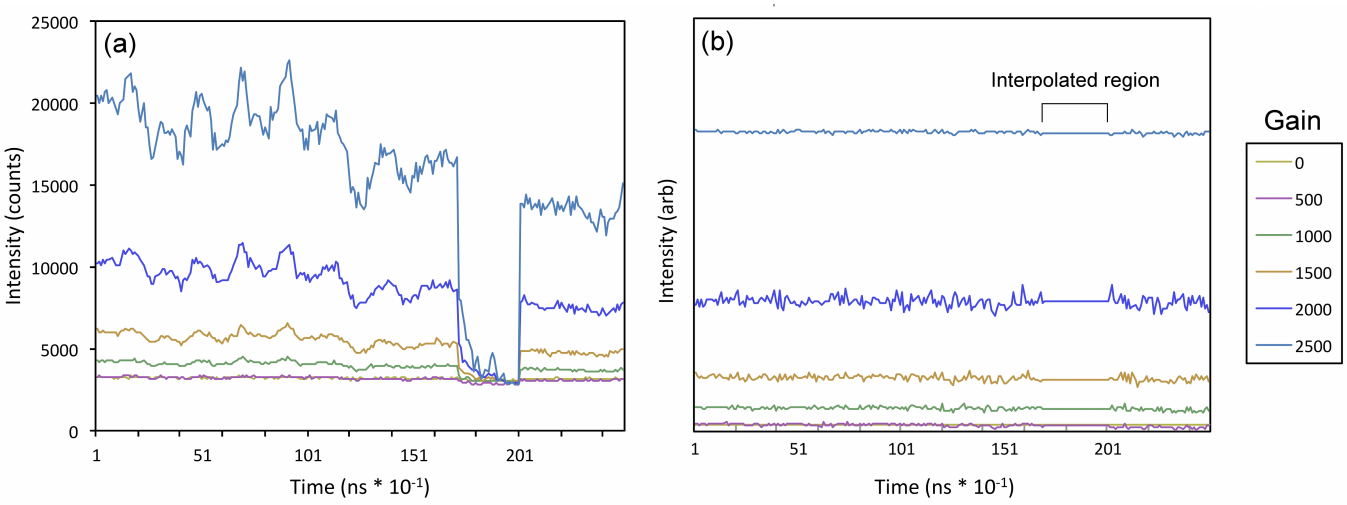

Figure 11: Instrument response function (IRF) used to calibrate the time axis of time-resolved fluorescence measurements. (a) The measured intensity of a blue LED with constant output depends on the gate delay if the shortest gate width (1.5 ns) is used. A region of particularly low sensitivity occurs between gate delay values of about 17 to 20 ns. (b) A calibration factor (IRF) is applied to the measured data, showing the corrected intensity. The IRF is independent of gain, and depends only on the gate delay.

components with efficiencies dependent on the frequency of the incident radiation. Spectral intensity was not corrected for fluorescence measurements. This correction could be roughly performed using the known relative peak heights of several of the emission lines from the Hg-Ar lamp, but the resulting correction would need to make the assumption that the correction factor was smooth between the calibration datapoints. A sensitivity curve provided by the manufacturer could assist in verifying that assumption, and in fact the sensitivity curve matched well when compared with the measured peak ratios of the Hg-Ar lamp.

Time-resolved measurements, described in detail in Chapter 4, required calibration of the time axis. When using the shortest possible gate width (1.5 ns), the degree to which the gate opens depends on the gate delay. At some delay settings, the gate does not fully reach an open state before closing. Consultation with the manufacturer

Parameter	Typical value
Power / repetition rate	2.1 mW @ 5 kHz
Spot size	0.1 - 2 mm
Temperature	-25 C; -38 C with chiller
Timing	5 sec. to 10 min. accumulations, 0.05 s exposure time
Triggering	Gate width: 6 ns; Gate delay: variable
Intensifier gain	3000

Table 3: Typical laser and detector acquisition parameters

revealed that this is a known property of the detector model used in this work. In order to determine a correction factor that could be applied to time-domain measurements, the peak emission wavelength of a blue LED with a constant output was measured using a 1.5 ns gate over a period of 20 ns, with a 0.1 ns gate step between subsequent measurements. These parameters matched the experimental parameters used to acquire the time-resolved fluorescence spectra presented in this work, and the resulting correction factor is shown in Figure 11. The LED was driven by an external current source for stability, and multiple time-resolved measurements were averaged to further account for intensity variations over the course of the measurement. Multiple measurements were also obtained at several gain settings, to ensure that the instrument response was not dependent on gain. The output of the LED was verified to be stable over the measurement lifetime using a Thorlabs power meter. The most significant feature present in the resulting correction factor was a 3 ns region between gate delay settings of approximately 17 and 20 ns that resulted in very low signal levels. In Chapter 5, fluorescence spectra are presented with interpolated data within this region.

2.2 Raman measurements

Pure organic compounds and mineral/organic mixtures, as well as mineral powders, were tested in fused-silica cuvettes with a 1 cm path length. Raman scattering off the cuvette was found to be very weak, as the cuvettes have a transmission in the UV of about 90%. A spectrum of the cuvettes used for the investigations described in this report is shown in Figure 13. The primary Raman band, broadened on the low-energy side of the band due to the amorphous structure, is located below 475 cm^{-1} and does not overlap with the primary peaks of organics and most minerals. The experimental parameters used in the investigations are similar whether the target is mineral, organic, solid, liquid, or in a cuvette. Several of these parameters, primarily the detector settings, significantly affect the quality of the Raman data. Typical instrument parameters are listed in Table 3. A more comprehensive table of instrument parameters is presented in Appendix 8.1. When obtaining spectra of mineral or organic targets, the acquisition time can vary on the order of minutes. Raman-scattered photons arrive at the detector in ns-scale pulses and accumulate charge on the CCD, shown in Figure 14. This charge is read out to the computer every 0.05 seconds. For the measurements of pure organic compounds presented in Chapter 3, a 10 minute measurement time was sufficient to observe all expected Raman peaks based on a survey of previous Raman studies of the compounds.

Synchronizing the camera's electronic gate with the Raman pulse allows for a significant reduction in noise and fluorescence, shown in Figure 14. When obtaining Raman data, ideally the gate delay should be set to open the intensifier at the time the Raman-scattered photons arrive at the detector, and the gate width should be set to only the duration of the incoming pulse. A gate width of 6 ns is sufficient to capture the Raman scattering while rejecting other sources of radiation. When measuring

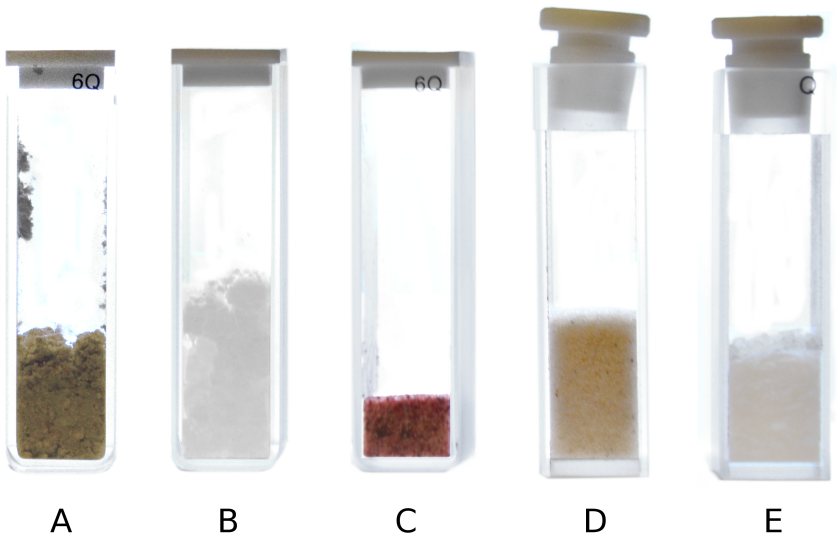

Figure 12: Fused-silica quartz cuvettes used as sample containers. Mixtures of mineral and organic (A, C, D) as well as pure organic powders and crystals (B, E) can be tested. Raman peaks due to the cuvette are weak and restricted to low wavenumber regions.

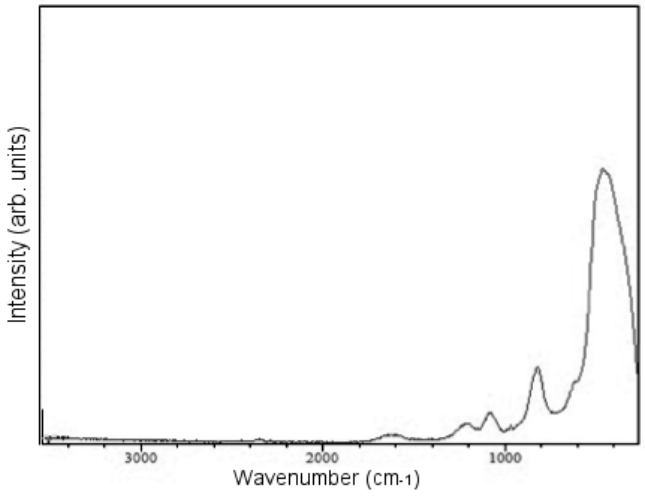

Figure 13: Raman spectrum of fused silica cuvettes used as sample containers. The broad band located below 475 cm^{-1} is due to the amorphous silica structure, with other bands representing various Si-O-Si bending and stretching modes.

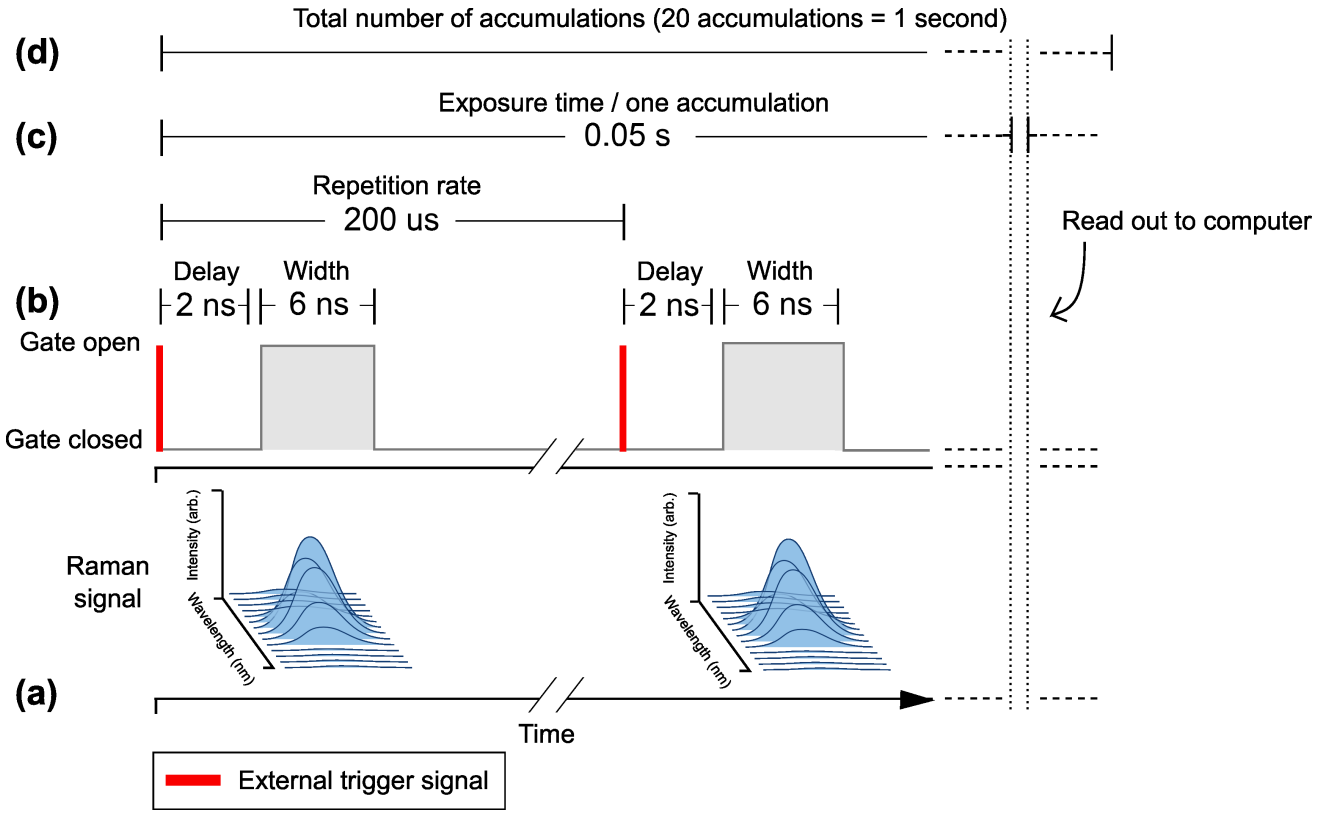

Figure 14: ICCD timing diagram. The laser, operating at 5 kHz, results in a pulse of light entering the detector every 200 microseconds (a). The detector receives an external trigger signal (b), indicating the laser has emitted a pulse, then waits a certain period of time (the gate delay) before opening to allow the incoming pulse to enter (gate width). As more pulses enter the detector, charge accumulates on the CCD. Every 0.05 s, charge is read out to the computer (c) and the CCD is prepared for a new accumulation. This process repeats (d), for example with a measurement time of 10 minutes representing 12,000 individual accumulations/exposure periods.

fluorescence as opposed to Raman scattering, the gate width was reduced to the minimum value, 1.5 ns, and multiple accumulations were obtained with increasing gate delay values. The resulting dataset contained a time-resolved measurement of the fluorescence, showing the full spectral behavior evolving in time with a nanosecond-scale resolution, described in detail in Chapter 5. A critical component of the detector is the ability to amplify the incoming signal. Raman scattering is a very weak process with cross sections on the order of 10^6 or 10^7 times less intense than Rayleigh scattering or fluorescence emission. Incoming photons, converted into photoelectrons, are cascaded through the intensifier in the detector, significantly amplifying the Raman signal, shown in Figure 9. The only pre-processing performed on the data was a background correction, removing the effects of dark current and accounting for any hot pixels or other CCD inhomogeneity. The background spectrum was always saved alongside the corrected spectra.

2.3 Analysis of spectra

Throughout this work many spectra are presented and Raman bands are identified and discussed and therefore it is useful to review the analysis methods selected to interpret individual Raman bands as well as analyze large datasets. Chemometric analysis was applied to larger datasets, and the following sections also describe the primary multivariate algorithms used to analyze datasets with hundreds or thousands of spectra. Chemometric methods are used in Chapter 4 to obtain fluorescence decay lifetimes, and in Chapters 3 and 5 to identify regions of interest in Raman and fluorescence maps. There are many alternative methods of analysis that could be substituted for these techniques, including cluster analysis and various machine learning algorithms. The intent in applying the multivariate algorithms presented in this work

was to identify situations where such techniques may be useful on a rover platform, for example in cases where the instrument may need to make informed decisions with humans out of the loop. The intent was not to define what specific algorithms are best suited for a particular task.

2.3.1 Peak identification in single spectra

Chapter 1 reviewed the theory and methodology used to interpret and model Raman spectra, attributing molecular vibrations to observed spectral bands. In this work, this computationally difficult approach was not applied directly, as many of the compounds selected for study have been well characterized by other authors. Generally Raman bands were identified in this work by matching experimentally obtained spectra to results available in the literature. In many cases, these authors applied the same methods discussed in Chapter 1 to obtain their results, such as DFT modeling to calculate vibrational frequencies. Due to the complexity of theoretical modeling, some authors disagree on the attributions for some of the weaker bands seen in complex spectra. There are occasionally contradictory results presented in Raman literature, especially in the field of planetary science where the research focus is weighted towards detection of organics and not towards the rigorous analysis of obtained spectra. In this work, peak attributions were referenced by more than one independent source if possible, and the strong bands significant for the analysis have undisputed molecular origins.

2.3.2 Principal components analysis (PCA)

PCA is a multivariate technique that is frequently used to reduce the dimensionality of large datasets, and can highlight important differences and groupings in spectral data. Given a dataset composed of hundreds or thousands of spectra, PCA can determine

the number of physical constituents of the system, their distributions in the dataset, and identify outliers or isolated spectral features. In this work, PCA was applied to Raman and fluorescence maps, datasets containing several hundred to several thousand individual spectra. PCA is able to determine how each variable (each measured wavenumber on the x-axis) chances in relation to the other variables. The resulting principal components (PCs) are vectors that contain information on correlated variables. For example, a PCA analysis of Raman map of a rock surface composed of an inhomogenous mix of gypsum and quartz would yield two primary PC vectors, one similar spectrally to gypsum, and the other similar spectrally to quartz. Subsequently, each spectrum in the Raman map, composed of 1024 datapoints, could be re-expressed in terms of only two datapoints describing the magnitude of contribution from each PC. In an uncharacterized sample, examining the principal components can help identify and separate spatially the components of the system.

An example of PCA is shown in Figure 15, simulating a Raman map across an inhomogenous sample with two physical components. Examining one row of the Raman map, Figure 15 (a) show the spectra as obtained by the Raman instrument. Figure 15 (b) presents the principal components, vectors that describe the primary components of the system. In Figure 15 (c), each point on the map is re-expressed in terms of the PCs. Figure 15 (d) and (e) show Raman maps derived from the PCs and the dataset expressed in PC space, respectively.

Data intended for PCA must be means-centered to have a zero mean value following

$$\boldsymbol{x} = x_i - \bar{\boldsymbol{x}} \quad \boldsymbol{y} = y_i - \bar{\boldsymbol{y}} \tag{24}$$

where $\bar{\boldsymbol{x}}$ and $\bar{\boldsymbol{y}}$ indicate the sample averages. A covariance matrix must be cal-

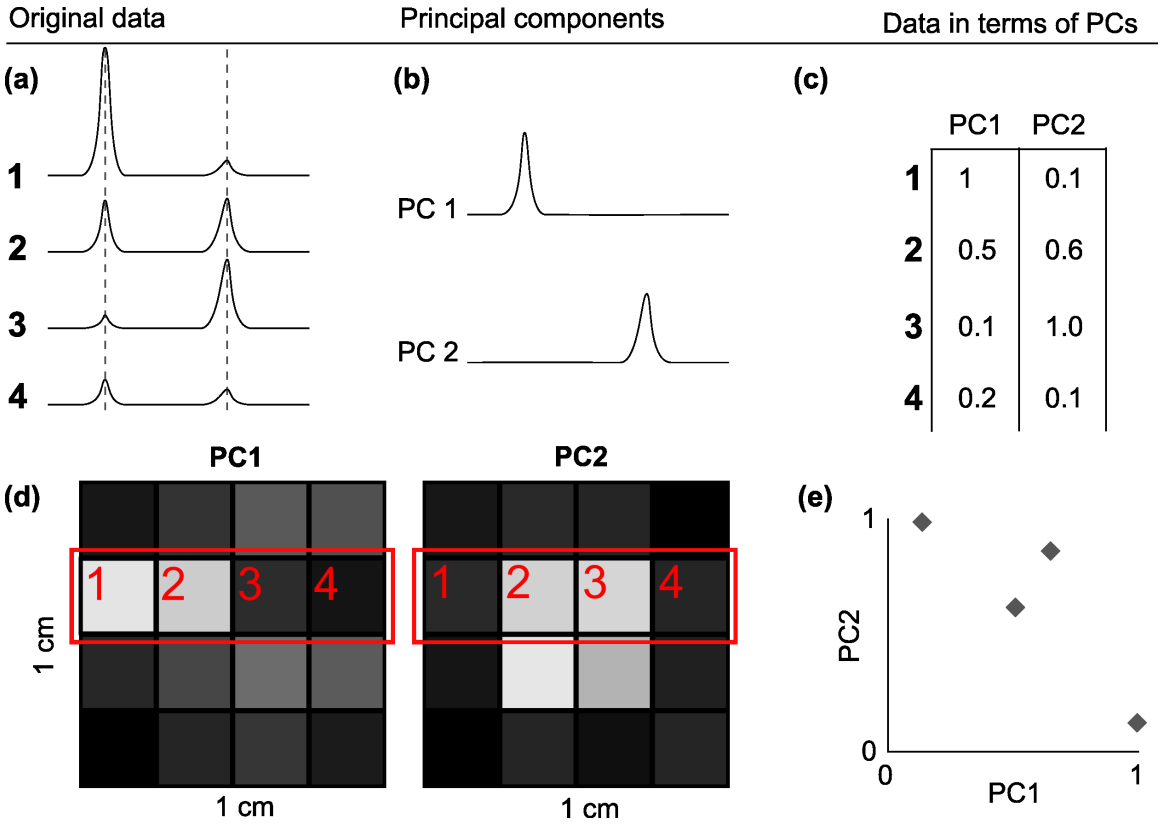

Figure 15: Example of Principal Components Analysis (PCA) using a simulated Raman map of across one square cm of an inhomogenous sample composed of two primary compounds. Examining one row of the Raman map, in (a) the spectra as measured by the Raman instrument are shown. PCA analysis identifies two principal components (b), and the original data can be expressed in terms of these PCs (c). (d) shows a simulation of Raman maps generated using the PC values. The dataset may also be expressed in PC space (e).

culated for the dataset using Equation 25. Covariance is calculated between two dimensions in the data, and therefore the covariance matrix for an n dimensional dataset will contain $n!/\left(2 \times (n-2)!\right)$ covariance relations. The covariance between two dimensions describes the extent to which the data in the two dimensions change together as the values deviate from the means of the dimensions.

$$\boldsymbol{C}(\boldsymbol{X}, \boldsymbol{Y}) = \frac{\sum_{i=i}^{n}(X_i - \bar{\boldsymbol{X}})(Y_i - \bar{\boldsymbol{Y}})}{(n-1)} \tag{25}$$

The eigenvectors of the covariance matrix will describe the relation between the dimensions of the data. There will be as many eigenvectors as dimensions in the original data, however many will not contain useful information. The relative importance of the eigenvectors can be determined by ordering them by their associated eigenvalues, and a feature vector can be constructed by selecting an arbitrary number of eigenvectors $\boldsymbol{e}_n$, representing as much information from the original dataset as desired.

$$\boldsymbol{F} = \begin{pmatrix} \boldsymbol{e}_1 & \boldsymbol{e}_2 & \dots & \boldsymbol{e}_{\text{arb.}} \end{pmatrix} \tag{26}$$

Finally, the original data $\boldsymbol{X}$ can be expressed in terms of these principal components by multiplying by the transpose of the feature vector.

$$\boldsymbol{T} = \boldsymbol{F}^{\top}\boldsymbol{X} \tag{27}$$

The result is the original dataset expressed only in terms of combinations of the principal components. The resulting matrix $\boldsymbol{T}$ can be plotted in two or three dimensions, and in the case of spectral data every spectrum in the dataset will be reduced to one point in principal component space, with nearby points representing spectra

with similar features.

2.3.3 Partial least-squares regression (PLS)

The multivariate technique partial least-squares regression (PLS) is similar to PCA and is useful when a linear regression is desired but the number of variables is large, which is the case with spectral data, where the goal is to determine the concentration of a particular compound, or determine a limit of detection for a particular compound. The PLS algorithm reduces the dimensionality of the dataset by calculating latent variables, which are similar conceptually to principal components, and are vectors that may be linearly combined to describe the data. Spectra of samples where the mixture of the constituents is unknown can be regressed against an appropriate PLS model to determine the concentrations of the components.

The goal of the PLS algorithm is to determine the relationship between a matrix $\mathbf{X}$ containing the spectral information and a matrix $\mathbf{y}$ containing the responses - such as concentration, decay lifetime, or other experimental quantity. $\mathbf{X}$ is an $n \times k$ matrix, where k contains the spectral data, and n represents the number of responses in the model, for example the number of concentrations of a mixture that were tested. $\mathbf{y}$ is a $1 \times n$ matrix which contains the response information. Score vectors are then computed that contain information on how $\mathbf{X}$ and $\mathbf{y}$ are connected, and a number of latent variables are selected to represent the information in the model. The end product is $\boldsymbol{b}$, the regression vector. Once the regression vector has been determined, the lifetime $\hat{c}$ of an unknown spectrum $\boldsymbol{r}$ can be predicted using Equation 28.

$$\hat{c} = \boldsymbol{r} \cdot \boldsymbol{b} \pm y_{\text{dev}} \tag{28}$$

The error of the lifetime determination y_{dev} is calculated as a deviation in the

predicted value from the model following the method described by [110]. It is also possible to calculate fit error using a global model error RMSEP (root mean squared error of prediction), using a χ^2 goodness of fit, or using other methods [22]. The PLS algorithm has a number of applications in this work; determining a limit of detection of the instrument, determining the relative concentrations of minerals in rock samples, and calculating fluorescence lifetimes by matching decay curves to models. The extensive application of the PLS1 version of the PLS algorithm throughout this work justifies presenting and discussing the algorithm in detail, and Mathematica code for applying the algorithm is provided in Appendix 8.2.

3 Ultraviolet Raman analysis of organic compounds and minerals

This chapter contains work adapted from the following peer-reviewed published article

> Eshelman, E., Daly, M. G., Slater, G., Dietrich, P. & Gravel, J.-F., An ultraviolet Raman wavelength for the in-situ analysis of organic compounds relevant to astrobiology. Planetary and Space Science 93, 65-70 (2014).

and presents the fluorescence and Raman spectra of a range of organic compounds including amino acids, fatty acids, alkanes, and polycyclic aromatic hydrocarbons (PAHs) at three UV excitations to determine at what Raman excitation fluorescence is minimized. Both Raman and fluorescence measurements indicate that a Raman instrument operating with an excitation of 266 nm will result in less fluorescence compared to an excitation of 355 nm. Raman spectra of organic compounds are also presented at a 1% concentration in a silica sand matrix, obtained at an excitation wavelength of 266 nm.

3.1 Introduction

Several Raman instruments have been proposed [73, 25] as part of a rover payload to detect the presence of organic carbon-containing compounds on Mars and to characterize mineralogy [15]. Although no Raman instrument has yet flown, advances in diode-pumped lasers and detector sensitivities now allow for a Raman instrument that meets the mass, power, and efficiency requirements of a space mission.

Essential to the development of a stand-off Raman instrument for a Mars rover is the selection of a laser excitation wavelength. Nd:YAG lasers have a substantial flight heritage and good efficiency, which motivates their incorporation into any proposed

Raman flight instrument [1]. A Nd:YAG laser was first used on Apollo 15, and the first space application of a diode pumped laser was in the Mars Orbiter Laser Altimeter (MOLA) instrument [89, 1]. More recently, a Nd:YAG laser was the basis of the Mars Phoenix LiDAR instrument [112] and is planned for the upcoming OSIRIS-REx Laser Altimeter [16]. Nd:YAG lasers can provide a range of IR to UV excitations from the fundamental 1.064 μm frequency through harmonic generation.

In this chapter we characterize the fluorescence spectra of a range of organic compounds when excited with 250, 266, and 355 nm wavelengths in the ultraviolet in order to select a wavelength for a future Raman spectrometer. At a 250 nm excitation, the Raman active region up to 4000 cm^{-1} extends less than 30 nm from the excitation wavelength, outside of the fluorescence region of both minerals and organic compounds [41, 7]. At an excitation of 355 nm we show that, for several of the organic compounds tested, fluorescence is significantly present in the Raman region. A compromise between these two excitations is achievable with the 266 nm fourth harmonically generated wavelength of an Nd:YAG laser. An excitation of 266 nm is found to provide excellent fluorescence mitigation and sensitivity while protecting the efficiency and heritage of Nd:YAG lasers. Raman measurements of a range of organic compounds at the chosen wavelength are presented to validate this choice.

3.2 Sample preparation

Pure organic compounds L-alanine (A7627), DL-cystine (C8630), octacosane (O504), L-lysine (L5501), L-serine (S4500), and stearic acid (S4751) were obtained from Sigma-Aldrich. Low concentrations of 1% organic by weight were made using silica sand with a 0.31 mm median grain size as a substrate. The silica sand substrate

was initially heated to 600^{o}C to remove any organic contamination. Following heating, a measured quantity of each organic compound was dissolved in an effective solvent, typically dichloromethane (DCM). The organic and solvent were added to the silica sand to achieve a ratio of 1% organic by mass. The solvent was evaporated with a rotary evaporator, resulting in an even distribution of the organic across the substrate. The amount of organic lost during the mixing process was determined to be under 5% by analyzing the residual material that remained on the sides of the glassware. Although silica is not a good Mars analogue, as relatively low amounts of silica have been detected on Mars, silica was chosen due to the ease of mixing with a solvent (compared to compounds such as gypsum or halite) and for its low absorbance in the ultraviolet.

Organic compounds can have altered spectral properties when in solution, including broadening and shifting of the Raman peak positions [117]. To determine if the sample preparation procedure altered the spectral properties of the organic compounds, spectra of pure organic compounds were compared with the resulting 1% mixtures. The average magnitude of the shift in peak position was calculated for several characteristic peaks and found to be insignificant, below 4 cm^{-1}, indicating that any changes in the properties of the organic compounds during mixing did not persist when the compound was evaporated out of the solvent onto the substrate.

Fluorescence spectra were obtained using aqueous samples of alanine, cystine, lysine, and serine. A measured amount of the organic compound was dissolved in distilled water to achieve a concentration of 3%. The fluorescence spectrum of fluoranthene was obtained with a silica sand substrate prepared using the method described above.

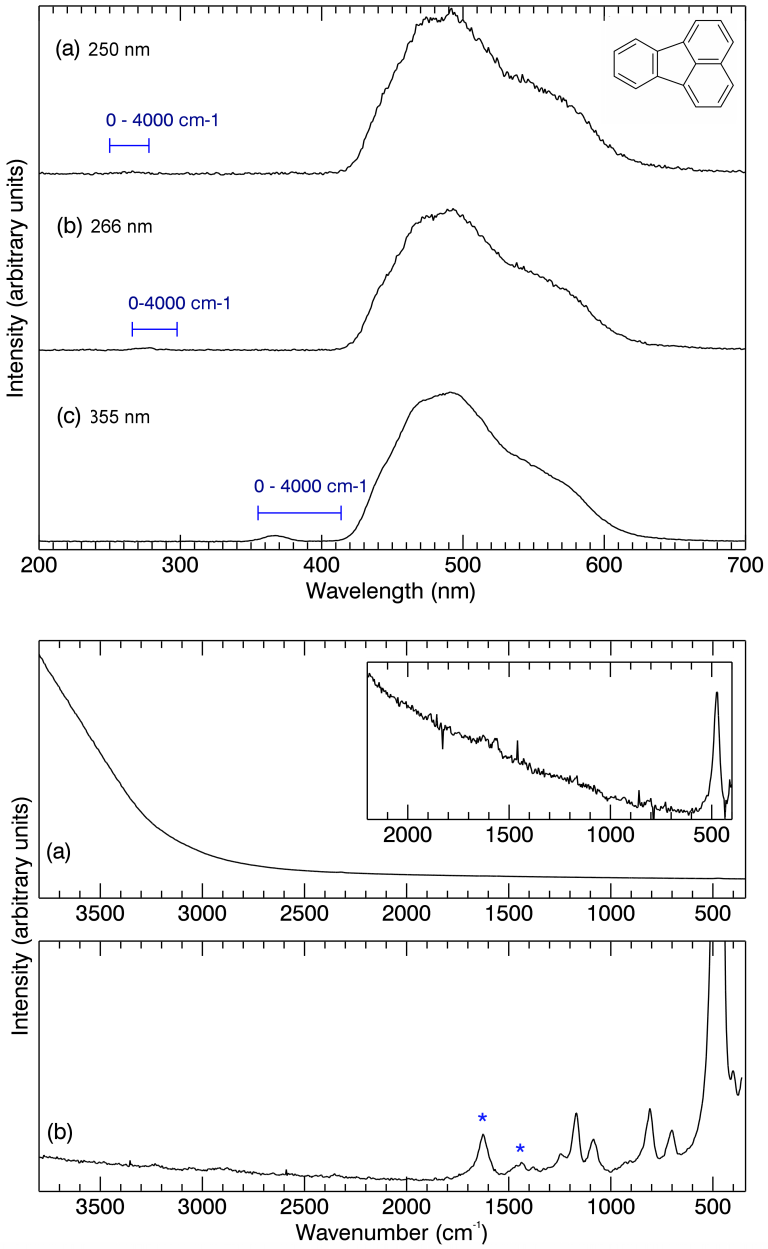

Figure 16: Top: fluorescence spectra of the PAH fluoranthene excited at (a) 250nm, (b) 266nm, and (c) 355nm. A horizontal line denotes the Raman active region between 0 and 4000 cm^{-1}. Bottom: (a) and (b) present the Raman spectra of 0.1% fluoranthene in a silica sand substrate obtained at excitations of 355 nm and 266 nm respectively. A subset of (a) is rescaled in the inset to demonstrate the level of fluorescence observed at 355 nm. Peaks attributable to fluoranthene are indicated with a star. Structural diagrams were created using ChemAxon software.

3.3 Laser induced fluorescence of organic compounds

A Shimadzu RF-551 fluorimeter was used to characterize the fluorescence spectra of a range of organic compounds at three UV excitations of 250 nm, 266 nm, and 355 nm, simulating the fluorescence that could be expected if Raman spectra were obtained with lasers at each wavelength. Fluorescence spectra with a 1 nm resolution were obtained at these fixed excitations over the range of 200 nm to 900 nm, with the goal of determining which excitation wavelength would minimize fluorescence present in the Raman window from 0 cm^{-1} to 4000 cm^{-1}. Organic compounds that were water soluble were dissolved in water at a concentration of 3% to accommodate the 90 degree observation geometry of the instrument. For the organic compounds that were not water soluble, fluorescence spectra were obtained by using silica sand as a substrate.

Fluorescence spectra of the PAH fluoranthene at three excitations are presented in Figure 16 (top). At 355 nm enough fluorescence is present, even in the tail end of the fluorescence band, to dominate the Raman spectra. However, at 266 nm and 250 nm the Raman bands have shifted far enough that no fluorescence will be present in the Raman spectrum. This is directly observed in Figure 16 (bottom), where the fluorescence of 0.1% fluoranthene in silica sand at 355 nm is several magnitudes stronger than the Raman scattering. The quartz bending mode at 475 cm^{-1} is resolvable, but the fluoranthene peaks are undetectable in the increased background. However, when excited at 266 nm, peaks at 1620, 1439, and 1380 cm^{-1} due to in-plane vibrations of the aromatic rings [65, 57] are observed without interfering fluorescence.

A comparison between the fluorescence induced by 266 nm and 355 nm radiation is presented in Figure 17. Significant fluorescence is present in the Raman region of several organic compounds when excited at 355 nm, presented in Figure 17 (top).

This fluorescence was observed both in the fluorescence spectra obtained with the fluorimeter, and in Raman spectra obtained with a 355 nm excitation. Note that artifacts are present in several spectra due to scattered light from the excitation and second order diffraction, and do not originate from molecular fluorescence. As indicated by the fluorescence spectra in Figure 17 (bottom), none of the organic compounds that were tested exhibited significant fluorescence in the Raman region when excited at 266 nm. Lysine and cystine both showed an overall increase in fluorescence at 266 nm compared to 355 nm, as 266 nm radiation induces fluorescence bands not observed at 355 nm. However, these fluorescence bands are predominantly above 297.7 nm, or 4000 cm^{-1}, and therefore we observe reduced interference of the fluorescence with the Raman signal at 266nm.

3.4 266nm Raman spectra of organic compounds

As expected, none of the organic compounds that were tested showed significant fluorescence when Raman spectra were obtained at 266 nm (Fig. 18). Qualitatively, the fluorescence observed in the Raman spectra is in agreement with the amount of fluorescence indicated in Figure 17. The spectrum of lysine contains a small amount of fluorescence, with a magnitude on the order of the Raman intensity. Cystine, which exhibited strong fluorescence at 355 nm, also shows a similar reduction in fluorescence, permitting the weak Raman scattering to be observed. The fluorescence bands induced by 266 nm radiation that are not present at an excitation of 355 nm are located at longer wavelengths and fall outside the Raman region, and therefore do not interfere significantly with the Raman signal.

The most prominent feature observed in the Raman spectra of the organic compounds presented in Figure 18 is the C-H stretching region between 2800 and 3100

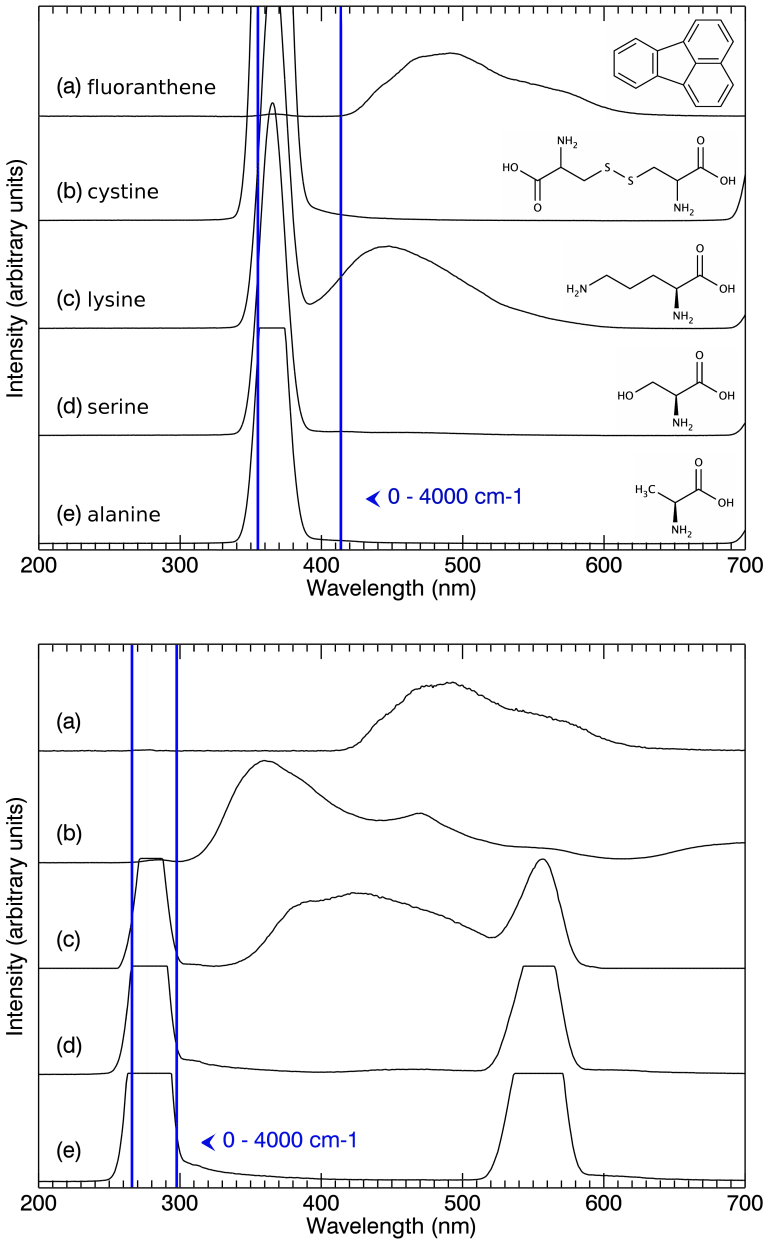

Figure 17: Top: fluorescence spectra of fluoranthene (a), cystine (b), lysine (c), serine (d), and alanine (e) at an excitation of 355 nm. The Raman active area occurs from 0 to 4000 cm^{-1} and is denoted with two vertical bars. Bottom: Fluorescence spectra of fluoranthene (a), cystine (b), lysine (c), serine (d), and alanine (e) at an excitation of 266 nm. The Raman active area occurs from 0 to 4000 cm^{-1} and is denoted with two vertical bars. First- and second-order diffraction artifacts are visible as two strong sharp peaks at 266 and 532 nm which result from scattering of the incident radiation. All other bands in the spectra are related to fluorescence of the molecule. Structural diagrams were created using ChemAxon software.

cm^{-1}. This region contains a complex superposition of symmetric and antisymmetric vibrations attributed to CH, CH_2, and CH_3 functional groups [90, 74], and vibrations of =CH modes are present in this region in aromatic compounds [46]. Assigning these bands to discrete vibrations is further complicated by Fermi resonances in this region that result from the proximity of CH_3 overtones to the fundamental stretching vibrations of CH_3 and CH_2 groups [8].

Figure 18b (top) presents the Raman spectrum of the α-amino acid L-alanine obtained at an excitation of 266 nm. Fig. 18c (bottom) presents the spectrum of L-alanine at a concentration of 1% by weight in a silica sand substrate. The C-H stretching region around 3000 cm^{-1} is very strong, with the band at 2977 attributable to C-H bending in methyl (CH_3) [44]. Further bands due to methyl deformation are visible at 1476 and 1421 cm^{-1}. Bands due to the carboxyl group (-COOH) asymmetric stretch are visible at 1607 cm^{-1}, and symmetric stretch at 1321 and 1373 cm^{-1} [91]. Amine (NH_2) and N-H vibrations are observable at 1607, 1149, 1028, and 664 cm^{-1} [58]. Other bands in the fingerprint region (500 to 1600 cm^{-1}) are due to mixed stretching modes and vibrations involving the structural carbon atoms. The moderate band at 860 cm^{-1} is due to C-N and C-C stretching [44].

The Raman spectrum of the dimeric amino acid DL-cystine was very weak at 266 nm, with the exception of a strong band at 680 cm^{-1}, shown in Fig. 18e (top). Cystine is formed by oxidation of two cysteine molecules, linking with a disulfide (S-S) bond. This linkage is observable in the Raman spectrum, with the S-S stretching band 491 cm^{-1} [100]. The origin of the strong band at 680 cm^{-1} is not clear, however it may tentatively be attributed to C-S stretching, which is expected in this location [27].

The α-amino acid L-lysine, shown in Fig. 18d (top) also exhibits a relatively weak Raman spectrum, and is the only amino acid to show a moderate fluorescent background when excited at 266 nm, at a magnitude around that of the Raman

Compound	Raman Peak Locations (cm^{-1})
Alanine	3276 *(sh)*, **3080** *(sh)*, **2977** *(vs)*, **2755** *(sh)*, 2622 *(w)*, 2515 *(sh)*, 2120 *(w)*, **1607** *(m)*, **1476** *(m)*, **1421** *(m)*, **1373** *(m)*, **1321** *(sh)*, 1149 *(w)*, 1130 *(w)*, 1028 *(w)*, 925 *(vw)*, **860** *(m)*, 780 *(vw)*, 664 *(w)*, 539 *(w)*, 405 *(w)*, 294 *(w)*
Cystine[a]	2961 *(w)*, 1978 *(vw)*, 1585 *(w)*, 1408 *(w)*, 978 *(w)*, 680 *(vs)*, 491 *(w)*
Octacosane[b]	**2893** *(vs)*, **1625** *(m)*, **1446** *(m)*, **1305** *(w)*
Lysine	3361 *(w)*, 3304 *(w)*, **2919** ***(vs)***, 1636 *(m)*, **1428** ***(m)***, 1350 *(sh)*, 1080 *(w)*, 685 *(m)*
Serine[a]	3096 *(sh)*, 2971 *(vs)*, 2746 *(sh)*, 1629 *(m)*, 1475 *(sh)*, 1434 *(m)*, 1334 *(m)*, 1229 *(w)*, 1131 *(m)*, 1013 *(m)*, 885 *(m)*, 680 *(vw)*, 609 *(w)*, 514 *(w)*
Stearic Acid	2896 *(vs)*, 2740 *(sh)*, 2444 *(w)*, 2202 *(w)*, **1658** *(m)*, **1457** *(s)*, **1309** *(m)*, 1174 *(sh)*, **1137** *(m)*, 1072 *(m)*, **882** *(w)*, 681 *(w)*, 568 *(w)*
Silica Sand	**1171** *(w)*, **1084** *(w)*, **809** *(m)*, **685** *(m)*, **470** *(vs)*

Table 4: Raman bands attributable to organic compounds in pure form and at a concentration of 1% in a silica sand matrix. Peaks in bold are observed in both pure and low concentrations. (a) 1% mixtures were not made for two of the compounds, cystine and serine. (b) A pure spectrum of octacosane was not obtained. Spectra were obtained with a 10 minute accumulation time. *vs* - very strong, *s* - strong, *m* - moderate, *w* - weak, *vw* - very weak, *sh* - shoulder.

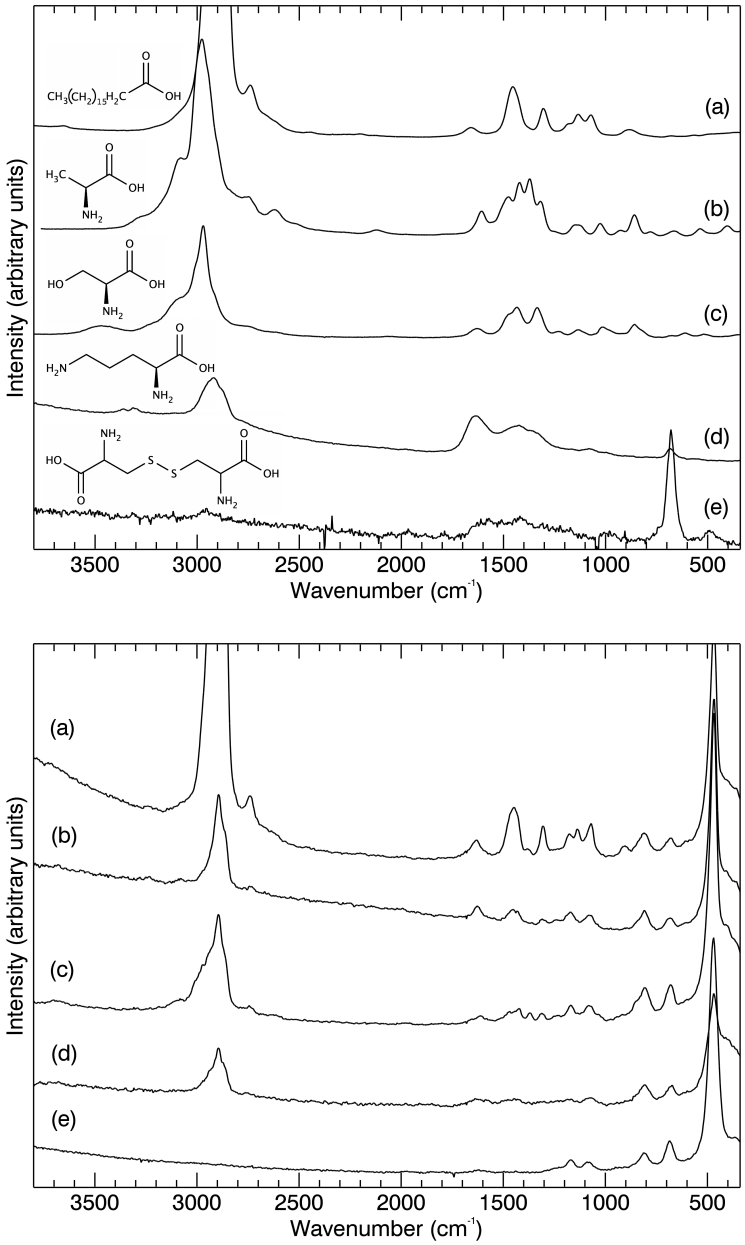

Figure 18: Top: Raman spectrum of stearic acid (a), alanine (b), serine (c), lysine (d), and cystine (e) at 266nm. Bottom: Raman spectrum at 266 nm of 1% concentrations of stearic acid (a), octacosane (b), alanine (c), and lysine (d), with silica sand as a substrate. (e) presents the Raman spectrum of pure silica sand.

intensity. The very strong *vs* peak at 2919 cm^{-1} is due to C-H aliphatic stretching in the backbone of the molecule. Group frequencies characteristic of amino acids are observable, including the carboxyl asymmetric stretch at 1636 cm^{-1}, NH_3 deformation at 1428 cm^{-1}, and CH_2 and NH_2 bending seen in the shoulder peak at 1350 cm^{-1}. The band at 1080 cm^{-1} is attributed to C-N and C-C skeletal stretching [3, 91]. Serine, shown in Fig 18c (top), contains similar bands to the amino acids previously discussed. The region between 3500 and 2600 cm^{-1} contains a complex combination of bands attributed to C-H, O-H, and N-H stretching, as well as a broad band at 3460 cm^{-1}, possibly attributable to adsorbed water due to the hydrophilic nature of the molecule. The *vs* peak at 2971 cm^{-1} and the peaks at 1475 and 1334 cm^{-1} are attributed to C-H and asymmetric CH_2 stretching. Carboxyl vibrations are visible at 1629, 1434, 609 and 514 cm^{-1}, and N-H and ammonium (NH_3) vibrations are present at 1629 and 1131 cm^{-1} [49, 91]. Bending of the hydroxyl (COH) group is observed at 1229 cm^{-1} [49], and skeletal C-C bending and stretching is observed at 885 and 1013 cm^{-1}.

The Raman spectrum of the alkane octacosane at a concentration of 1% in silica sand is shown in Fig. 18b (bottom). The C-H stretch is the most prominent feature at 2893 cm^{-1}. The 1446 cm^{-1} band is interpreted as asymmetrical bending of the methyl groups, and the 1305 cm^{-1} band is interpreted as methylene twisting and wagging [99]. Stearic acid is presented in pure form and at a 1% concentration by weight in Fig. 18a top and bottom respectively. The peak at 1658 cm^{-1} is attributed to C=O stretching in the carboxyl group [61]. In the aliphatic chain, CH_2 twisting and rocking is present at 1457, 1309, and 1174 cm^{-1}, and stretching is observed in the *vs* 2896 cm^{-1} peak. Methyl (CH_3) rocking is observed at 882 cm^{-1}, and bands at 1141 and 1079 cm^{-1} are attributed to C-C stretching [98]. All vibrations of α-quartz that are observable in pure form, shown in Fig. 18e (bottom), are identifiable when mixed with the organic compounds, with the very strong Si-O-Si bending mode at 470 cm^{-1}[82] dominating.

Table 4 lists the Raman bands of each compounds. Peak positions in bold indicate bands that were observable at both pure and 1% concentrations.

A potential downside to the selection of a pulsed ultraviolet laser is the possibility of thermal or photochemical damage to the sample [53, 92]. The spot size and pulse energy used in this work result in a peak power density at the sample of 4.9×10^4 Wcm^{-2} over the duration of one pulse. To determine if this power density could cause thermal damage to the sample over the ten minute measurement interval, the intensity of the Raman bands of 1% mixtures of stearic acid and octacosane were measured while exposed to the laser for a period of two hours. No decrease in Raman intensity was observed, and no additional Raman signal from any breakdown products was detected. Pure L-alanine was also exposed to the laser for a period of two hours, and no change was observed in either the Raman spectra or the visual appearance under microscope inspection. At the low power density and measurement times used in this work, no thermal damage or photolysis was observed in any sample.

3.5 Raman analysis of Mars analogue samples

On Mars any extant organisms or preserved organic material would likely be embedded in a complex mineral matrix. Organic material deposited from meteorite impacts would be sampled by a Raman instrument against a mineral background. These sampling environments are very different from pure compounds and controlled simple mixtures measured in a laboratory setting. Several locations on Earth have harsh conditions that are comparable to the environment found on Mars, and studying the types of organisms that survive in these climates can offer an analogue to possible Martian life. Additional challenges are present in investigating samples from these analogue environments, including locating organic material within a mineral context,

and working with rough topography of a sample. A sample can be considered a good analogue to Mars if it meets two conditions. First, the sample should be similar chemically to samples found on Mars, and second, the sample should be obtained from a location on Earth that experiences harsh environmental conditions similar to the Martian climate.

Unlike pure organic compounds, which exhibit characteristic Raman peaks across the Raman window, complex organics in-situ tend to show less Raman diversity. The Raman spectrum of kerogen, microbial mat, and b-carotene, along with samples of carrot root and parsley leaf, are presented in Figure 19 as examples of complex organics. The kerogen spectrum was collected through a collaboration with Svetlana Shkolyar and Jack Farmer of the School of Earth and Space Exploration at Arizona State University, discussed further in Chapter 5. All of these samples contain arrangements of many types of organic compounds yet all display as the primary Raman feature a broad band located in the 1600 to 1650 cm^{-1} region. This feature is due to C=C and C=O bonds in the organics, and can originate from a variety of bond types, including resonant enhancement of aromatic breathing modes or the fatty acids in the material of cell walls. As this is the primary Raman feature visible in simple biomolecules (b-carotene), active endoliths (microbial mat), and geologically preserved organics (kerogen), it is also the Raman feature that was sought in the subsequent analogue studies as an indication of organic carbon. Virtually no minerals or inorganic compounds have vibrational energies in the 1650 cm^{-1} region, and therefore the observation of this band is a good indication that organic material is present.

3.5.1 Overview of Mars analogue environments

While no location on Earth provides true Mars-like conditions, several locations serve as analogues to different time periods in Mars' evolution, shown in Figures 20, 21,

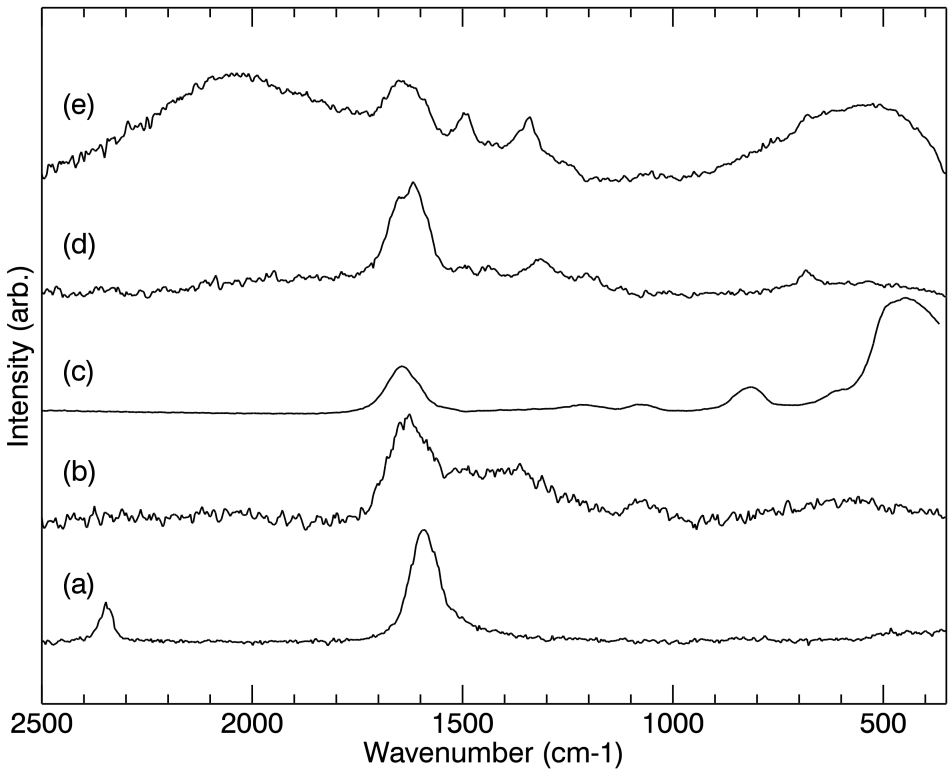

Figure 19: Raman spectra of a range of biomolecules, microbes, and geologically preserved complex organics. (a) kerogen, (b) microbial mat, (c) b-carotene, (d) carrot root, and (e) parsley leaf. The primary Raman band in the 1600 to 1650 cm^{-1} region is found in all samples, and is likely due to both C=C and C=O stretching and breathing modes in the organic.

and 22. The Canadian Arctic, with low temperatures ranging from -36 ºC to +5 ºC, is a good analogue for studying early Martian habitability, when liquid water was presumed to be present in significant quantities, the atmosphere was thicker, and a magnetic field was present [33].

Axel Heiberg island, home to the McGill Arctic Research Station (M.A.R.S.) since 1960, is one of the most active Mars analogue research sites. From this station, located in a cold dry region at 80° north, the north Canadian Arctic is accessible, allowing investigation of perennial springs that exist in climates similar to a Martian environment. The springs have a high salt content derived from significant amounts of sedimentary material, and serve as good locations to study extremophile bacteria in an environment similar to what early Martian life may have encountered [5]. Springs have been observed in this environment that are composed of brines sufficiently salinated to remain a liquid at temperatures of -15 ºC, close to the Martian surface temperature. After flowing through 600 meters of permafrost, the salty brines reach the surface and form springs that maintain temperatures above the freezing point [5, 75].

In Mars' later era, the atmosphere thinned and the planet became dry. With temperatures averaging -60 ºC, and arid soil containing oxidizing material and perchlorate salts, life would have needed to adapt to harsher conditions to survive. The Atacama desert, a large plateau on the west coast of South America covering 1000 km [113], provides a good analogue for a dry Mars. Atacama soils have likely been arid for over 10 million years, and contain oxidizing material including perchlorates in similar quantities compared to Martian soil [33]. Low or no organic matter is found in some regions of the Atacama, highly unusual for Earth soil. Areas of the Atacama are considered the driest on Earth, and can experience virtually no precipitation for years or decades [26]. Microbial life in the Atacama must contend with this arid environment, and pockets of microbial communities can be found in the crust of porous

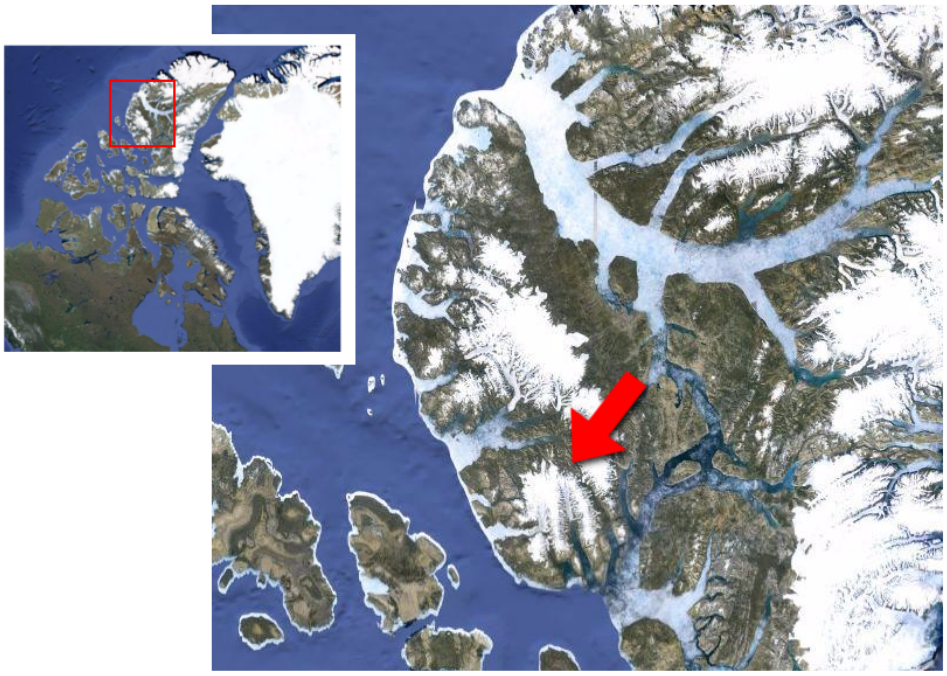

Figure 20: Axel Heiberg Island, Canadian Arctic. Source: Google Earth.

minerals such as gypsum and halite [108].

Another good analogue for a dry Mars are the Dry Valleys in Antarctica. The permafrost, subsurface ice, and dry environment are similar to conditions in some Martian climates. The McMurdo dry valleys possibly offer the best Mars analogue site available on Earth, as the rocky, dusty, permafrost-covered environment is similar to conditions observed at the Phoenix landing site [4]. Studying the extremophile bacteria that survive in these types of environments can improve our understanding of Martian habitability, and samples from these environments are useful to demonstrate instrumentation intended for detecting signs of life elsewhere in the solar system.

Figures 23 and 25 present images of the analogue samples selected for testing, composed of a range of sedimentary minerals containing endolith colonies. Figure 24 presents photographs of the sample locations, showing the environment from which

Figure 21: Atacama Desert, Chile. Source: Google Earth. Top arrow: Salar Grande, bottom arrow: Yungay.

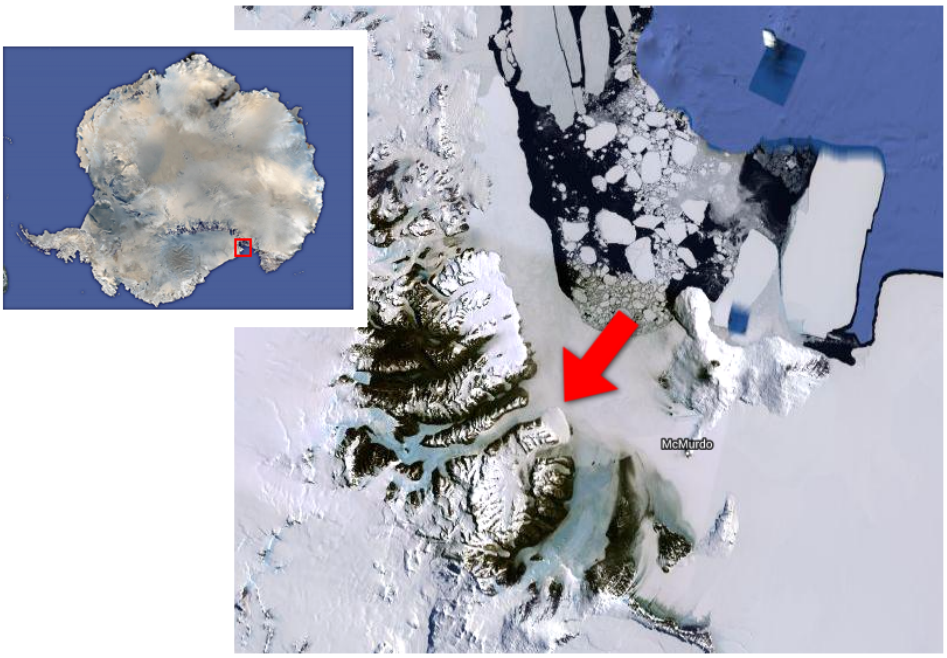

Figure 22: Dry Valleys, Antarctica. Source: Google Earth.

the samples were obtained. Figure 24 (a, b) presents images of the Yungay and Salar Grande regions of the Atacama Desert. A description of the field activities that led to the acquisition of these samples is available in Ziolkowski et al. (2013) [118]. Colonized gypsum and ignimbrite were collected from the Monturaqui region of the Atacama, while colonized halite was collected from Salar Grande and Yungay. Samples were collected in May, 2009 by Lori A. Ziolkowski at McMaster University using a rock hammer. The samples were sealed with a desiccant in sample bags and stored at room temperature for ten days, then placed in a freezer and stored at -20°C. Figure 24 (e, f) presents images of the McMurdo Dry Valleys in Antarctica. Colonized sandstone samples were collected in January, 2013 by Jackie Goordial at McGill University using a clean rock hammer, gloves, and sterile sampling bags. Samples were frozen and shipped to McMaster University, where they were freeze dried and kept in a freezer until analysis. Antarctic samples were obtained from two locations, University Valley and Farnell Valley. A photograph of Axel Heiberg in the Canadian Arctic is shown in Figure 24 (c). Colonized gypsum samples were collected from Axel Heiberg in July, 2012 by Michael Daly and Michael Ilnicki at York University. Samples were placed in ziplock bags and transported at room temperature to York University, where they were frozen along with a desiccator.

All rock samples were kept in bags and frozen with a desiccator when not in use. In order to minimize organic contamination, which could affect the Raman signal and likely would significantly affect the fluorescence signal, the samples were not handled except with fresh nitrile gloves. Endolithic colonies are indicated by a green color, primarily due to the presence of cyanobacteria. In some cases, such as the Axel Heiberg samples, microbial colonization is visible from the surface of the sample. In other cases, colonization occurs below the sample crust a few millimeters and can only be observed from the side of a broken face of the sample. The depth of colonization can

be dependent on several environmental factors, including temperature and humidity, and can vary on the order of millimeters [113].

3.5.2 Raman mapping of Mars analogue samples

To obtain 2D Raman maps of rocks and other analogue samples, samples were placed on a three-axis motorized stage. LabVIEW software automates data acquisition by controlling the timing of the detector and motion of the sample stage. A detailed overview of the software, developed for this work, is available in Appendix 8.3. As datasets can be composed of upwards of 2500 individual spectra, acquisition times are ideally limited to less than twenty seconds. A two second delay was required between measurements to move the sample to the next position. Complete datasets with a 50x50 map resolution were obtained by this automated system in approximately 7-9 hours.

Mapping resolution on a flight instrument may be limited by the spot size and angular resolution of the pan-tilt mount supporting the sensor head containing the laser and optics. On the breadboard instrument, controlling the laser spot size and the motor step distance simulates this specification. As the breadboard geometry is close to a 180° backscatter geometry (approximately 160°), variations in the sample texture and surface roughness do not significantly affect the optical alignment with the laser spot.

Figure 26 presents a Raman map of a sample containing gypsum, quartz, and endoliths from the Canadian Arctic (sample shown in Figure 23 A). The sample was found to have a predominantly quartz base, on which endolith colonization was supported in a porous gypsum layer. Raman maps were generated plotting the point of maximum intensity of a single characteristic Raman peak in each compound. The 1015 cm^{-1} gypsum peak, 475 cm^{-1} quartz peak, and 1650 cm^{-1} endolith peak were used

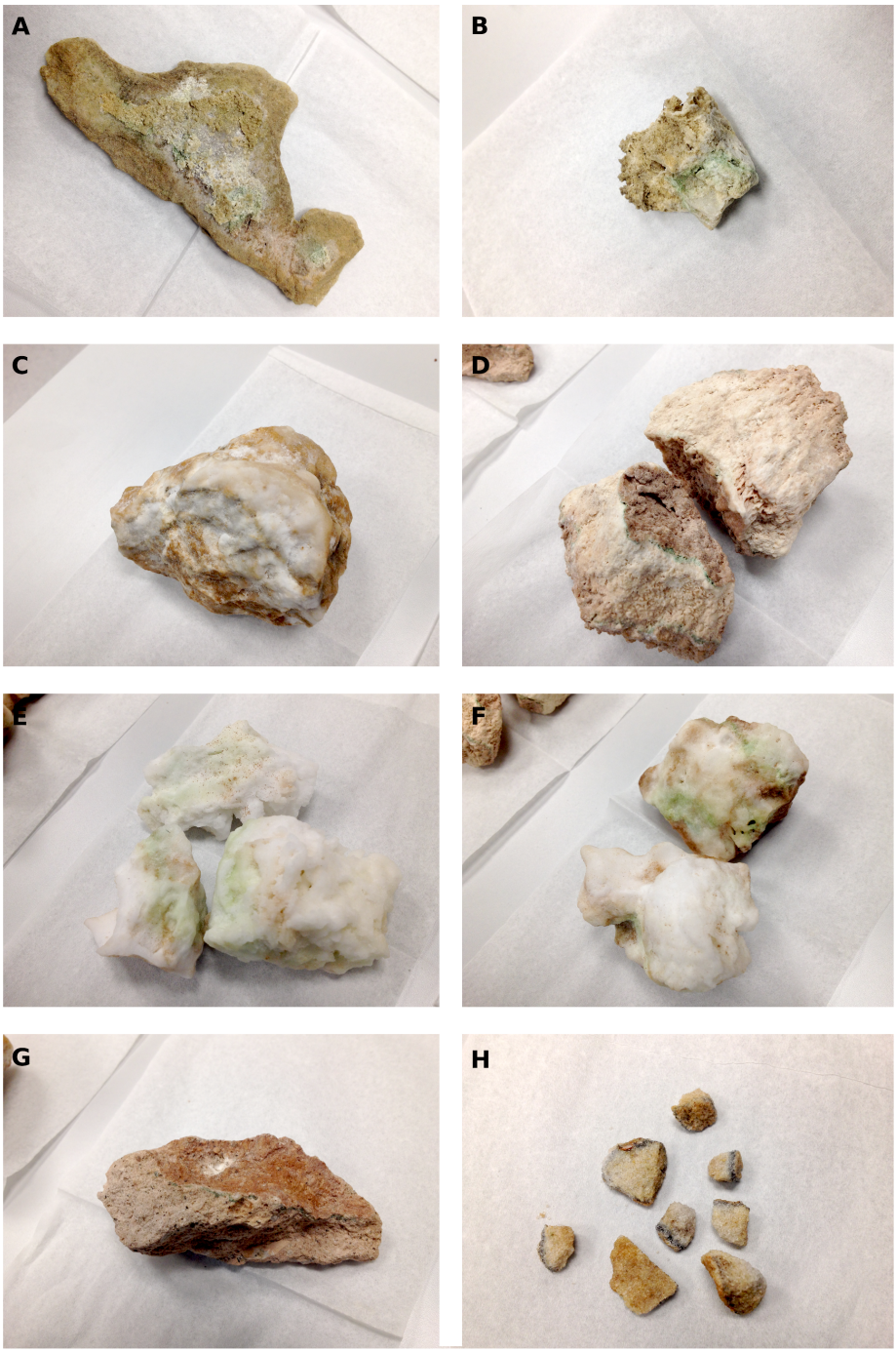

Figure 23: Endolith samples from the Arctic, Antarctica, and Atacama Desert. (A,B) Gypsum and endoliths from the Canadian Arctic, (C,D) gypsum and endoliths from the Atacama Desert, (E,F) halite and endoliths from the Atacama Desert, (G) ignimbrite from the Atacama Desert, and (H) sandstone and endoliths from Antarctica.

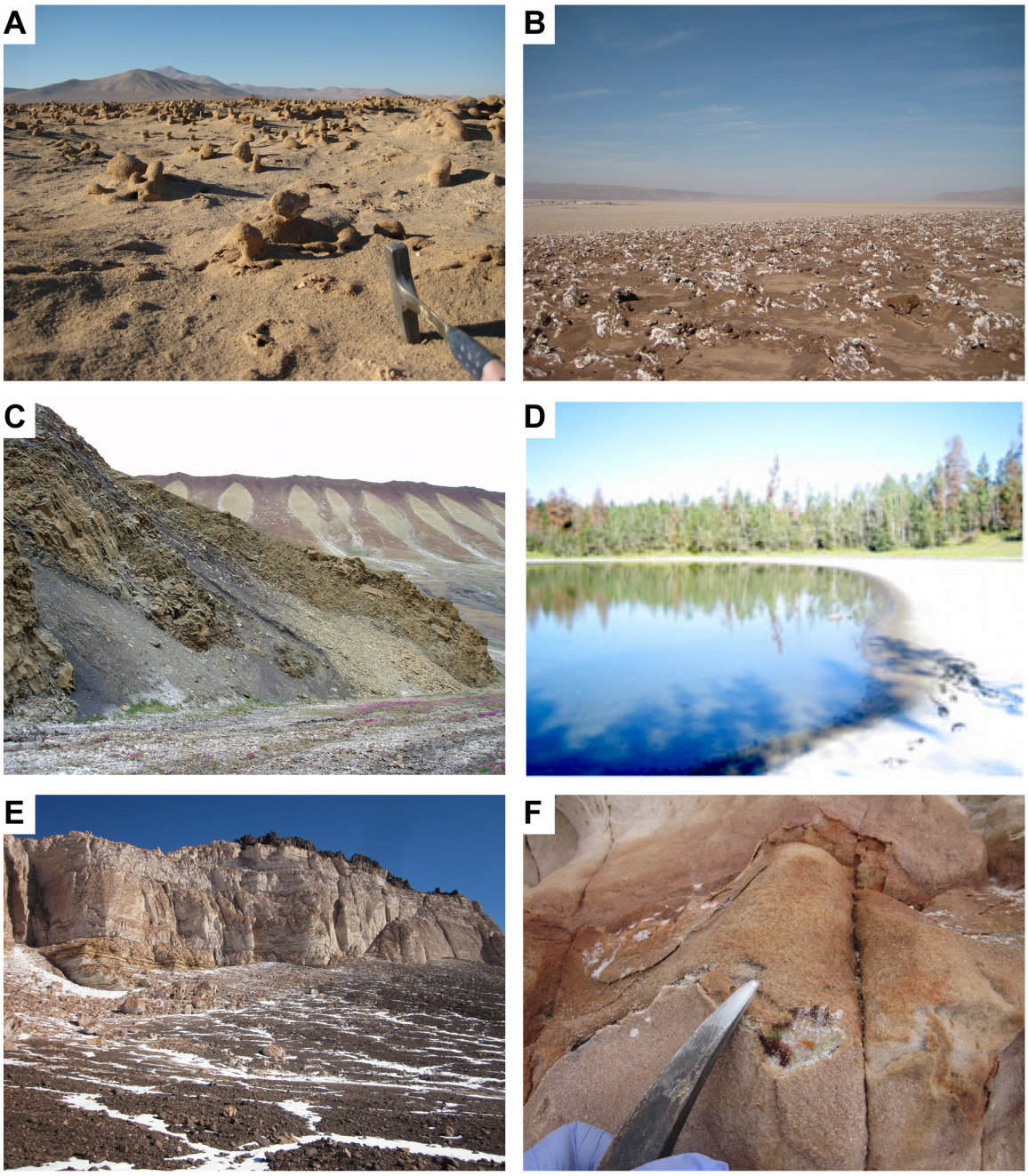

Figure 24: Images from field expeditions to Mars analogue environments are presented of the Atacama Desert showing Yungay (a) and Salar Grande (b), Axel Heiberg in the Canadian Arctic (d), Probe Lake (d), and the McMurdo Dry Valleys in Antarctica (e), (f). Photo credit: (a), (b) Gregory Slater, McMaster University; (c) Michael Daly, York University; (d) Allyson Brady, McMaster University; (e), (f) Jackie Goordial, McGill University, and Margarita Marinova, NASA Ames.

Figure 25: Images from field expeditions to Mars analogue environments are presented of the Atacama Desert showing collection of (a) ignimbrite, (b) Yungay gypsum, and (c) Salar Grande gypsum. Photo credit: Gregory Slater, McMaster University

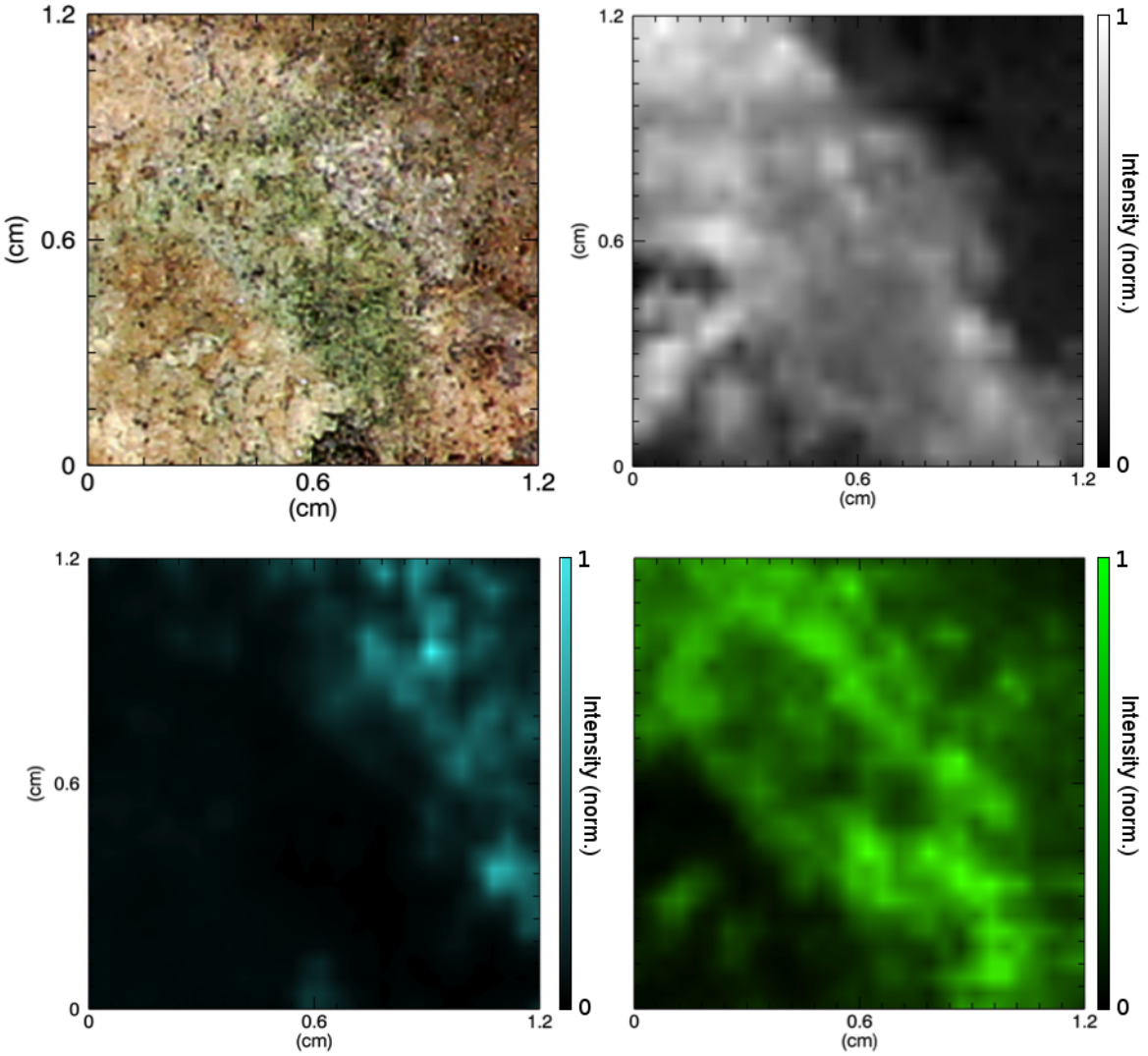

Figure 26: Gypsum and cyanobacteria from the Canadian Arctic. Raman maps are presented of gypsum (white), quartz (blue), and cyanobacteria (green). Raman maps were generated by plotting the intensity of a single Raman peak, with each map individually normalized to the peak height. The sample was unprepared, sampled in the state in which it was obtained from the field. Mapping was performed with a 0.4 mm spot size.

to generate the maps as they were the strongest Raman features in each compound. The intensity scale of each map was normalized to the value of the highest peak. The figures correspond visually with the camera image of the sample, and serve as a qualitative validation that the map scaling and orientation methodology was applied correctly.

Several Raman maps are presented in Figure 27, all of samples with a primarily gypsum and quartz matrix. The top map presents a region of Atacama gypsum from the Yungay region of the desert. In this sample, while gypsum and a quartz grain were observed, there was no organic content detectable by the 266 nm instrument. The Yungay region of the Atacama is the most arid, and samples from this region contain the lowest levels of organic content. The sample presented in Figure 27 middle is from a less arid region of the Atacama, and microbial colonization is visible. Raman features were strongest in areas that appeared devoid of surface dust and areas that appear more porous, while much of the map contains low or no levels of Raman signal. An X-ray fluorescence (XRF) study was performed on several points across the sample, on locations with and without strong Raman signal, in an effort to determine why large regions yielded no Raman signal, however the XRF measurements did not reveal any significant differences in the composition of different locations. It may be the case that, as the sampling depth of the ultraviolet laser is likely on the order of microns or less, even small quantities of surface dust may block observation of the bulk sample if the dust absorbs at the laser frequency. A possible source of this absorption could be the iron content in the Atacama soil, which can strongly attenuate ultraviolet light. Figure 27 bottom presents gypsum, quartz, and organic content of a sample from Axel Heiberg island in the Canadian Arctic. As with the previous samples, organic and mineral signatures are most detectable when not covered by any surface dust. Raman maps in Figure 27 were generated similarly to Figure 26.

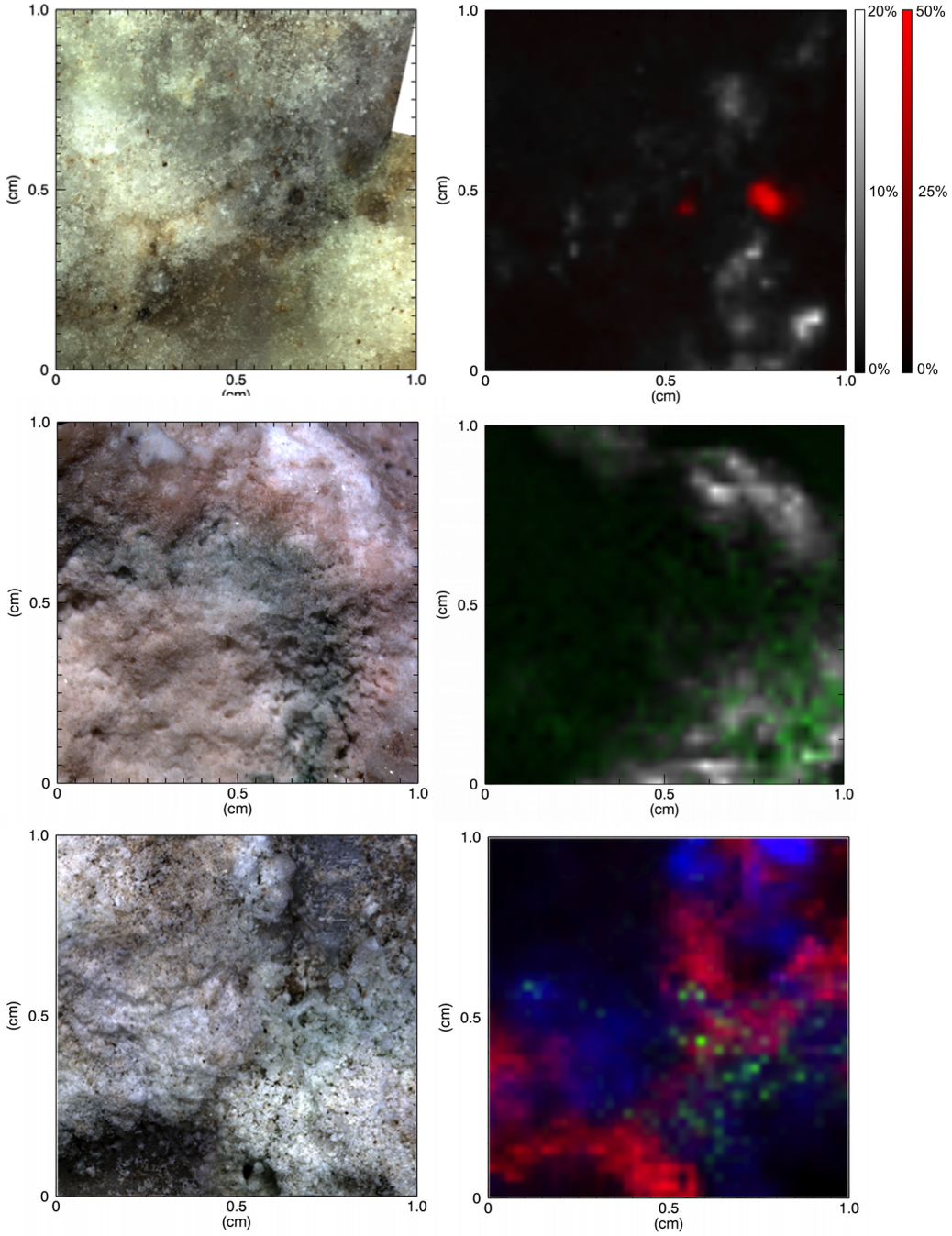

Figure 27: Top: Endoliths in a gypsum and quartz matrix from the Atacama Desert. Red and white colors correspond to the relative intensities of quartz and gypsum respectively. Middle: Another example of Atacama gypsum (white) and endoliths (green). Bottom: Gypsum (blue), quartz (red), and organic material (green) from the Canadian Arctic. Spatial axes on the Raman maps match the corresponding image in the left column. The color bars in the top map were generated by a Partial Least Squares calibration model developed from pure gypsum and pure quartz in controlled mixtures.

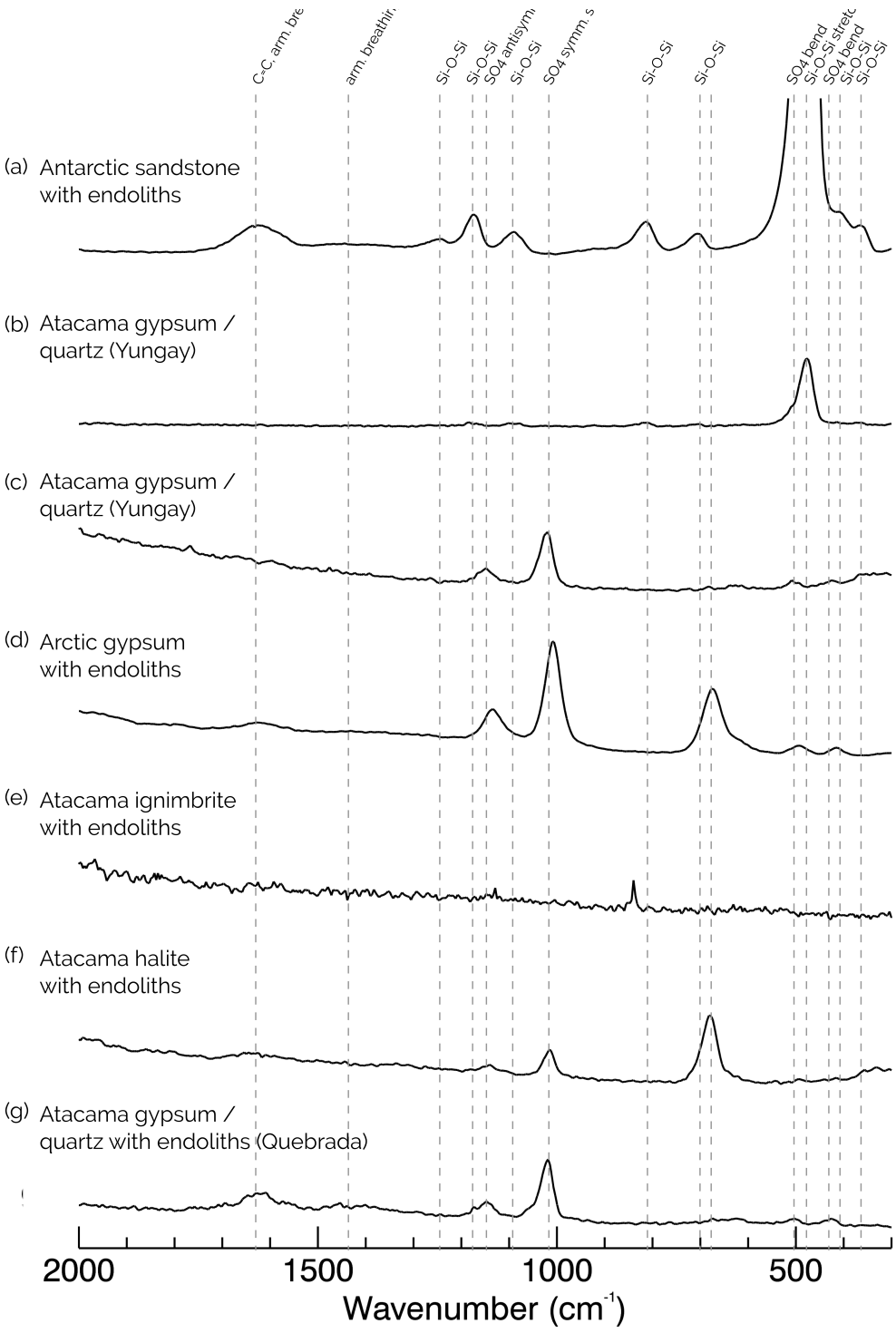

Figure 28: Representative Raman spectra of Mars analogue samples containing endoliths

A summary of the Raman spectra obtained from these samples is presented in Figure 28. Observed Raman features are attributable to the primary constituents of the samples; gypsum, quartz, and endoliths. In all cases the mineral matrix and organic distribution could be well mapped, with the exception of ignimbrite. Ignimbrite is composed of volcanic ash with a high glass content, and strongly absorbs in the ultraviolet. Despite visible regions of endolith colonization, the Raman signal of these regions did not display a significant organic signature.

It is desirable to extract as much information as possible from map datasets, which can be composed of hundreds or thousands of spectra. Multivariate techniques, which make use of the entirety of the spectral information, can provide increased sensitivity to trends in the data compared to univariate methods. The color bars in Figure 27 top were generated by a Partial Least Squares calibration model developed from pure gypsum and pure quartz in controlled mixtures. The application of a PLS model to the Raman dataset, composed of 2500 individual spectra, allowed the relative percentage of the two compounds to be determined at each spot in the sample. This was accomplished by measuring controlled mixtures of pure gypsum and quartz to generate a calibration model, and then regressing each spectrum from the Raman map against the model to determine the relative percentages of each constituent. Appendix 8.2 provides a detailed overview of the PLS algorithm used for this analysis.

The Raman maps generated in Figures 26 and 27 were constructed by visually inspecting the data for strong Raman peaks and with prior knowledge of the sample composition. With an unknown sample, or if a small grain of an interesting feature occupies one or two spectra out of thousands, it may be difficult to visually inspect the dataset for interesting features. Principal Component Analysis (PCA) may be applied to such datasets as an unsupervised first-look, and can provide information concerning the interesting features of the data. Figure 29 presents the first three principal

components of the Atacama Yungay dataset. Two vectors in principal component space represent the two physical components of the rock, the gypsum and quartz. Additionally, a third arm composed of only three or four spectra extends separately from the primary features. These spectra were determined to have a Raman signal of gypsum, but have a fluorescence background profile not found in other regions of the sample. This feature would potentially be worthy of follow up investigation, and would likely have been missed if the 2500 spectra in the dataset were investigated visually. Unlike traditional PCA analysis, where groupings of large numbers of data points are crucial for classification, outliers in PCA space in this application represent areas that are potentially the most interesting. The primary targets of investigation, organic compounds, are expected to be very localized and confined to sub-mm or micron scales, and therefore may present as outliers in PCA space, indicating that the spectral profile of those points contained information that was significantly different from the bulk sample.

3.6 Summary

Interference from fluorescence can significantly constrain detection of organic material in the Raman analysis of *in situ* samples. A stand-off Raman spectrometer operating on Mars with similar specifications to the UV system presented in this work would be expected to obtain spectra from a mm-scale field of view containing signatures from a complex matrix of organics and minerals. Trace and rare earth elements would likely result in mineral fluorescence in addition to fluorescence from the organics themselves, limiting the detection of organic matter when fluorescence is present. Several organic compounds tested at an excitation of 355 nm, comprised of a range of amino acids, fatty acids, alkanes, and PAHs, showed significant fluorescence in the Raman spectra

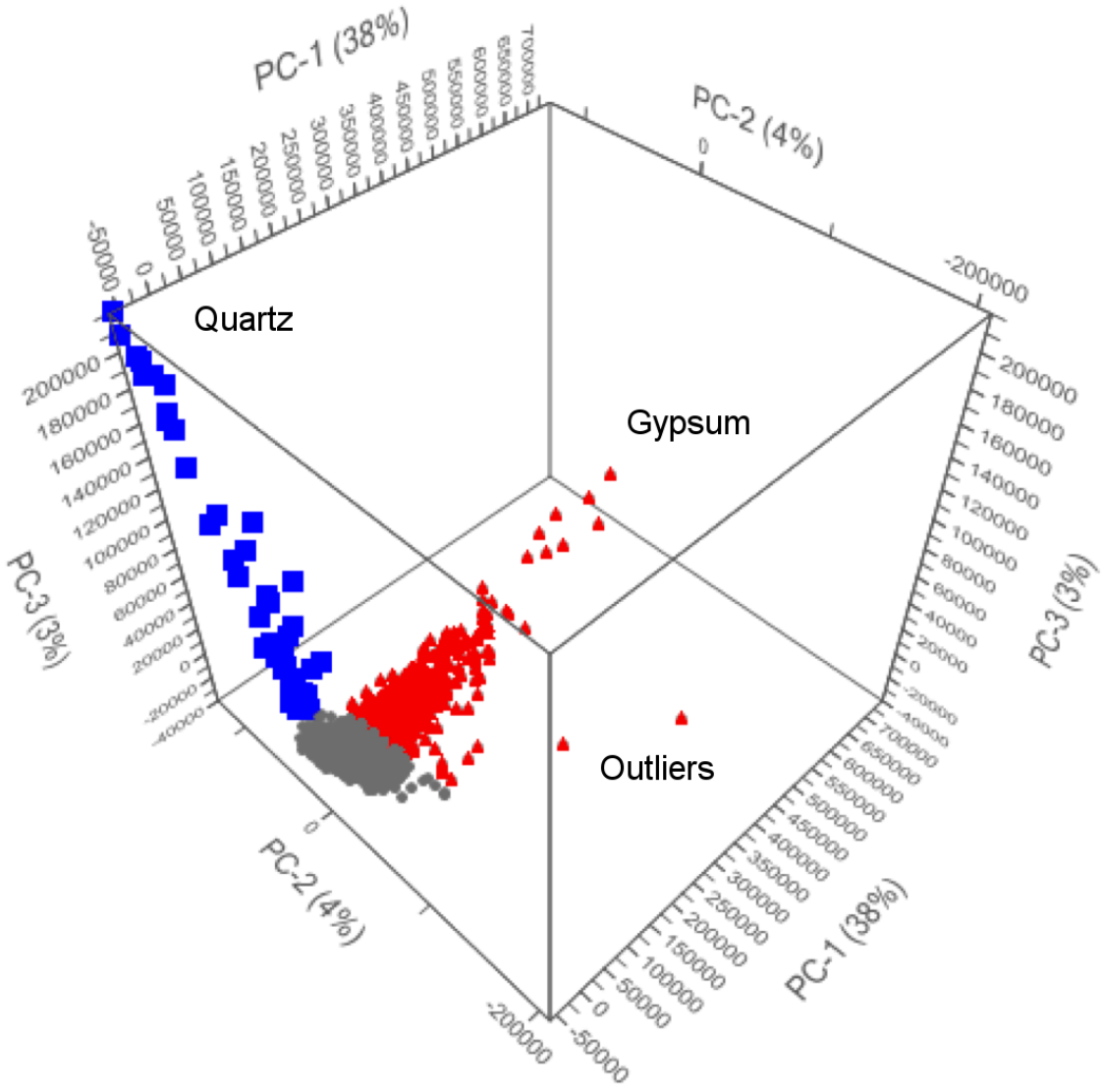

Figure 29: PCA analysis of a gypsum and quartz sample from the Atacama Desert. The first three principal components are plotted, with gypsum (red) and quartz (blue) marked. The three axes represent the first three principal components, describing most of the variation observed in the dataset.

Compound	Solvent / substrate	Fluorescence observed in		Fluorescence observed in Raman spectra at 266 nm
		Raman spectra at 355 nm	fluorometer spectra	
Alanine	Distilled water	No	No	**No**
Cystine	Distilled water	Yes	Yes	**No**
Fluoranthene	Silica sand	Yes	Yes	**No**
Lysine	Distilled water	Yes	Yes	**No**
Octacosane	Silica sand	No	No	**No**
Serine	Distilled water	No	No	**No**

Table 5: Expected and observed fluorescence in organic compounds at 355 nm and 266 nm excitations

that affected the ability to discriminate the Raman bands. We have showed that this fluorescence can be significantly reduced by moving to a 266 nm excitation, with a summary of the findings presented in Table 5. In all cases investigated, the Raman spectra at 266 nm demonstrate that fluorescence is either removed or reduced to a magnitude approximately equal to the intensity of the Raman scattering.

While moving deeper into the UV to 250 nm would completely remove all fluorescence, a 266 nm wavelength may be obtained with Nd:YAG lasers, which have significant flight heritage and are proven in a space environment (e.g. [112, 89, 1]). Additionally, the small amount of fluorescence that is observable in the 266 nm window may be useful. Further study is needed to determine if the the fluorescence observed above 2000 cm^{-1} can provide additional information regarding the presence of organic matter.

4 266 nm laser-induced fluorescence of organic compounds and minerals

This chapter presents work adapted from the following peer-reviewed published article

> E. Eshelman, M. G. Daly, G. Slater, P. Dietrich, and E. Cloutis. Time-resolved detection of aromatic compounds on planetary surfaces by ultraviolet laser induced fluorescence and Raman spectroscopy (2015) Planetary and Space Science, 119, pp. 200-207

and demonstrates the potential to perform sub-ns fluorescence lifetime measurements of Mars-relevant organics and minerals using an intensified detector with fast gating capabilities and a short laser pulse. A method is presented for measuring fluorescence lifetimes that allows mineral and organic fluorescence to be separated, and lifetime measurements are presented for aromatic amino acids, PAHs, and mineral-organic mixtures to demonstrate the utility of this techniques applied to Mars relevant samples. This chapter demonstrates how this technique, traditionally performed in a laboratory, can be adapted to a planetary surface.

4.1 Introduction

Upcoming and future ultraviolet Raman instruments are likely to incorporate laser-induced fluorescence (LIF) capabilities, as these capabilities can be added for modest cost and accommodation increases [86, 47]. The minimum photon energy needed to induce fluorescence in a compound is equivalent to the energy difference between the highest occupied molecular orbital (HOMO) and lowest unoccupied molecular orbital (LUMO). Energies in the ultraviolet are sufficient to meet this gap for a wide range of organic compounds, especially compounds with aromatic rings containing de-localized

Figure 30: Blue fluorescence visible from a calcite sample

π electrons [96]. Many complex organics therefore exhibit strong fluorescence when excited with ultraviolet radiation. This laser induced fluorescence may be several magnitudes stronger than the Raman scattering, yet the emission spectrum is Stokes-shifted to longer wavelengths [94], with generally all fluorescence occurring above 270 nm [11]. Fluorescence will therefore be energetically separated from the Raman window if an excitation of 266 nm or lower is selected [32].

Unlike Raman scattering, which occurs on a femtosecond timescale, fluorescence emission occurs on the nanosecond timescale, or greater. Many organic compounds exhibit strong short-lived fluorescence when excited with ultraviolet radiation, while some minerals exhibit longer lived fluorescence [14], which can be due to the presence of transition metals or rare earth impurities [42]. Fast fluorescence (a lifetime less than < 10 ns) is considered a potential biosignature due to its probable organic origin. In this chapter it is shown that if a fast time-gating (FTG) capability is used with an intensified detector and a short laser pulse, it is possible to obtain sub-ns fluorescence

lifetime measurements of Mars-relevant organics and minerals using instrumentation with specifications similar to a flight instrument. While not achieving the time resolution of traditional laboratory CCD imaging, time correlated single photon counting (TCSPC), [111] or other lifetime measurement techniques [105], the method presented here may be performed in-situ on a planetary surface without greatly adding to the complexity of a combined Raman and fluorescence instrument. This serves a primary purpose of discriminating mineral from organic fluorescence. Additionally, this may assist in determining if more than one fluorescing species is present and provide information concerning the molecular structure as well as the context of the sample. The nanosecond timescale of fluorescence emission is sufficient to allow chemical reaction of the excited molecules with the local environment, which can affect both the emission wavelength and lifetime through quenching mechanisms [59]. FTG also improves the system capabilities and operational utility by allowing the removal of the majority of the fluorescence background from the Raman signal and reducing the effect of ambient light. Combining fluorescence and Raman measurements results in an instrument with the discriminating power provided by Raman spectra and increased sensitivity to organic material due to the high cross section of fluorescence, potentially allowing detection of organic material to ppb scales [95].

4.2 Sample preparation

Three aromatic amino acids, L-phenylalanine (Sigma-Aldrich P2126), L-tyrosine (Sigma-Aldrich T3754), and L-tryptophan (Sigma-Aldrich T0254) were obtained in pure form from Sigma-Aldrich. The lifetimes of these compounds are well defined in the literature [59], and therefore they serve as good lifetime standards to calibrate and verify the measurement methodology. Time-resolved spectra of the aromatic amino acids

were obtained by first dissolving the compounds in distilled water at a concentration of 0.001% by mass, as lifetime values are typically reported in the literature for aqueous solutions. The resulting solutions were placed in fused-silica quartz cuvettes, which do not exhibit fluorescence when excited with 266 nm radiation. Minimal Raman scattering from Si-O-Si stretching modes is present in the quartz [82], but it is several magnitudes weaker than the fluorescence scattering and is restricted to below 500 cm^{-1} (269.5 nm) and does not overlap with the fluorescence emission. Four Mars-relevant polycyclic aromatic hydrocarbons (PAH) 9-nitroanthracene (Sigma-Aldrich N1020-9), dibenzothiophene sulfone (Sigma-Aldrich D3240-7), phenoxathiin (Sigma-Aldrich 21882-0), and phenoxazine (Sigma-Aldrich P1485-8) were also obtained from Sigma-Aldrich in pure powdered form with a sub-45 μm grain size. The PAHs were placed in powdered form into disposable UV cuvettes for testing. The disposable cuvettes used are highly transparent to UV light, and do not exhibit significant fluorescence. As the cuvettes are constructed from an organic polymer, a C-H Raman stretching mode is visible around 3000 cm^{-1} [60], but does not interfere with fluorescence lifetime measurements. Research grade calcite was obtained from Ward's Science to investigate mineral fluorescence described in Section 3.3. Microbial mat from Probe Lake in the Cariboo Plateau, British Columbia was mixed with the calcite to generate a sample displaying both mineral and organic fluorescence. The microbial mat was composed of 60-65% carbonate inorganic phases, with the remaining organic content dominated by cyanobacteria [17]. The mixed sample contained 1% microbial mat by dry mass, resulting in an organic concentration of 0.35 ± 0.05%. Figure 24 (d) presents a photograph of Probe Lake. A description of the field activities that sampled the mat is available in Brady et al. (2013) [17]. Samples were collected in 2008 over a period of several months at a location away from the shoreline, and stored in combusted organic-free glassware. Samples were transported on dry ice, and stored

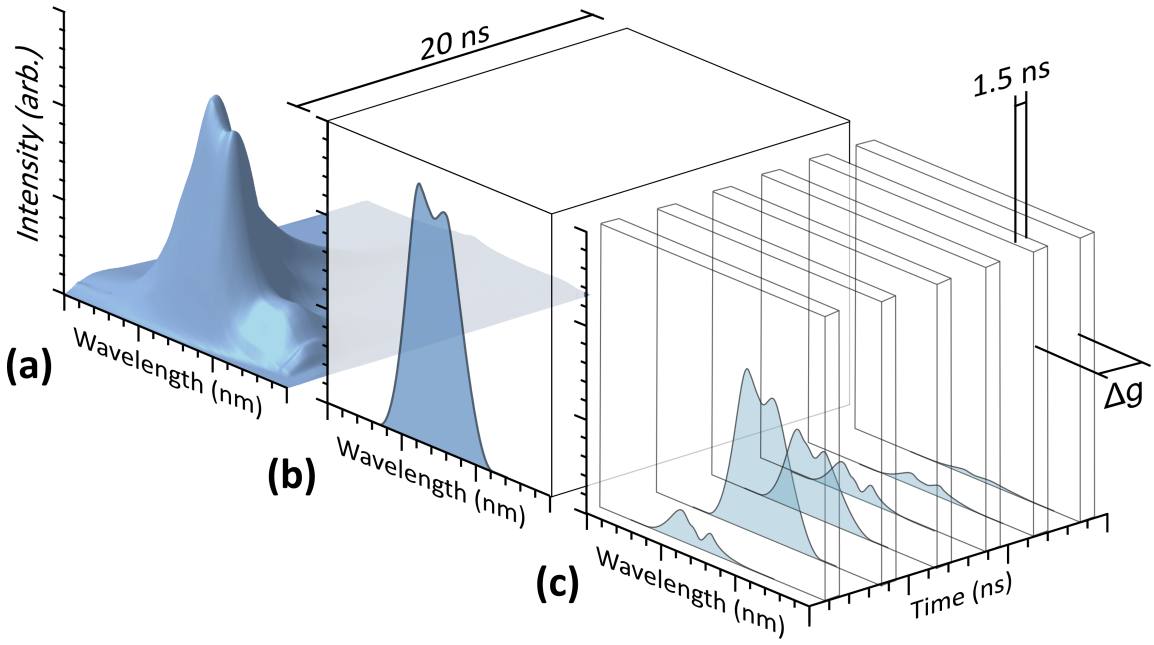

Figure 31: Diagram depicting time-resolved measurements performed by the ICCD detector. In (a) a typical fluorescence spectrum is shown, evolving in time over 20 ns. A single-spectrum measurement may be performed (b) by opening the detector gate for a period of 20 ns and capturing all incoming photons. Alternatively, a time-resolved measurement may be performed (c) by using the minimum gate width of 1.5 ns and taking subsequent acquisitions with a time delay increaseng by $\triangle g$ between each measurement.

in freezer when not under analysis.

4.3 Time-resolved fluorescence measurements

Photons entering the detector first strike a photocathode, producing photoelectrons that are amplified in an intensifier before arriving at the CCD. Controlling the voltage across the photocathode determines whether photoelectrons will be produced, and therefore serves as a fast electronic gate [104]. The Andor iCCD was used for this work that has a minimum gate width of 1.5 ns and an irising time on the scale of tens of picoseconds. An additional parameter, the gate delay, coordinates opening the gate with the arrival of the laser pulse by applying an electronic delay after receiving the

external trigger signal. A detailed overview of the measurement process is described in Section 2.2

A spectrum is typically produced by accumulating signal from several thousand pulses, and time-resolved measurements may therefore be obtained by incrementing the gate delay between subsequent spectra. A depiction of this measurement method is shown in Figure 31. In Figure 31 (a), a typical fluorescence profile is shown decaying over a period of 20 ns. A single-spectrum measurement may be performed by setting the detector gate width to a relatively wide value and capturing all incoming photons. Alternatively, a time-resolved measurement may be obtained, shown in Figure 31 (c), where the detector gate is minimized and multiple acquisitions are performed, each with a subsequent offset in time to capture a different time segment of the decay profile. In this work the gate delay was incremented by 0.1 ns between 200 acquisitions to observe decreasing fluorescence intensity with time. The subsequent dataset of 200 spectra can be viewed top-down as a contour plot to visualize the fluorescence evolution in time.

4.4 Fluorescence lifetime calculation

Fluorescence lifetime, τ, is the average time a fluorophore will remain in an excited state, with the intensity of fluorescence emission decreasing exponentially over time. The intensified CCD, pulsed laser, and gated detector which form the foundation of the Raman instrument also allow for measurement of fluorescence lifetimes with a time resolution below 1 ns. This is fast enough to discriminate organic fluorescence, which typically occurs on a time-scale of 1-10 ns. During acquisition of a Raman spectrum the detector gate and delay are set to ensure that the detector opens to capture the Raman scattered light and to minimize the fluorescence and ambient

light. By minimizing the gate width and increasing the gate delay incrementally, the acquired spectra provide a time-domain picture of the decay of the fluorescence with a resolution determined by the optical width of the gate and the gate delay. Fluorescence spectra presented in this work were obtained using the minimum possible optical gate width of 1.5 ns in order to maximize the time resolution. Calculating a lifetime value can be accomplished by modeling decay curves with different lifetimes using a measured laser pulse shape and detector gate profile. Experimental decay profiles may be fitted to the model using a partial least-squares multivariate regression to determine the best fit. Partial least squares (PLS) modeling was performed using the chemometric software package The Unscrambler X .

4.4.1 Modeled fluorescence decay

A molecule with a fluorophore that exhibits a single decay time that is excited by an ideal δ-function would produce fluorescence that follows an exponential decay. The form of the decay is shown in Equation 29,

$$I(t) = I_0 e^{-t/\tau} \tag{29}$$

where the fluorescence intensity $I(t)$ at time t is determined by the initial intensity I_0 and the lifetime τ. When measuring fluorescence using a fast time-gated approach with a pulsed laser, the emitted fluorescence is not a pure exponential decay, but a decay profile that is the convolution of the laser pulse shape with the exponential decay function. The convolution integral for the laser profile and idealized decay from Equation 29 is presented in Equation 30,

$$f_{\text{laser}}(t) \star f_{\text{decay}}(t) = \int_0^t f_{\text{laser}}(x) f_{\text{decay}}(t-x) dx \tag{30}$$

and is used to generate the fluorescence decay profile that results from excitation by a non-ideal laser pulse shape at time t. This may be thought of as summing the fluorescence profiles of all the delta excitation functions that occur within the shape of the laser pulse. The laser pulse shape was measured by an oscilloscope with a measurement rate of 20 Gs/s and a rise-time of under 150 ps, coupled with a fast photodetector with a 40 ps rise-time. A baseline correction, a linear fit to the spectrum extents, was applied to the laser profile in order to prevent the background signal from introducing errors when convolved with the decay function. In addition to the effect of the laser pulse shape, the detector itself has a minimum gate width of 1.5 ns. Each spectrum that composes the dataset therefore represents a fluorescence measurement not at a discrete time, but over a 1.5 ns time window. The detector is gated by controlling the voltage across a phosphor, and therefore may be opened much more rapidly than would be possible with a mechanical shutter. As the irising time for the phosphor is on the order of tens of picoseconds, the gate profile may be approximated as a square wave with a 1.5 ns width. The measured signal at the detector is therefore an additional convolution of the laser and ideal decay function with the detector gate profile. Equation 31 may then be applied to determine the expected measured decay:

$$f_{\text{observed}}(t) = (f_{\text{laser}} \star f_{\delta\text{decay}}) \star f_{\text{gate}} \tag{31}$$

A series of fluorescence decay curves for various lifetime values was calculated and used to generate a partial least squares (PLS) calibration model, using the method

described in Section 4.4.1. A PLS calibration composed of twenty decay profiles with a 0.5 ns lifetime step is shown in Figure 32. In this application the matrix **X** contained the modeled lifetime decay spectra and the matrix **y** contained the lifetime values for each decay curve. In this case, five latent variables were selected to describe how the decay spectra change with the fluorescence lifetime.

4.4.2 Lifetime calculation by partial least squares fitting

Experimental data may be applied to the model generated by Equation 31, determining the lifetime value and fit error. In order to fit experimental data to the model, the data must have a baseline correction applied and be normalized to the scale of the model. Additionally, an instrument response function (IRF) must be applied to account for variations in the measured intensity as a function of the measurement delay. Unlike a traditional IRF, which is commonly measured over the time scale of the excitation pulse and using the shape of the pulse itself [63], the iCCD detector has an IRF that depends on the delay value set in the digital delay generator. It is therefore necessary to measure the instrument response not just for the duration of an excitation pulse, but on a time scale approaching the length of the lifetimes that will be measured. This measurement of the IRF was accomplished by measuring the constant output of a blue led, shown in Figure 11. As the detector gate is stepped forward in time, the intensity of the blue LED remained constant and a correction factor was calculated based on the measured intensity as a function of gate delay.

4.5 Lifetime measurements of the aromatic amino acids

In order to validate the procedure described above for calculating fluorescence lifetimes, the PLS calibration of the modeled decay profiles was applied to time-resolved

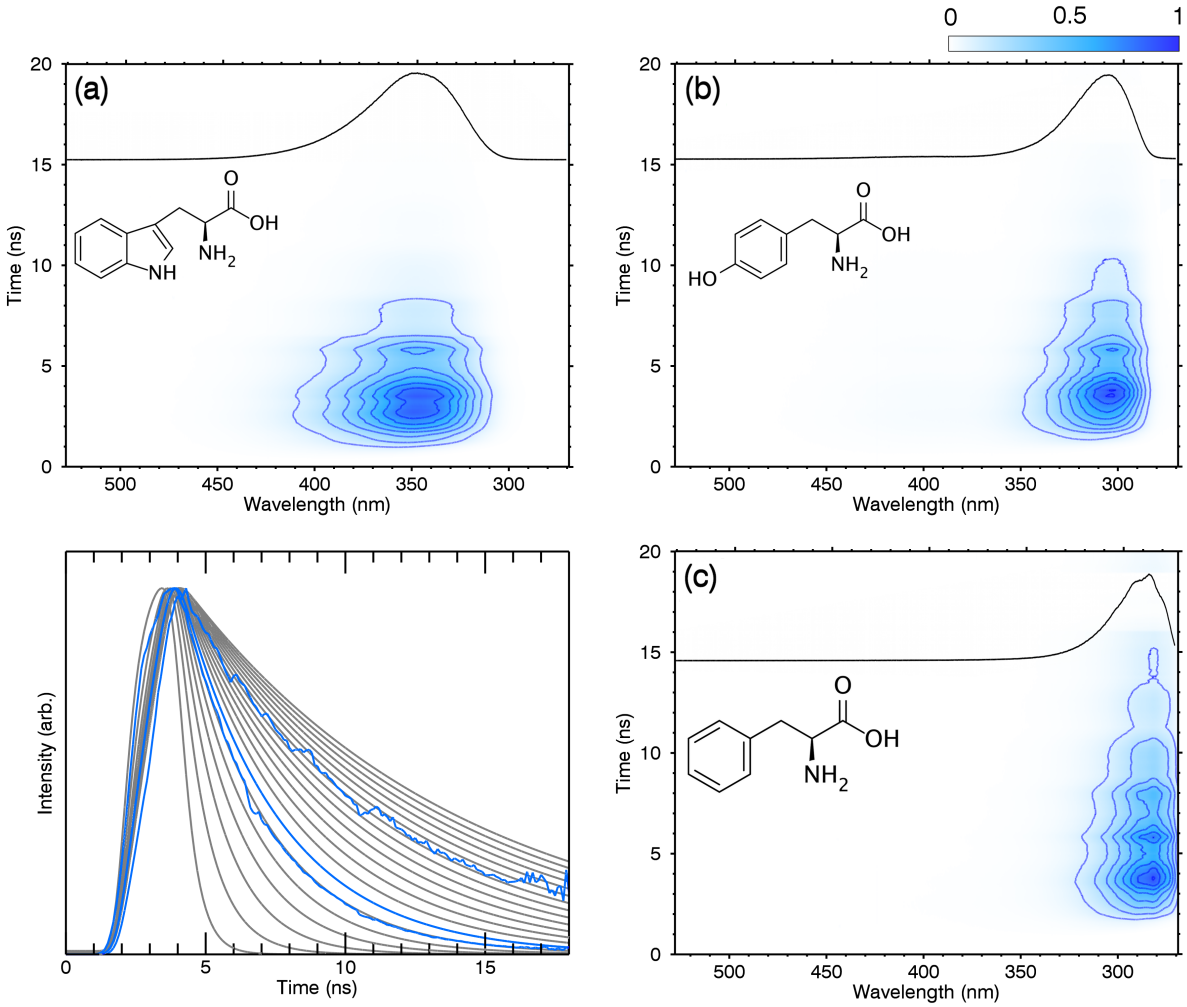

Figure 32: Time-resolved normalized fluorescence decay profiles of the aromatic amino acids (a) tryptophan, (b) tyrosine, and (c) phenylalanine. The bottom left plot presents modeled decay curves (grey) generated from the convolution of the laser pulse with the detector gate and exponential decay profiles. Corrected decay curves of the aromatic amino acids are overlaid in blue. Single spectra are overlaid at the top (a-c), and were obtained with a 1.5 ns gate width at the time of maximum intensity. Molecular diagrams were created using ChemAxon software.

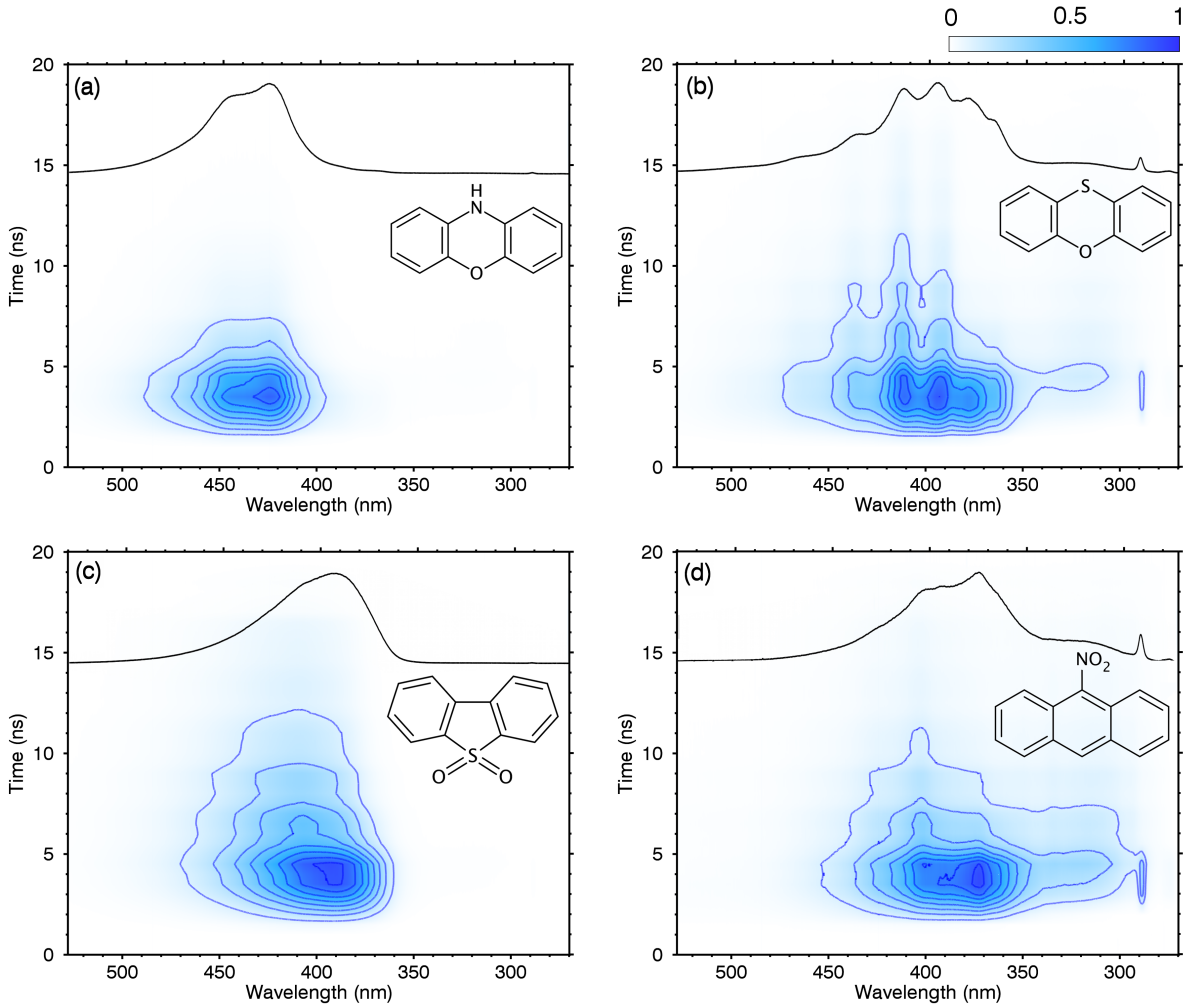

Figure 33: Normalized decay profiles of the PAHs (a) phenoxazine, (b) phenoxathiin, (c) dibenzothiophene sulfone, and (d) 9-nitroanthracene. In (b) and (d), Raman scattering from C-H stretching in the cuvette polymer is visible around 289 nm. Single spectra are overlaid at the top of each plot, and were obtained with a 1.5 ns gate width at the time of maximum intensity.

Compound	Lifetime (ns)	Lifetime [literature] (ns)	λmax (nm)	λmax [literature] (nm)
phenylalanine	7.3 ± 0.3	6.8	288	282
tyrosine	3.4 ± 0.2	3.6	307	304
tryptophan	2.8 ± 0.2	3.1	355	353
phenoxazine	2.2 ± 0.2	-	424	-
phenoxathiin	4.7 ± 0.2	-	465, 436, 412, 391, 365	-
dibenzothiophene sulfone	4.0 ± 0.2	-	393	-
9-nitroanthracene	5.0 ± 0.2	-	372	-

Table 6: Lifetime measurements and emission maxima of the aromatic amino acids and four PAHs. Measured values are compared against lifetimes and peak emission values (λmax) from the literature if available [59].

measurements of the three aromatic amino acids - phenylalanine, tyrosine, and tryptophan in aqueous solutions. The lifetimes of these compounds are well characterized, with variation in published lifetime values of a few tenths of nanoseconds (e.g. [59, 71, 2]). The decay profiles are presented in Figure 32 (a,b,c), along with a spectrum of the fluorescence at the time location of maximum intensity. Figure 32 (bottom-left) shows the modeled decay curves used to generate the PLS model (grey), and the experimental decay profiles of the aromatic amino acids (blue) after correction due to the instrument response function. The lifetimes calculated from the PLS model are shown in Table 6, along with values obtained from the literature. The wavelength of maximum emission is reported as well, along with the corresponding literature values.

The aromatic amino acids, in addition to their usefulness as a lifetime reference, are also molecules that have strong astrobiological relevance [69, 76]. These compounds are essential for life on Earth [35, 78], and much of the ultraviolet fluorescence that is observed in extremophile bacteria can be attributed to fluorescence from the aromatic amino acids in proteins, primarily tryptophan residues [22]. Measured

lifetime values are close to values reported in the literature. The larger fit error for phenylalanine may be due to the longer lifetime, as the correction factor applied to the instrument response function is most accurate for spectra obtained at shorter lifetimes. Accurate measurements of longer lifetimes, including mineral fluorescence would require an IRF measured over a time period on the order of the lifetime of interest.

4.6 Fluorescence of PAHs

Although no definitive polycyclic aromatic hydrocarbons (PAHs) have been detected on Mars, they are expected to be present on the surface and the recent detection of the aromatic compound chlorobenzene [56, 39] motivates the search for more complex organics. PAHs can form abiotically in the interstellar medium [30], and can be present in carbonaceous chondrites at levels above 1000 ppm [48, 23], several orders of magnitude above the limit of detection using fluorescence based techniques. PAHs have been detected in Martian meteorites [9], although whether the organics are of Martian origin has not been resolved. While PAHs have many different forms, with varying numbers of rings, side groups, and substitutions, all PAHs generally exhibit strong fluorescence when excited with UV light due to the easily excitable delocalized π electrons present in the aromatic rings [96]. Phenoxazine, phenoxathiin, dibenzothiophene sulfone, and 9-nitroanthracene were selected to demonstrate the potential for lifetime measurements on this class of Mars-relevant organics. Spectra were obtained with a ten second integration time, and a 0.1 ns gate step. Fluorescence decay was measured for twenty nanoseconds beginning one nanosecond prior to excitation by the laser pulse. The fluorescence decay profiles are shown in Figure 33, along with the fluorescence emission spectra from 268 nm to 528 nm, obtained at the time of max-

imum fluorescence intensity. Differences in the fluorescence lifetimes are resolvable, with a lifetime range of 2.2 ns to 5.0 ns.

4.7 Discriminating between mineral and organic fluorescence

As minerals typically fluoresce on longer timescales than organic compounds, the fast gating ability of the detector can discriminate between organic and mineral fluorescence. The time-resolved emission spectrum of a mixed sample containing calcite, an astrobiologically relevant mineral [77], and 1% microbial mat by weight is presented in Figure 34. Raman scattering, organic short-lived fluorescence, and mineral fluorescence are presented in Figure 34 (left). Raman scattering at 1086 cm^{-1} is attributable to the stretching of the carbonate ion [52], and is observed as a small feature in the lower right of Figure 34 (left) and expanded in Figure 34 (top-right). Without the ability to gate on a nanosecond scale, the origin of the fluorescence would be ambiguous, shown in Figure 34 (middle-right). With gating of the detector all emission longer than 6 ns can be rejected, shown in Figure 34 (middle-right) (b), and fluorescence due to the microbial mat can be observed. Much of the fluorescence below 400 nm observed in the microbial mat is due to aromatic amino acids bound in proteins [24]. Typically the strongest emission features in proteins are due to tryptophan residues, as tyrosine and phenylalanine fluorescence is quenched through energy transfer or other mechanisms [59]. The longer lifetime fluorescence that is emitted from the calcite is due to the presence of the cerium Ce^{3+} ion [88], and has an emission maximum at around 375 nm. Fast time gating results in a greater ability to identify short-lived fluorescence, considered a potential biosignature. The high cross section of fluorescence, especially with an ultraviolet excitation, allows a combined Raman-fluorescence instrument to rapidly identify the presence of organic material

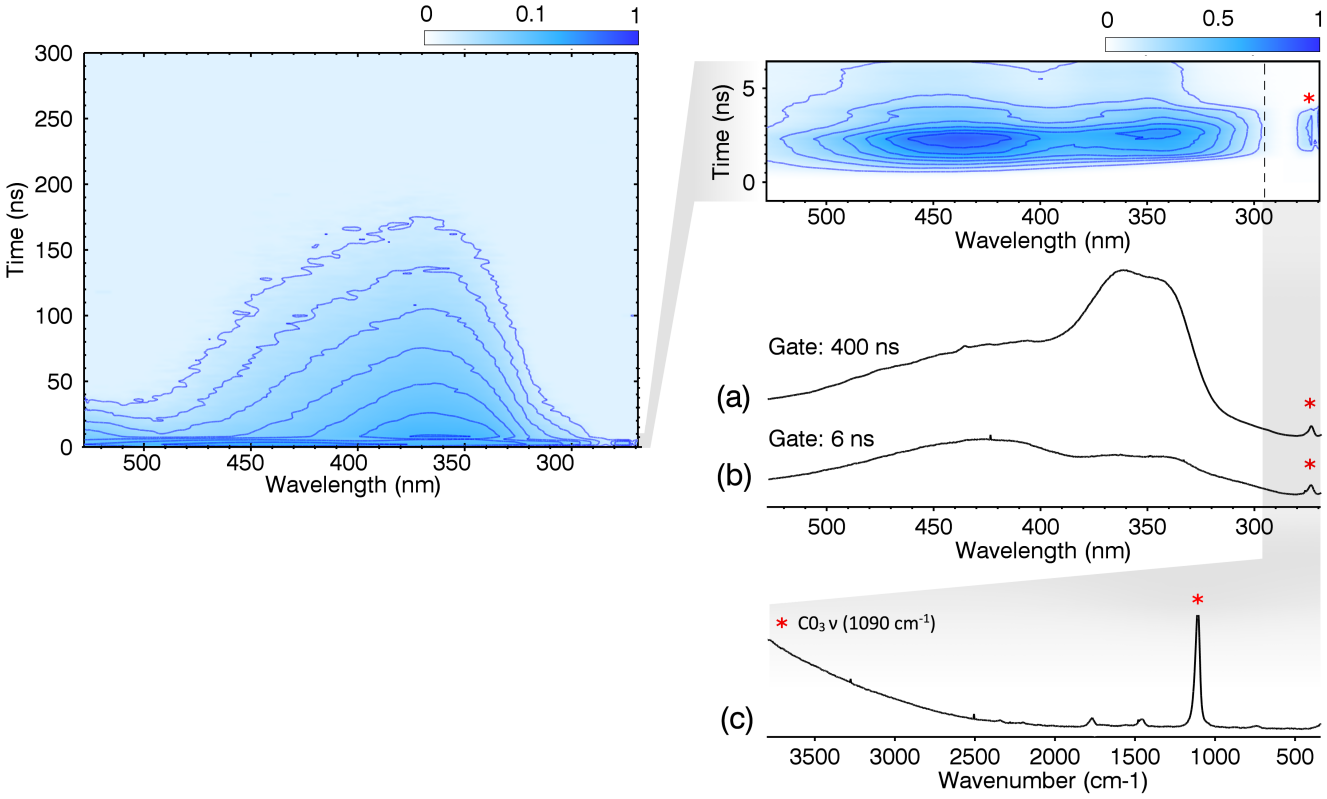

Figure 34: Left: Time-resolved fluorescence of calcite over 400 ns. Intensity is presented on a log scale to emphasize the mineral fluorescence due to the cerium Ce^{3+} ion, which is weaker than the short-lived organic fluorescence due to the microbial mat. Top-right: Decay scaled over 8 ns, presented on a linear scale. The Raman peak due to the stretching mode of the carbonate ion is visible and noted with a star. Bottom-right: (a) calcite spectrum obtained with a 400 ns gate, simulating an ungated acquisition, and (b) a 6 ns gate demonstrating the rejection of mineral fluorescence and unambiguous detection of short-lived fluorescence. A vertical bar and vertical shaded grey area denotes the Raman window which extends to 3800 cm^{-1}. (c) presents the Raman spectrum of the calcite sample.

by observing short-lived emission under 10 ns. With a 266 nm excitation nearly all of the fluorescence occurs outside the Raman window, shown in Figure 34 (c), and a subsequent Raman acquisition can be obtained in order to fingerprint the compound.

4.8 Summary

A combined Raman and fluorescence instrument has a higher sensitivity to organic carbon compared to a Raman instrument alone. We have demonstrated that if a fast time-gating (FTG) approach is coupled with a combined Raman and fluorescence instrument, it is possible to obtain fluorescence lifetime measurements on the nanosecond time scale of Mars-relevant organics and minerals. This combined measurement capability potentially allows for organic detection from fluorescence at the ppb level, and organic fingerprinting using the Raman signal at a ppm level. The ability to measure fluorescence lifetime offers several potential advantages, especially when applied in a planetary setting where other laboratory techniques are not available. Mineral and organic fluorescence can be separated, allowing for unambiguous detection of short-lived fluorescence, a strong potential biosignature. For a compound that has been identified either through a Raman or fluorescence spectrum, the additional measurement of fluorescence lifetime can provide further information concerning the local environment, as the nanosecond timescale of fluorescence permits nuclear motion and the interaction of a molecule with its neighbors. As organic fluorescence is produced alongside Raman scattering with ultraviolet excitation, instrumentation that combines both capabilities increases the chances of detecting organics on the Martian surface. Fast time-gating is also applicable to Raman instruments that make use of visible or near-IR excitation wavelengths, as the majority of the fluorescence that interferes with the Raman signal at these longer wavelengths can be rejected.

The results in this chapter motivate future work in cataloging a wider variety of PAHs by measuring the Raman, fluorescence, and fluorescence lifetime signatures. A larger catalog of samples may lead to an understanding of how the fluorescence lifetime can be related to the molecular properties of PAH and how the lifetime is affected by Mars-like conditions, ultimately leading to fast-gating capabilities in future flight instruments.

5 Geolocating and discriminating organic compounds in-situ with time-resolved fluorescence

This chapter builds on the techniques developed in Chapter 4 for measuring fluorescence lifetimes in-situ by applying the methodology to a suite of 24 PAHs of varying complexity. Composed of structures with multiple rings, side groups, and substitutions, these PAHs represent the types of organic compounds that could be present on Mars and elsewhere in the solar system. The primary purpose of the chapter is to demonstrate that incorporating time-domain (e.g. fluorescence lifetime) measurements allows PAHs to be better differentiated from other PAHs and from matrix fluorescence. Fluorescence has been proposed as an efficient method for locating organic material on an unknown surface, as measurements may be obtained on the order of seconds, while Raman measurements of comparable sensitivity could take tens of minutes [10]. A fast scan may therefore be performed using fluorescence techniques, and subsequent points of interest could be further investigated with single-point Raman acquisitions. This chapter provides a case study of this technique applied to a stromatolite sample containing preserved organic material in a mineral matrix, demonstrating the significant benefit offered by time-resolved measurements in locating probable organic fluorescence.

The results presented in Section 5.5.2 were obtained through a collaboration with Svetlana Shkolyar and Jack Farmer of the School of Earth and Space Exploration at Arizona State University. The collaboration occurred over a two week period. Data was collected at York University using the 266 nm Raman system in the Planetary Instrumentation Laboratory using samples provided by ASU. All subsequent analysis that is presented in this Chapter was performed for this work.

5.1 Introduction

As any organic material on Mars is expected to be scarce and localized to regions with scales on the order of microns, methodologies for locating organics that are both sensitive and rapid will be highly valued. Fluorescence is often significantly more intense than Raman scattering, and strategies for organic detection have proposed generating fluorescence maps containing a few hundred points, and using the observed features to guide the acquisition of lengthier Raman measurements to conclusively identify the C-H, C=C, and C=O bonds that confirm the presence of organic material [47, 10]. Successful detection of organic compounds using this methodology is therefore contingent on the ability to interpret rapidly obtained fluorescence spectra for features indicative of organics. As many minerals exhibit fluorescence due to impurities and rare-earth elements, differentiating between mineral and organic fluorescence is highly valuable in situations, like a Mars rover, where time-consuming Raman spectra must be judiciously obtained.

In this chapter we present time-resolved measurements of a suite of 24 PAHs. The wide diversity of the fluorescence spectra demonstrate that fluorescence measurements alone may be sufficiently discriminatory to characterize single PAHs, if present on the Martian surface. Time-resolved measurements were contrasted against single-spectrum measurements to show how time-domain measurements allow increased differentiability. PAH fluorescence was shown to occur over a wide window, extending from ultraviolet to visible wavelengths, and instruments with constrained windows of detection may need to carefully locate their window with certain targets in mind. Finally, a case study was conducted of fluorescence mapping performed on a Mars analogue stromatolite. Time-resolved measurements allowed short-lived fluorescence to be identified and separated from mineral fluorescence, reducing the number of sam-

pling spots that would be good candidates for subsequent Raman measurements and increasing the likelihood of organic detection.

5.2 Sample preparation

A selection of 24 PAHs, listed in Table 7 along with chemical diagrams, were obtained from Sigma-Aldrich. Previous work on these samples by Cloutis et al. [19] characterized the 532 nm Raman spectra, visible fluorescence spectra, and UV absorption of the samples. The samples were obtained in powdered form, with grain sizes less than 45 μm ranging in purity from 95% to greater than 99.5%. A quantity with a volume greater than the laser spot size (0.5 mm^2) of each PAH was placed into low-fluorescence polycarbonate disposable UV cuvettes in order to ensure that the sampling surface would be larger than the laser spot. This procedure was performed under a fume hood due to the toxicity of the majority of the PAHs. The fluorescence of the polycarbonate cuvettes was measured and confirmed to be very weak. While the cuvettes display strong Raman scattering, the Raman peaks are restricted to the Raman window below 290 nm, and therefore do not interfere with the majority of the PAH fluorescence. The strongest Raman feature, the 3000 cm^{-1} C-H stretch, is located at 289 nm and serves as a reference peak against which PAH fluorescence can be normalized and the relative intensities compared. The time-resolved fluorescence spectra of several mineral standards were measured in pellet form. Minerals were crushed and pelletized to remove the effect of fluorescence due to surface contamination. An example pellet is shown in Figure 35.

Time-resolved and single fluorescence spectra were obtained using the 266 nm Raman system described in Chapter 2. Single fluorescence spectra were obtained with 10 ns gate widths, and time-resolved datasets were obtained with the shortest possible

Compound	Sigma-Aldrich	Structure
Naphthalene	18,450-0	
Anthracene	14,106-2	
2,3-Benzanthracene	B240-3	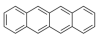
Phenanthrene	P1,140-9	
1,2-Benzanthracene	B220-9	
Pyrene	18,551-5	
9-Anthracenecarbonitrile	15,276-5	
9-Nitroanthracene	N1020-9	
9,10-Diphenylanthracene	D20500-1	
2-Acetylphenanthrene	A1920-2	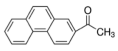
Phenathrene-9-carboxaldehyde	P1160-3	
9-Phenathrol	21,128-1	
Perinaphthenone	P1080-1	
7-Methylbenzo [a] pyrene	38,090-3	

Compound	Sigma-Aldrich	Structure
Fluoranthene	42,394-7	
Acenaphthene	21,537-6	
1-Acenaphthenol	A40-6	
2-Acetylfluorene	A1620-3	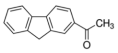
Dibenzothiophene	34,783-3	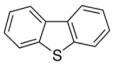
Carbazole	C310-3	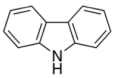
Dibenzothiophene sulfone	D3240-7	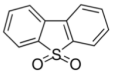
Phenoxathiin	21882-0	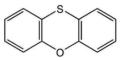
Phenoxazine	P1485-8	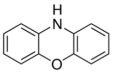
9(10 H)-Acridone	15021-5	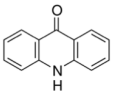

Table 7: PAHs selected for testing, with molecular structure diagrams and Sigma-Aldrich catalogue numbers

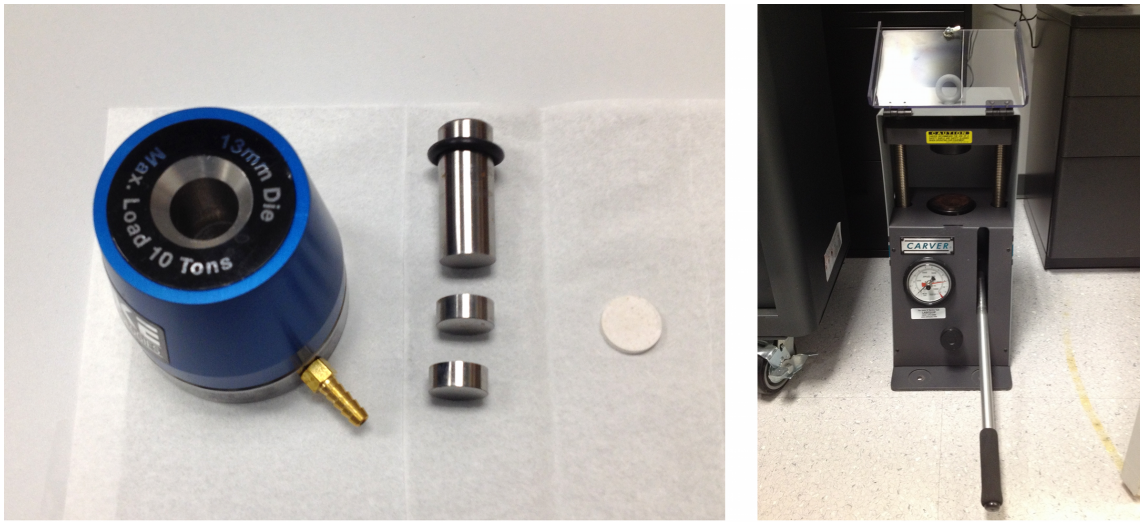

Figure 35: Pellet die (left) and press (right). A sample gypsum pellet is shown.

detector gate width of 1.5 ns, with fluorescence decay measured over a period of 20 ns with a 0.1 ns measurement resolution. In order to correct for the varying detector response as a function of the digital gate delay, an instrument response function was applied to the time-resolved spectra, measured using the constant output of a 200 mW, 465 nm blue LED. Lifetime values from the fluorescence decay profile were determined using a partial-least squares regression model incorporating the shape of the laser pulse and detector gate. A detailed overview of the time-resolved measurement methodology is presented in Chapter 4.

5.3 Time-resolved fluorescence of PAHs

In the subsequent analysis and discussion the 24 PAHs were divided into three groups; alternant (PAHs solely composed of six-membered rings), alternant with side groups, and non-alternant. Fluorescence is highly complex, dependent on many factors unique to each molecule that preclude making generalizations about relationships between numbers of rings, lifetimes, or other factors. For example, collision with atmospheric

O_2 can quench fluorescence, but the degree to which fluorescence is quenched is different for each PAH. Despite this complexity, the three groups of PAHs may be discussed broadly in the context of general rules applicable to some group members.

5.3.1 Alternant PAHs, side groups, and heterocycles

Figure 36 presents the time-resolved fluorescence spectra of six alternant PAHs, which consist solely of various numbers of six-membered carbon rings. Out of the 24 compounds, the alternant PAHs have the simplest structure and are the most frequently characterized in the literature. As alternant PAHs contain no substitutions and have no side groups, fluorescence is due primarily to $\pi - \pi^*$ transitions. The amount of delocalization increases with increasing ring number, moving fluorescence to lower energies. Multiple peaks in the spectra are likely the resolved vibrational structures of the ground and first excited states. As molecular stability increases with delocalization, geologically preserved kerogens or shales can be composed of hundreds to thousands of conjoined ring structures [93]. PAHs such as these are stable on the Martian surface on the scale of hours [23], long enough to be observed by a Raman or fluorescence instrument after being exposed by a drill or rock abrasion tool.

Figure 37 presents the time-resolved fluorescence of eight alternant PAHs, each containing a side group. Depending on the electron configuration, conjugation can extend onto side groups increasing the delocalization. Broader and faster fluorescence in PAHs containing side groups is indicative of more complex electronic configuration, and fewer pathways for radiative transitions back to the ground state. Figure 38 presents the time-resolved fluorescence of ten non-alternant PAHs and heterocycles. Substitutions in the six membered ring can cause significant reductions in fluorescence lifetimes. In these heterocycles, the lowest energy transition is not a $\pi - \pi^*$, but a $n - \pi^*$ due to the presence of unpaired electrons in the substituted atoms.

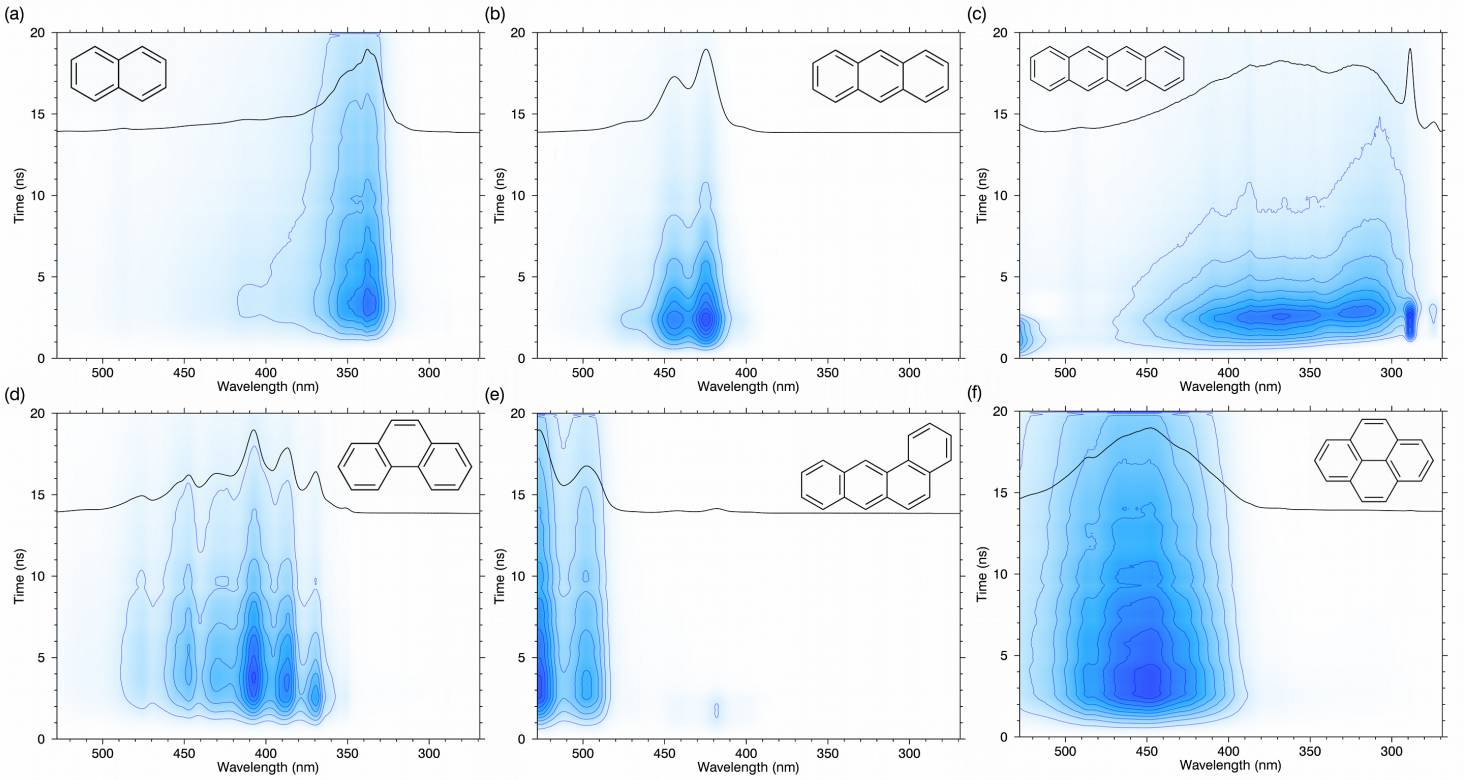

Figure 36: Time-resolved fluorescence over 20 ns of alternant PAHs (a) naphthalene, (b) anthracene, (c) 2,3-benzanthracene, (d) phenanthrene, (e) 1,2-benzanthracene, and (f) pyrene. A spectrum at the point of maximum intensity is overlaid at the top of each plot, and molecular structure diagrams are presented. The fluorescence intensity is represented by the color hue value of the contour plot.

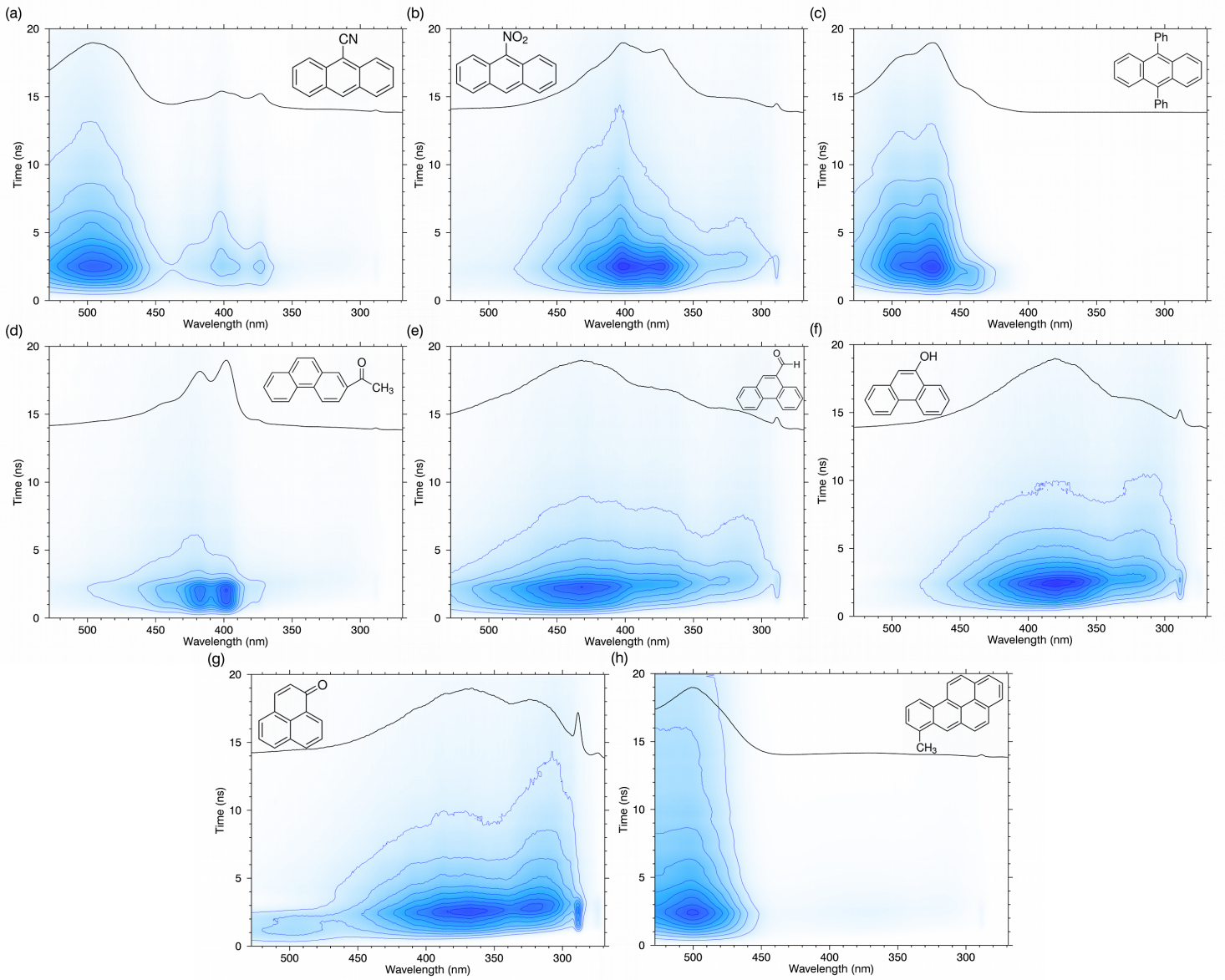

Figure 37: Time-resolved fluorescence over 20 ns of alternant PAHs with side groups (a) 9-anthracenecarbonitrile, (b) 9-nitroanthracene, (c) 9,10-diphenylanthracene, (d) 2-acetylphenanthrene, (e) phenathrene-9-carboxaldehyde, (f) 9-phenathrol, (g) perinaphthenone, and (h) 7-methylbenzo [a] pyrene. A spectrum at the point of maximum intensity is overlaid at the top of each plot, and molecular structure diagrams are presented.

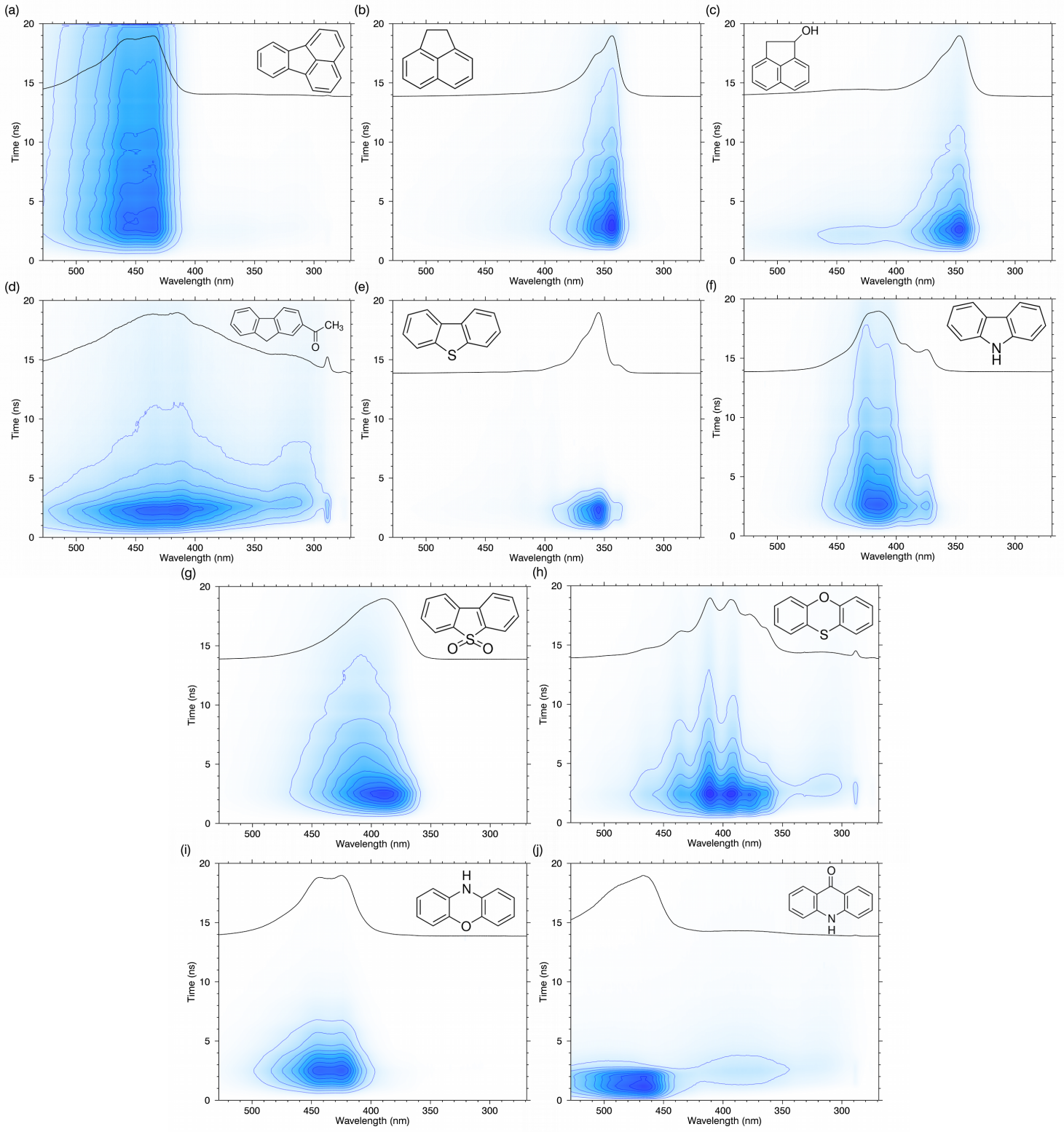

Figure 38: Time-resolved fluorescence over 20 ns of non-alternant PAHs and heterocycles.

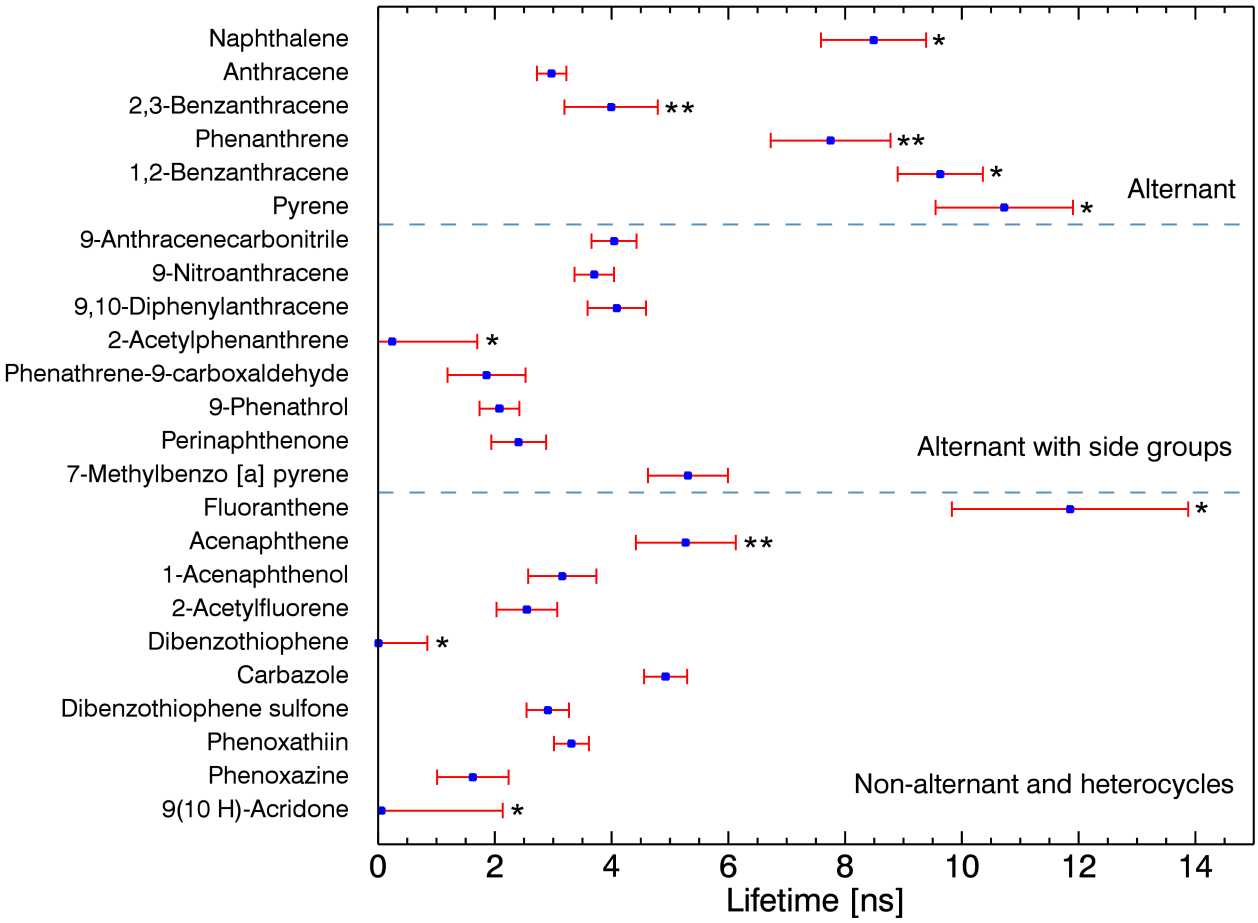

Figure 39: Calculated fluorescence lifetimes of PAH suite, with uncertainties presented as error bars in red. A (*) indicates a long or short lifetime not well fit by the model, and a (**) indicates a poor fit due to an apparent multiexponential decay.

5.3.2 Lifetime calculations

Figure 39 contains calculated lifetime values for each PAH. Lifetimes were calculated by fitting the decay curve to a partial least-squares regression model incorporating both the laser pulse and gate shape, following the method described in Chapter 4. The lifetime uncertainties are generally under 0.5 ns, determined using the methodology described in Chapter 2, although lifetimes that are very short (less than 1.5 ns), or very long are not as well fit by the model. Lifetimes shorter than the width of the laser pulse and gate width could not be precisely measured. Longer lifetimes could be measured with higher precision by using a different measurement and PLS model timescale, for example by measuring fluorescence decay over 100 ns instead of 20 ns. In some cases, the relatively large measurement error is due to the decay curve deviating from a single-exponential profile. Multi-exponential decays indicate either a contaminant in the sample, formation of a transient species when significant numbers of molecules are kept in an excited state, or multiple fluorophores within a sample [59].

5.3.3 PAH intensity and diversity per wavelength

The diversity of the PAHs selected for study may allow for some generalizations to be made regarding the behavior of 2-4 ring PAHs in general. It is clear from the measured spectra that PAHs of this variety fluoresce across a wide wavelength range. From an instrumental perspective, selecting a window of observation may require a trade-off if the window extent is limited by engineering constraints. In order to determine an optimal observation window, the 24 PAH spectra were normalized relative to the Raman C-H stretch of the cuvette, allowing the relative intensities to be compared. The PAH spectra were then added together, resulting in a combined spectrum

highlighting wavelengths that contained higher intensities of PAH fluorescence. The result is displayed in Figure 40 top. A vertical trace (blue) indicates the optimal center wavelength for an observation window with a width read off of the y-axis, and is located around 420 nm for any width. The optimal center wavelength was determined by calculating the window position that contained the highest levels of PAH fluorescence for each window width.

A similar calculation can be performed to locate an optimal observation window focusing not on regions with higher intensity, but on regions with the most diversity in fluorescence. Diversity of fluorescence was calculated by normalizing all spectra to the highest fluorescence point and taking the standard deviation of all 24 samples at each wavelength. This calculation was performed for all 24 PAHs, and for each of the three subgroups individually, presented in Figure 40 bottom. A vertical trace indicating the optimal gate position based on the variation of PAH fluorescence was found to also center around 420 nm.

While the amount of fluorescence and quantified diversity of fluorescence was found to be relatively low below 350 nm, a combined Raman and fluorescence instrument would likely utilize this spectral region if engineering constraints are strict, as this wavelength range is connected to the Raman window and can be imaged using the Raman grating without re-alignment. While this region may not be optimal for all PAH fluorescence, it is preferred for other important astrobiological targets, such as aromatic amino acids (see Chapter 4). However, it is not obvious if such a window would allow strong detection of larger PAHs or complex geologically preserved organics, which may fluoresce with broad signatures centered around higher wavelengths.

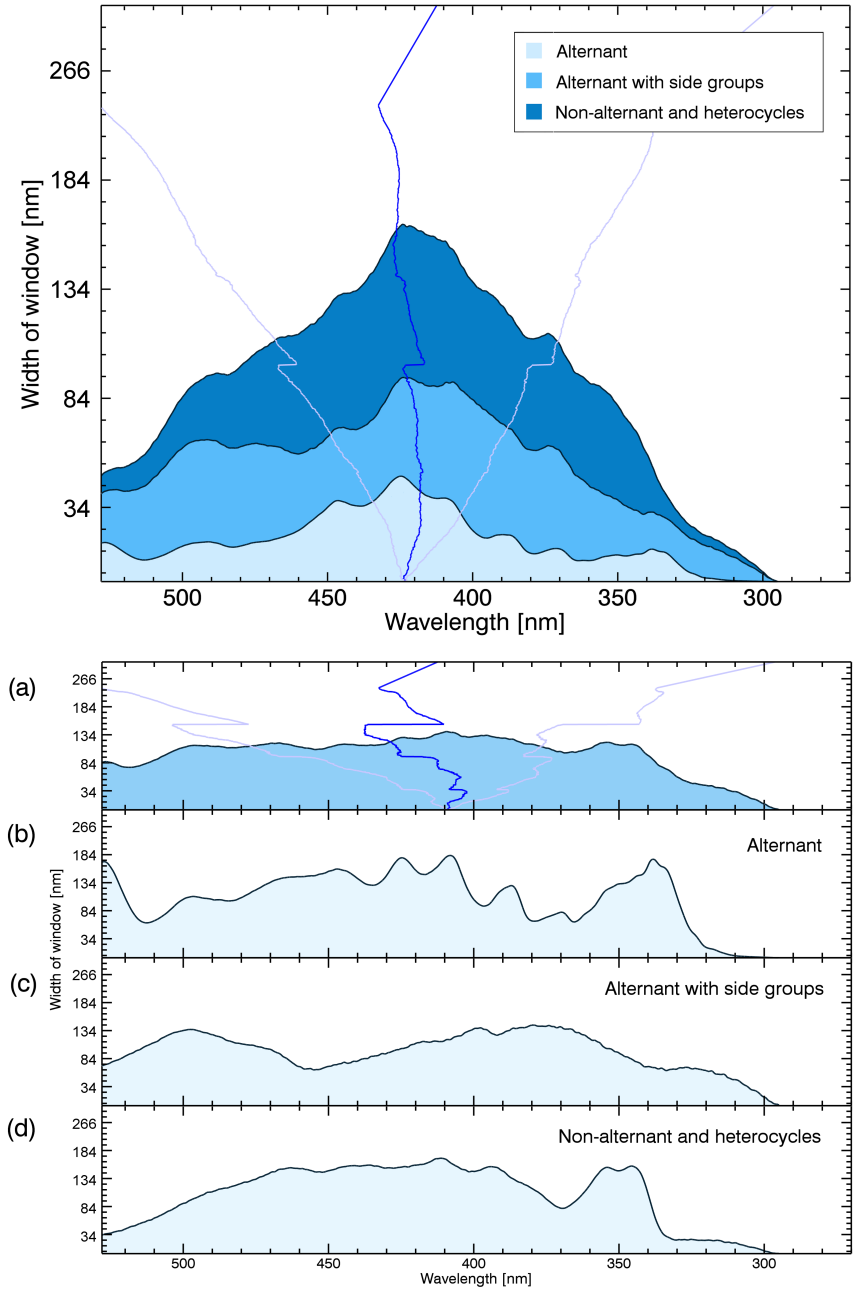

Figure 40: Top: A flight instrument may have a restricted fluorescence observation window due to engineering constraints. The top figure presents a summation of all PAH fluorescence, with a blue vertical trace indicating the optimal location for the center of an observation window with a width read from the y-axis. The optimal center wavelength regardless of the size of the observation window is centered around 420 nm. Bottom: Similar vertical traces are applied to a plot of spectral regions containing high levels of diversity in the PAH suite, where diversity is defined as the standard deviation of PAH spectral intensities at each wavelength.

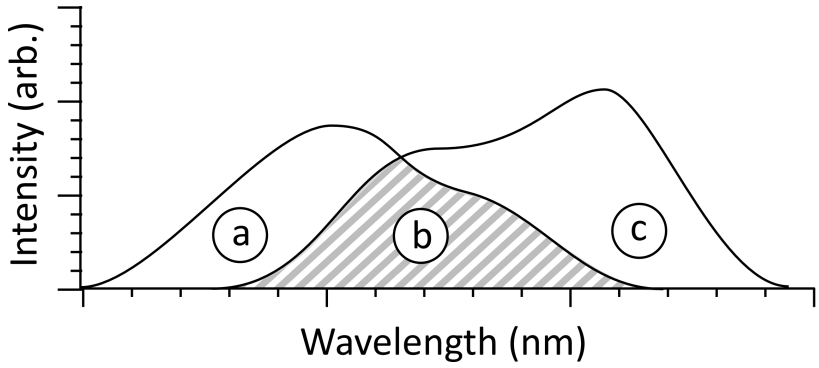

Figure 41: Visual representation of the spectral difference integral defined in Equation 32, calculated by integrating over the non-overlapping areas (a) and (c) of two normalized spectra.

5.4 Improved discrimination of PAHs by incorporating time-domain measurements

From Figures 36 and 37, and 40 it is evident that the 2-4 ring PAHs exhibit diverse fluorescence lifetimes. The lifetime may therefore be used in addition to the spectrum to discriminate between compounds. Compounds such as dibenzothiophene and acenaphthene have similar fluorescence spectra, but have lifetimes that differ by several nanoseconds. Therefore by incorporating time-domain information into the analysis of PAH spectra, the samples may be better distinguished.

In order to quantify the differences between single spectra and time-resolved datasets, which are composed of sets of 200 individual spectra, a normalized spectral difference integral was calculated for both sets of data between each of the 24 PAHs. A representation of the difference integral is shown in Figure 41. For single spectra, the area of each PAH spectrum was normalized and a difference integral was calculated using Equation 32.

$$\Delta_S(\boldsymbol{\alpha}, \boldsymbol{\beta}) = \int_{i=0}^{N} \left| \frac{\alpha_i}{\|\boldsymbol{\alpha}\|_1} - \frac{\beta_i}{\|\boldsymbol{\beta}\|_1} \right| d\tilde{v} \tag{32}$$

where Δ_S is a value quantifying the differences between two spectra, $\boldsymbol{\alpha}$ and $\boldsymbol{\beta}$. The spectra are individually normalized using the L1 norm, and the integration occurs over the extent of the measured window, N. For time-resolved datasets, the volume of the decay curve for each PAH was normalized and difference integrals were calculated between each PAH following Equation 33.

$$\Delta_T(\boldsymbol{\alpha}, \boldsymbol{\beta}) = \int_{i=0}^{N} \int_{j=0}^{M} \left| \frac{\alpha_{i,j}}{\|\boldsymbol{\alpha}\|_{2\mathrm{D}}} - \frac{\beta_{i,j}}{\|\boldsymbol{\beta}\|_{2\mathrm{D}}} \right| dt\, d\tilde{\nu} \tag{33}$$

where Δ_T is a value describing the differences between two time-resolved datasets, $\boldsymbol{\alpha}$ and $\boldsymbol{\beta}$. The integration extends over the spectral window N, and the time window M. Terms in the denominator represent a 2D analogue to the L1 norm, a summation of the absolute value of all elements, ensuring that the two datasets are similarly normalized. These two difference integrals are comparable, as a single fluorescence spectrum obtained with a 20 ns gate width can be considered to be equivalent to the sum of all 200 spectra with a 0.1 ns gate step over the same 20 ns in the corresponding time-resolved dataset. In both cases, the detector accumulates the same quantity of photons over the same time period. In other words, if the fluorescence signal volume is contained in a 20 ns time window, that signal can either be measured all at once (in a single-spectrum measurement with a 20 ns gate width), or in slices (a time-resolved measurement) but the overall signal in each case is similar and therefore the sum of all the time-resolved spectra can be normalized to the sum of the single-spectrum measurement.

Equation 32 was applied to each pairing of PAHs, quantifying how unique each individual spectrum is compared to the other members of the sample set. Figure 42 presents a matrix quantifying the difference integral between each PAH using the single-spectrum Δ_S values. Color values of blue correspond to spectra that are more

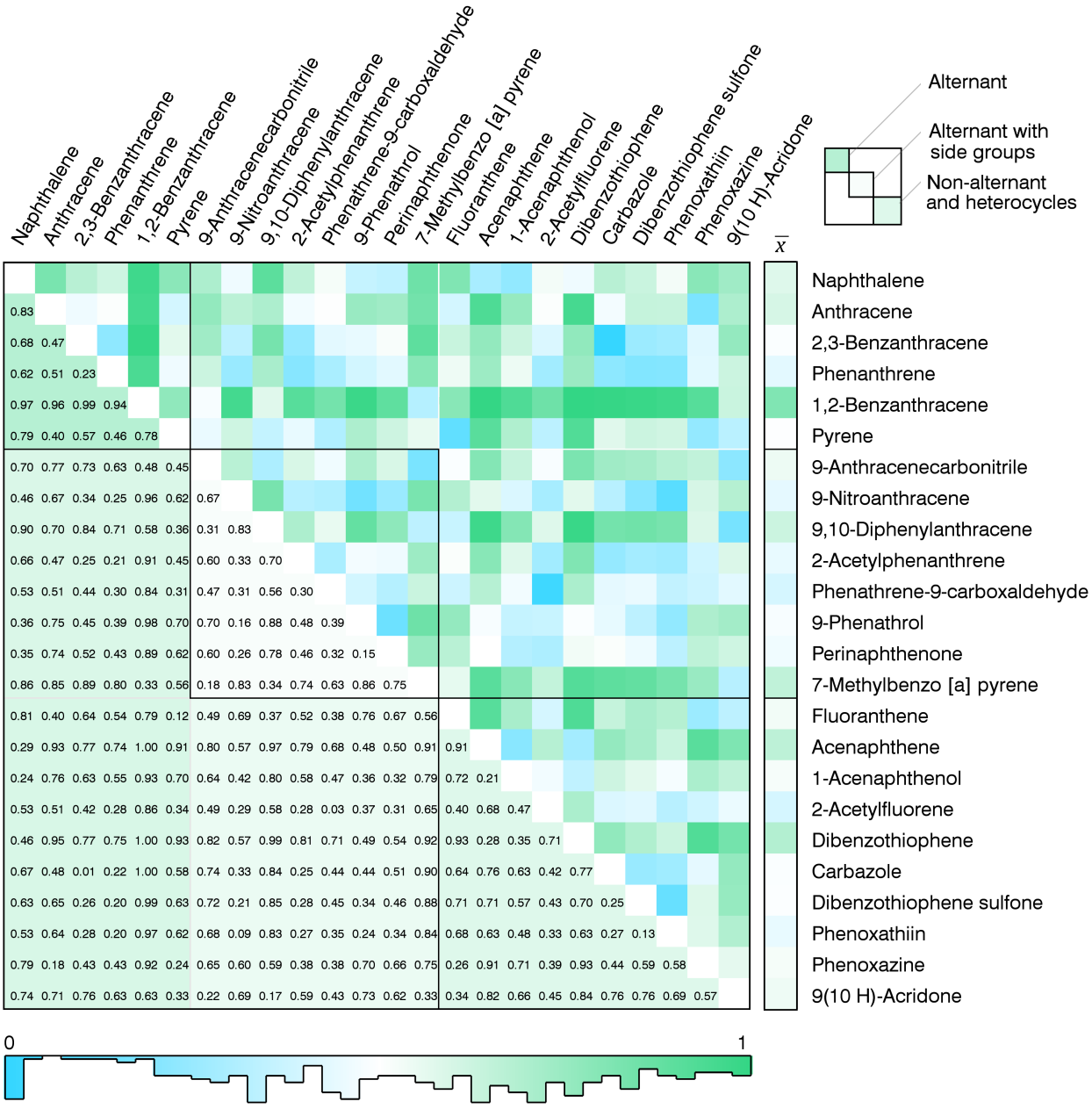

Figure 42: A matrix containing the normalized spectral difference integral between each of the 24 PAH samples. Blue colors indicate spectra that are more similar, and green colors represent spectra that are less similar (and have a larger difference integral). The matrix is divided along the diagonal into alternant PAHs, alternant PAHs with side groups, and non-alternant PAHs and heterocycles. Average values for the overlap integral for each PAH compared to all others are presented in the vertical color column labeled $\bar{x}$. The lower-left half of the matrix contains the normalized numerical value of the spectral difference. The color bar at the base of the matrix contains a histogram indicating the distribution of difference values.

similar, while values of green indicate spectra that are more differentiated and have larger difference integrals. Figure 43 presents a similar matrix, but higher color values correspond to samples where the difference integral is increased when time-domain information is accounted for, represented as a percentage increase between the time-resolved and single-spectrum values. The color value was determined by taking the percent difference between the time-resolved and single-spectra difference integrals, following Equation 34. In this case, redder colors correspond to spectral pairs that were more differentiated when time-domain information was included. The calculated increase in differentiability was clamped at 100%, due to a few strong outliers resulting from comparisons between short and long lifetime compounds.

$$\Delta_D(\boldsymbol{\alpha}, \boldsymbol{\beta}) = 100 \times \frac{\Delta_T(\boldsymbol{\alpha}, \boldsymbol{\beta}) - \Delta_S(\boldsymbol{\alpha}, \boldsymbol{\beta})}{\Delta_S(\boldsymbol{\alpha}, \boldsymbol{\beta})} \tag{34}$$

A summary of these results is presented in Figure 44. Three histograms are presented, each containing results from the application of Equations 32-34. PAHs compared using time-resolved measurements were able to be better differentiated than when compared using single-spectra measurements. This is seen by a higher average differentiability in Figure 44 (b) compared to Figure 44 (a). Histogram (c) in Figure 44 is weighed towards the lower end of the histogram range. This indicates that the increase in useful information provided by time-domain measurements is not restricted to one or two outliers, but instead the differentiability between a larger number of PAHs was moderately improved. The top 25% of compounds that had calculated lifetime most distinct from the average are seen in the long tail of Figure 44 (c), where their distinct lifetimes resulted in a significant increase in differentiability when time-domain information was accounted for. Examples of these compounds are fluoranthene, pyrene, and 9(10 H)-acridone, which have higher or lower lifetimes

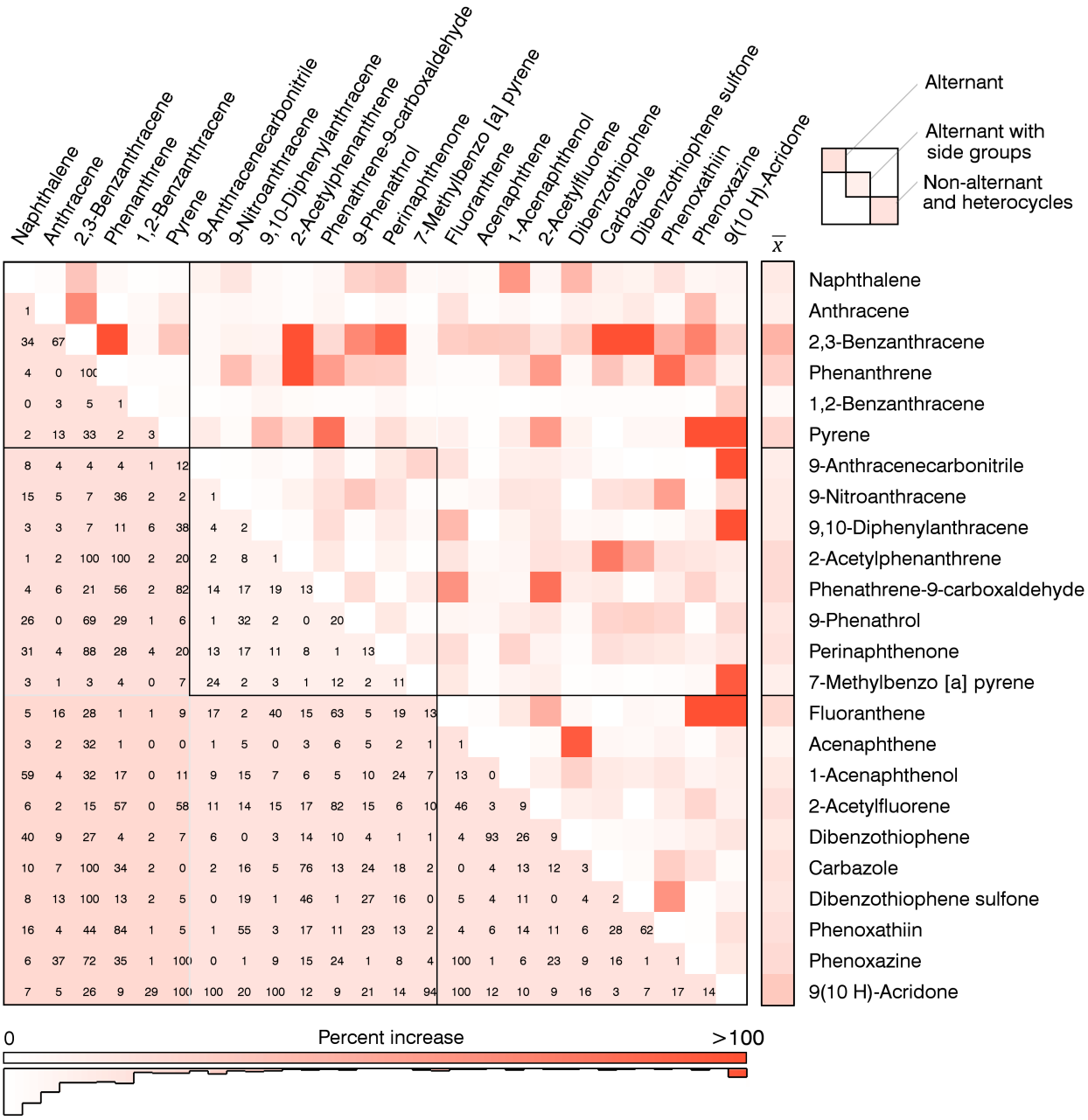

Figure 43: A matrix containing the percent increase in differentiability between the single-spectrum and time-resolved datasets for each of the 24 PAH samples. Redder colors represent spectra that are better differentiated with the addition of time-domain information. Values greater than 100% (pairings of very short and long lifetimes) were clamped to 100%. The color bar at the base of the matrix contains a histogram indicating the distribution of overlap values.

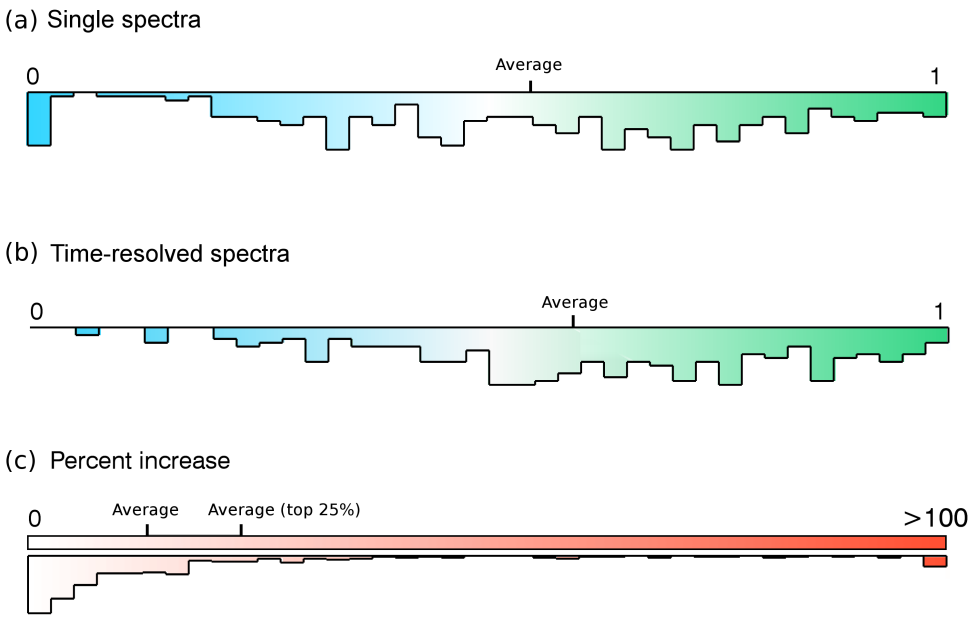

Figure 44: Histograms showing the spread in differentiability between the PAH samples for the single spectra (top) and time-resolved (middle) datasets. The bottom histogram presents the percentage increase for each PAH between the two datasets. In all cases, higher values represent more differentiability between spectra. The average of each histogram is noted, and the bottom histogram additionally marks the average increase in differentiability for the 25% of PAH samples that had lifetimes most divergent from the average.

(lifetimes most divergent from the average). Dibenzothiophene and acenaphthene, similar spectrally, are more easily discriminated when time-resolved measurements are obtained. Conversely, compounds that are different spectrally but have similar lifetimes, such as anthracene and 1-acenaphthenol, do not increase differentiability when time-domain information is measured, as expected. Overall, the average increase in discrimination was found to be 12% for all PAHs, and 20% for the 25% of compounds with lifetimes most divergent from the average.

5.5 Geolocation of organics using time-resolved fluorescence

An ultraviolet Raman measurement with an average power of around 2 mW on an unprepared surface could take several minutes or longer, up to tens of minutes, to obtain sufficient signal to conclusively identify the C=C, C-H, and C=O bonds indicative of organic material. As the spot size of a flight instrument may be on the order of tens of microns, and any organic material may be in similarly sized concentrations, it is imperative to only obtain Raman spectra of spots that offer the greatest chance of organic detection.

As individual fluorescence spectra may be obtained in a matter of seconds, it has been proposed to obtain fluorescence maps, consisting of a few hundred spectra, and use the features in the fluorescence map as a guide when obtaining lengthier Raman acquisitions [10]. A case study of this concept is described below, demonstrating how time-resolved measurements can assist in locating fluorescence features of probable organic origin, increasing the likelihood of organic detection.

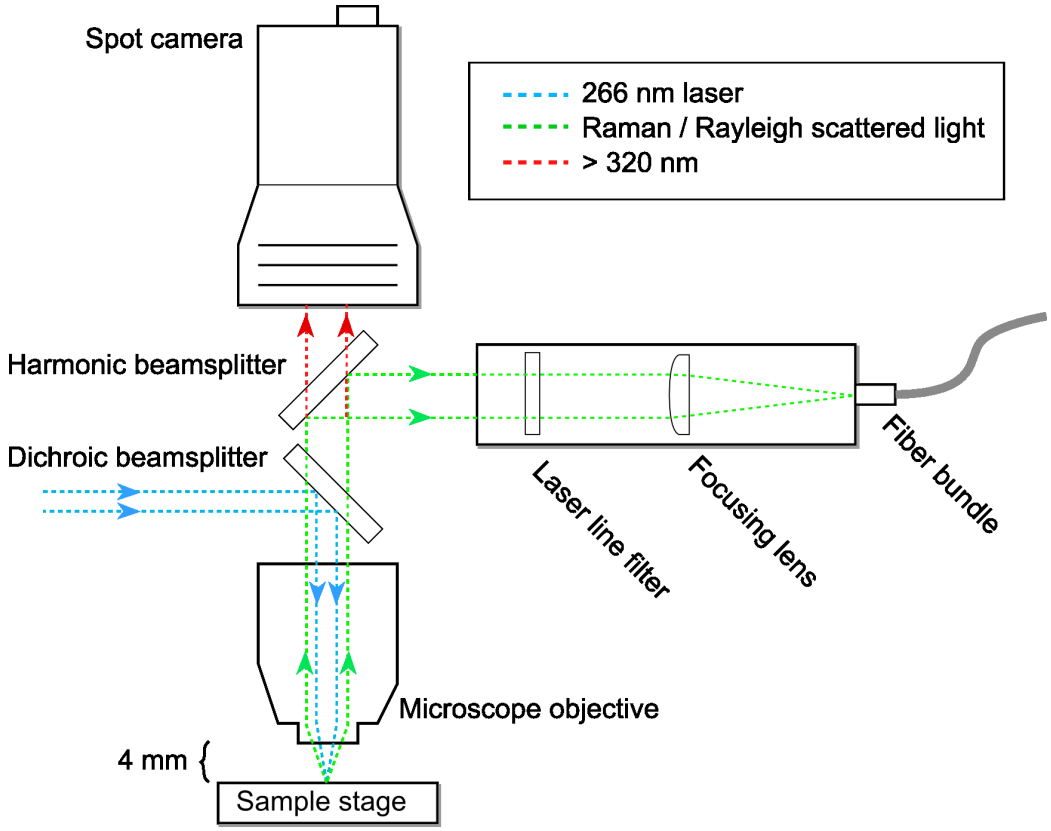

Figure 45: Microscope optical schematic.

5.5.1 Microscopic mapping

As the ultraviolet system used for this study is in a breadboard configuration, microscopic optics may be added to the laser path. To convert the system to operate on microscopic scales, an ultraviolet microscope objective was incorporated, coupled with a dichroic beamsplitter to direct the laser to the sample and a harmonic beamsplitter to direct the Raman scattered light to the spectrometer. This permits spot sizes on the sample of a few tens of microns, closely matching the spot sizes of most commercial systems. The motorized sample stage used for the traditional configuration of the instrument is sensitive enough to permit micron-scale movements, and therefore Raman mapping may be performed on this system at a microscopic scale.

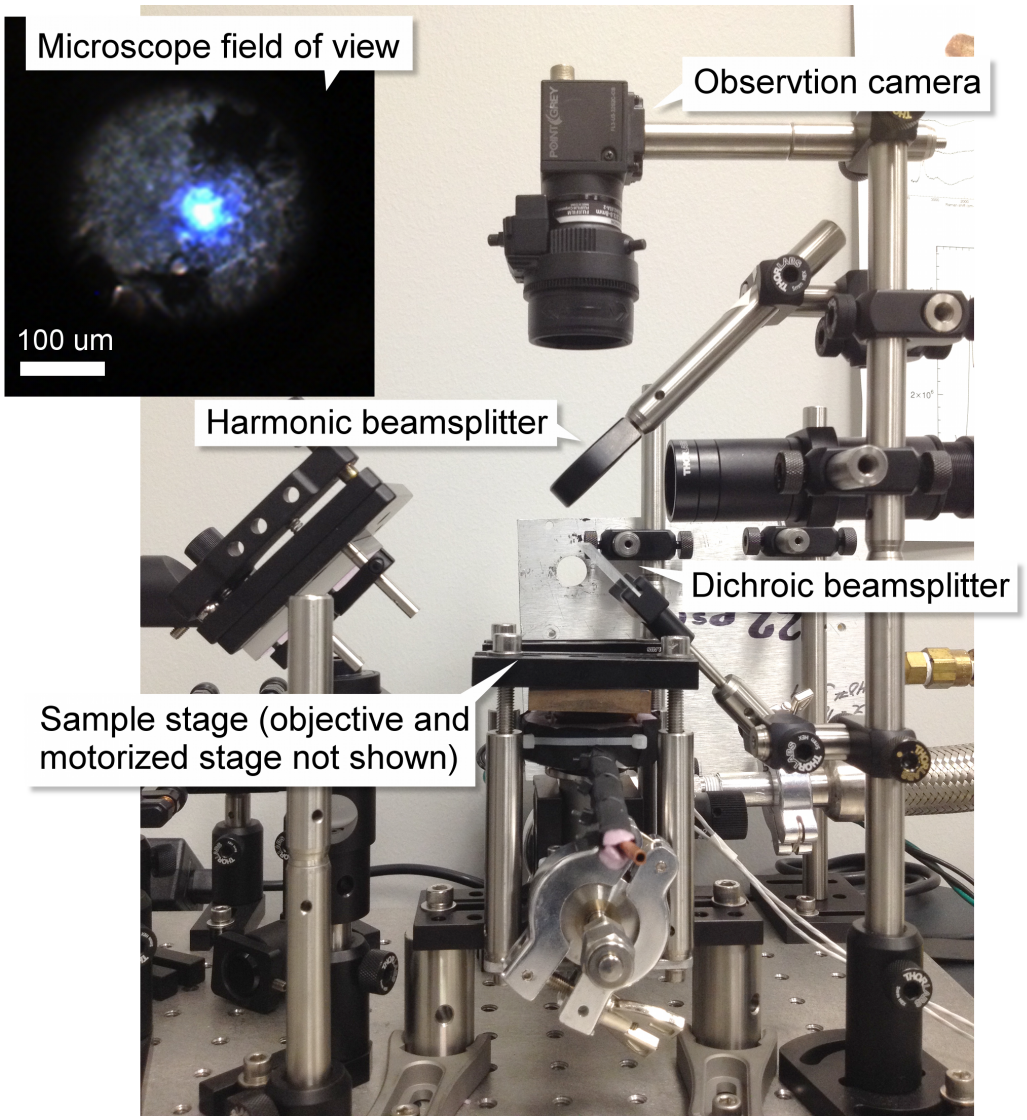

Figure 46: Microscope picture with a view of the laser through the objective (top). The microscope objective is not shown.

5.5.2 Locating regions of interest across complex surfaces

Fluorescence mapping was performed across a Mars analogue stromatolite sample containing geologically preserved carbon in the form of kerogen. The primary mineral constituents of the sample had been previously characterized as primarily carbonate and quartz. Mapping was performed in 50 μm step sizes across a 1 mm x 1 mm surface. A principal component analysis was performed on the 400 spectra dataset. The first three principal components, representing 94% of the variation in the data, are presented in Figure 47 (a, b, c). These three components correspond to the three physical fluorescence features observed in the data, and the distribution of each component across the sample surface is presented in Figure 47 (d, e, f). Each component is negatively correlated, further indicating that the fluorescence features originate from separate constituents of the sample.

Three time-resolved measurements were obtained at three locations on the sample, denoted by a red box on the figure, each location containing a maximum contribution of one of the principal components. The three time-resolved measurements are shown in Figure 47 (g, h, i). The lifetimes of the three fluorescence components can then be compared, and point (a) identified as the location on the sample most likely to contain organic carbon based on the presence of short-lived fluorescence. In this case, the components of the sample (kerogen, carbonate, and quartz) are known and the observed components can be compared against standards of the same compounds, shown in Figure 48. With this additional information, the selection of feature (a) for subsequent Raman investigation is further justified.

Without time-resolved measurements the highest priority location for Raman investigation would be determined only from Figure 47 (a,b,c). The choice would not be as clear, as each of the three features is similarly broad, differing only in peak

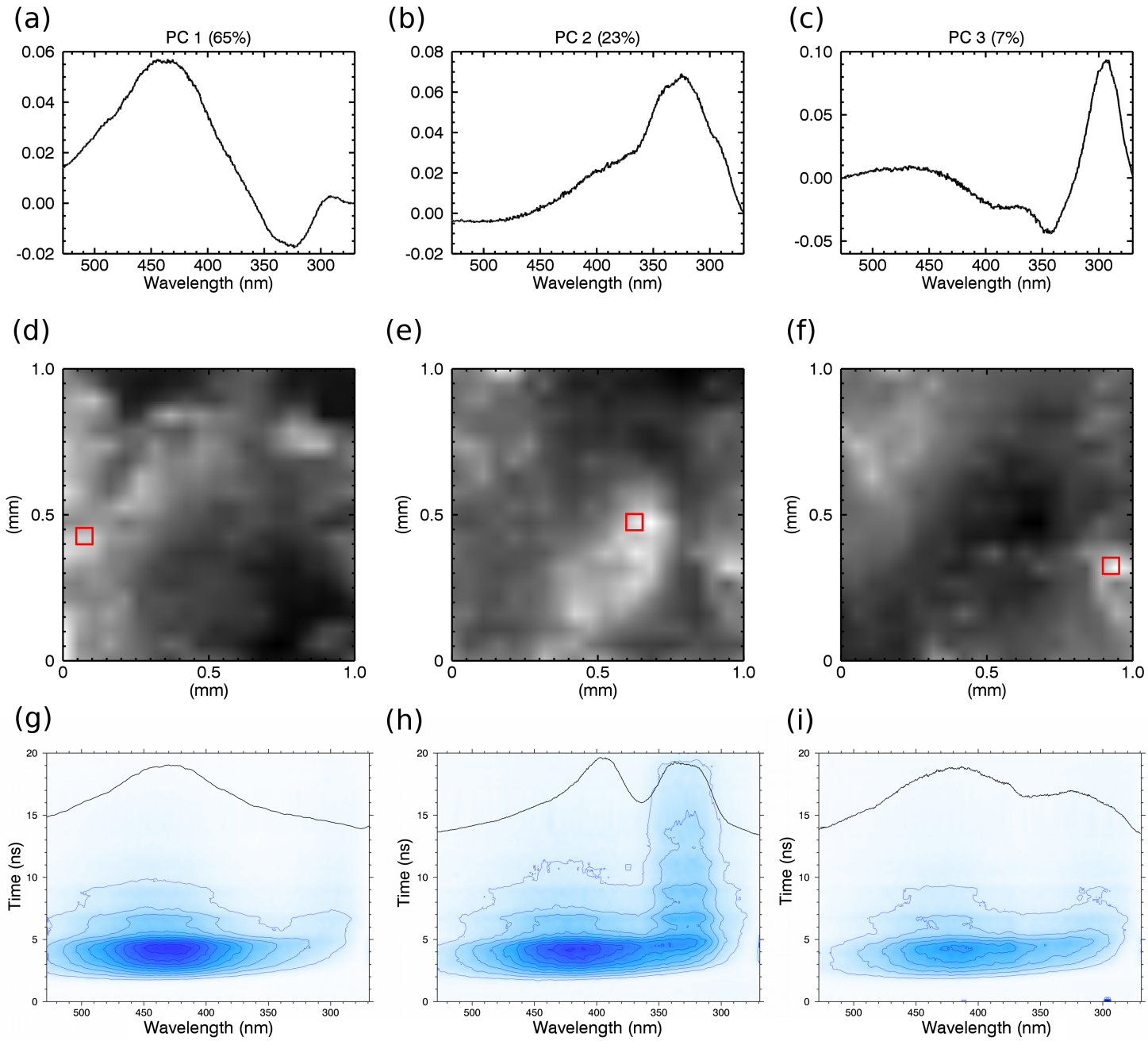

Figure 47: (a, b, c) The first three principal components of the fluorescence map dataset are presented in the top row. (d, e, f) The distribution of the three PCs across one square millimeter of the stromatolite surface are shown in the middle row. (g, h, i) Time-resolved fluorescence spectra obtained over 20 ns are presented in the bottom row, obtained at locations indicated by a red box on the middle row fluorescence maps. Single-spectra are overlaid in black on the time-resolved plots.

wavelength, which is not in itself a particular indicator of organic material. With time-resolved information, the long-lived components can be identified as probable mineral fluorescence.

Without the ability to gate and measure fluorescence on short timescales, organic and mineral fluorescence will be convolved. If a Raman instrument on a Mars rover must be judicious in the number of spectra obtained, it is important to select the positions that best offer the chance of organic detection. Figure 49 presents a comparison between ungated measurements (Figure 49 left), simulated using a 1 μs gate, and short-gated measurements (Figure 49 right). Figure 49 (a, b, c) correspond to the locations presented in Figure 47. Several fluorescence features that appear interesting in the long-gate acquisition are not present in the short-gate spectra, and are noted with a blue asterisk. The absence of these features in the short-gate spectra indicate that the fluorescence is long-lived, and therefore likely due to minerals or rare-earth impurities. However, features indicated with a red asterisk are persistent in both short- and long-gate spectra, and are likely due to organic material in the sample. A system without time-resolved capabilities would only be able to rely on the long-gated measurements, while a time-resolved system could deconvolve the short-lived signal from the total fluorescence emission.

5.6 Summary

The fluorescence spectra and time-resolved decay profiles of 24 2-5 ring PAHs have been presented. The PAHs display diversity in both the fluorescence spectra and decay lifetimes, calculated using a PLS model incorporating the shape of the laser pulse and detector gate. Calculated lifetimes were most accurate for single-exponential profiles with lifetimes in the 2-8 ns range. If performed on the Martian surface, time-

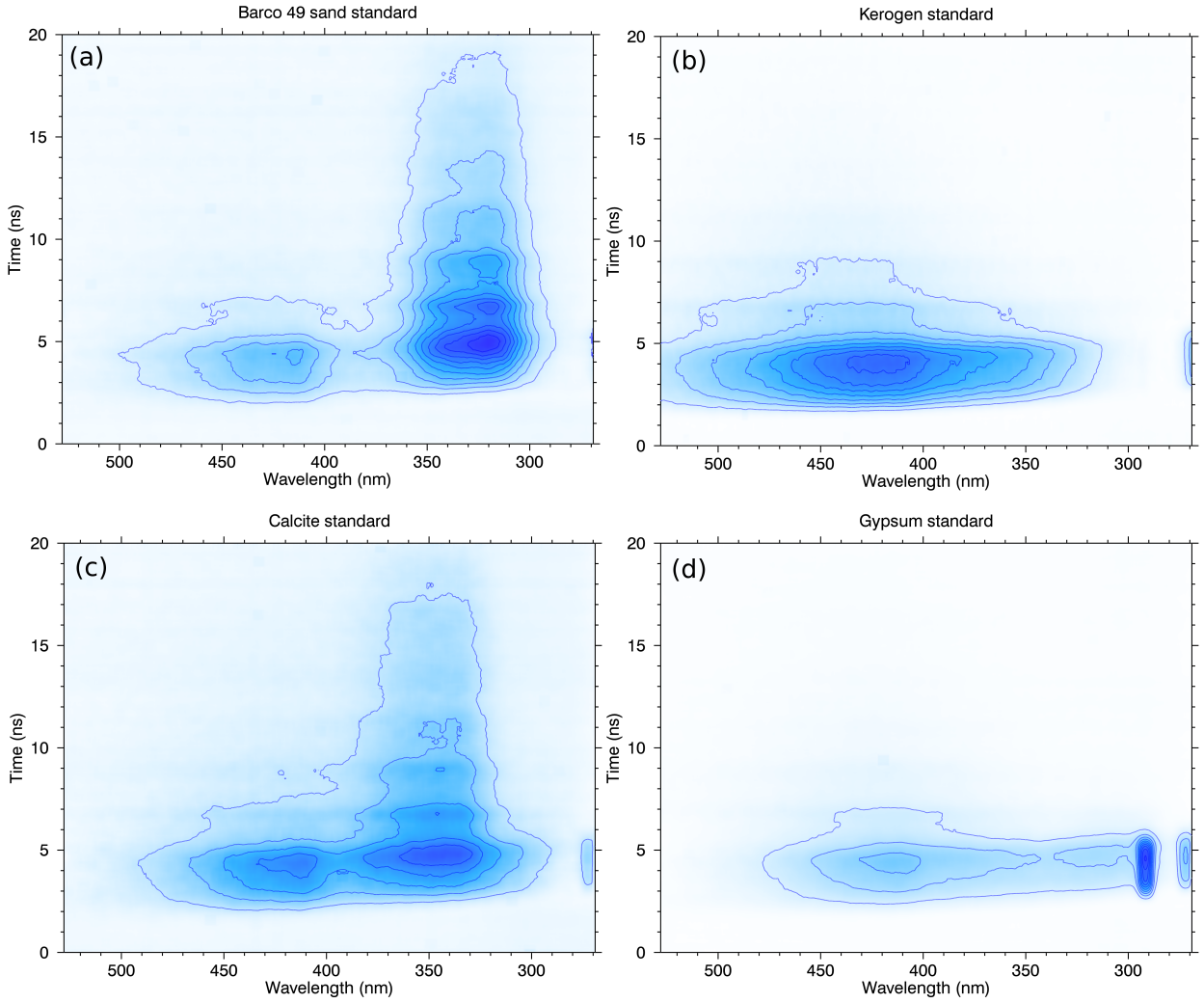

Figure 48: Time-resolved fluorescence profiles of (a) silica sand, (b) kerogen, (c) calcite, and (d) gypsum

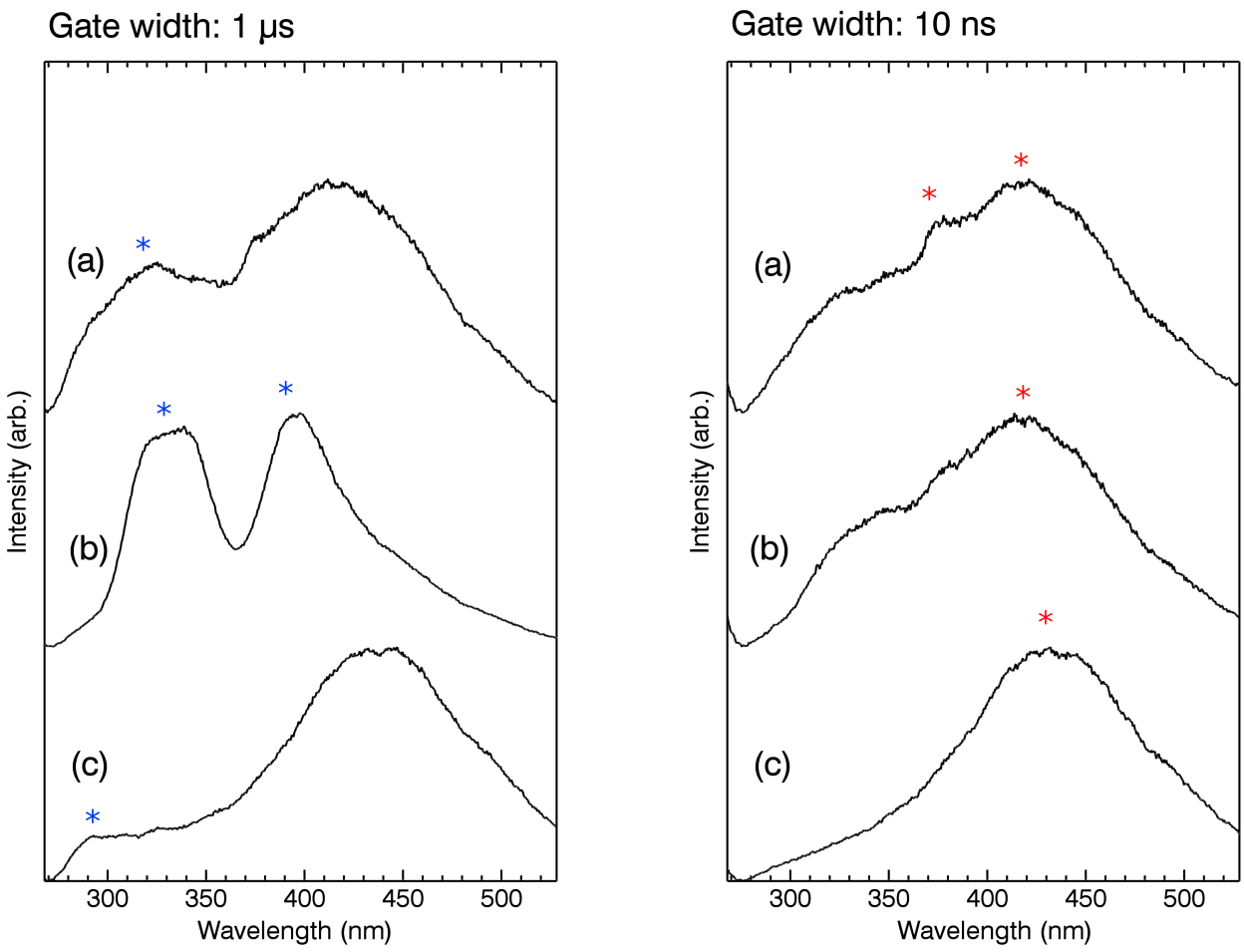

Figure 49: Fluorescence spectra of the points (a, b, c) sampled in Figure 47. Both long-gate (left) and short gate (right) measurements are presented. Blue asterisks denote features with long lifetimes (mineral), while red asterisks denote short-lived (organic) features.

resolved measurements may help detect and discriminate organic material, and may play a valuable role in algorithmically locating regions of interest for subsequent Raman measurements searching for C=C, C-H, and C=O bonds indicative of organic material. Time-resolved measurements can help identify short-lived organic fluorescence features which would otherwise be ambiguous. With the limited measurement opportunities and timeframes inherent on a rover platform, time-resolved capabilities can assist in identifying the locations on a sample most likely to contain organic material, increasing the chances for detecting organic carbon.

6 Conclusions

A 266 nm Raman spectrometer incorporating time-resolved fluorescence capabilities was developed at York University in order to investigate the performance of an ultraviolet Raman system in detecting organic material on Mars. The instrument was designed to match the specifications of a putative stand-off flight instrument, primarily considering the laser, detector capabilities, and optical concept. A breadboard construction allowed the instrument to be easily modified between Raman and fluorescence modes, as well as between macro (mm) and micro (μm) scale 2D mapping. Software and analysis methods developed for this work allowed large spectral datasets to be autonomously collected and algorithmically analyzed, in a workflow similar to an unsupervised instrument on the Martian surface. The instrument was carefully characterized, measuring the laser properties at the sample, selecting detector parameters, and calculating limits of detection to baseline performance.

In order to determine if 266 nm is a useful excitation for organic detection, a tiered approach was applied to a wide range of pure organic compounds, simple organic-mineral mixtures, and finally complex rock samples from extreme environments on Earth. A wide range of mineral and organic samples were found to present characteristic Raman spectra at 266 nm, detectable at low (sub 1%) concentrations. Generally, the Raman window from 266 nm to 296 nm was found to be free of fluorescence. In cases where organics or the mineral matrix displayed fluorescence, it was limited to wavenumbers greater than 2000 cm^{-1}, and did not overlap with the organic fingerprint region between 1100 and 1650 cm^{-1}. This result contrasts with the findings of some authors, who had previously suggested that the acceptable cutoff for laser wavelength was 250 nm, and that any excitation above that limit would suffer from fluorescence interference. We find that in fact 266 nm is virtually fluorescence free in the region

where organic bands are present, and the potential to obtain fast (on the order of 1 ns) pulses from frequency quadrupled 1064 nm lasers, which have significant flight heritage, makes 266 nm a promising choice for a flight instrument.

In some cases, while fluorescence did not interfere with the Raman signal, the signal could be impacted if the sample was absorbent in the ultraviolet. This impact was strong enough to result in no observed Raman scattering in samples where the absorption coefficient was sufficiently high. A variety of physical causes may explain this observation, including absorption of both the incoming and outgoing radiation, re-absorption of any Raman scattered light, and non-radiative de-excitation pathways in complex samples. The dust on Mars, which is ubiquitous across the surface, contains absorbent compounds such as iron oxides and glasses, and future work should investigate the effect of a thin dust coating on a signal obtained by a stand-off ultraviolet instrument. Closer to the rover, this issue could be resolved by a rock abrasion tool that can remove dust from a sampling area.

While absorption can be a drawback to ultraviolet excitation, a primary outcome of this work is that absorption by organics can be more than overcome by incorporating fluorescence capabilities into the instrument. When the Raman signal of an organic compound is reduced due to absorption, the subsequent reemission of the absorbed light in the form of fluorescence can be several magnitudes stronger than traditional Raman scattering. This potential benefit was investigated by selecting a wide range of organic compounds, including PAHs that displayed poor Raman scattering at 266 nm. Fluorescence experiments also followed a tiered approach, and involved looking at pure compounds, simple mixtures, and complex rock samples. It was found that classes of organic compounds containing six-carbon rings (including aromatic compounds) displayed poor Raman spectra compared to other wavelengths but that they typically displayed strong and characteristic fluorescence between 290

and 500 nm. The samples that exhibited this behavior included a suite of 24 PAHs, the most likely organic candidate on Mars.

As minerals can also fluoresce, any fluorescence spectra observed on Mars may contain a complex mixture of mineral and organic compounds. With no ability to separate the two, the inherent complexity of interpreting fluorescence compared to Raman spectra may make any identification of organic fluorescence difficult or impossible. A major finding of this work was that a laser with a pulse width on the order of one nanosecond and a fast-gating detector is sufficient to measure fluorescence lifetimes with sub-ns precision. As organic and mineral fluorescence significantly differ in lifetime, time-resolved capabilities can help locate organic fluorescence when it would otherwise be convolved with fluorescence from a complex mineral matrix. This capability does not require any additional instrumentation other than the ability to observe the fluorescence window. Further, organic lifetimes differ, ranging from <1 ns to 20 ns, and therefore incorporating time-domain information allows individual organics to be better discriminated.

If Canada remains invested in the development of an ultraviolet Raman instrument for life detection, the outcome of this work should provide guidance into resolving trade-offs that will occur when reconciling science objectives with the engineering restrictions of a prototype or flight instrument. Incorporating fluorescence capabilities strongly increases the detection threshold and range of organic compounds that can be identified, critically increasing the detection of PAHs, the most likely Mars organic. Further, adding time-resolved capabilities allows organic fluorescence to be separated from mineral fluorescence. Although much work remains to be done in addressing some of the trade-offs of an ultraviolet excitation, a combined ultraviolet Raman and fluorescence instrument offers higher sensitivity to the highest priority Mars-relevant organics than a Raman instrument alone.

7 Future work

While a Raman instrument has not yet flown in space, the successor to the Curiosity rover in 2020 will have a 532 nm stand-off Raman system and a 248 nm micro Raman and fluorescence mapping instrument. There is a significant amount of work that can be done before that date that will improve understanding of the performance of Raman systems operating in a Martian environment.

A primary outcome of this work was to demonstrate the potential benefit of including time-resolved capabilities in a combined Raman and fluorescence instrument. These experiments provide a foundation for future work that should expand on the range of samples tested to represent better the possible fluorescence environment that may exist from Martian samples. While organic fluorescence was the focus of this work, understanding mineral fluorescence would be useful not only for the further development of time-resolved fluorescence capabilities, but for providing ground-truth measurements useful for interpreting the single-spectral measurements of SHERLOC that will return from Mars in a few years. The degree to which Martian environmental conditions affect fluorescence and fluorescence lifetimes is not well studied. Advances in algorithmic methods to determine how to identify interesting Raman locations on a sample would be valuable. One proposed mode of operation of SHERLOC is to use fluorescence mapping as a method to locate regions of interest for subsequent Raman measurements.

When considering the eventual engineering requirements of a flight instrument, the investigations performed in this work have shown that organic fluorescence can occur over a very large wavelength range, and an eventual window of observation may need to be limited in order to accommodate Raman capabilities or other considerations. While the data presented in Chapters 4 and 5 can provide a good basis

for selecting a fluorescence window intended to observe PAHs and aromatic amino acids, the fluorescence behavior of other classes of biomolecules were not thoroughly investigated. There is likely a trade-off between the size and position of the Raman and fluorescence observation windows that should be weighted based on the quality of data obtained from the highest priority groups of organic and mineral compounds, not all of which have been addressed in this work.

An ultraviolet excitation, like visible and near-IR wavelengths, performs well for some groups of compounds and poorly for others. While much of this work focused on sedimentary samples containing endoliths, Mars may have other types of structures, such as extinct hydrothermal systems, that could host organic compounds or signs of life. The Raman and fluorescence properties of sample types beyond sedimentary systems should be investigated to have a full understanding of the benefits of ultraviolet excitation.

While 266 nm performed well in this work in locating organic material in Mars analogue samples, the Raman signal of the bulk sample was found to be limited in cases where the sample contained an absorbing component, for example in cases where a thin coating of dust was present or if the sample contained iron oxides or organic compounds with aromatic rings. A rock abrasion tool would likely address this issue for cases where absorption was due to a surface contaminant by generating a fresh sampling face. In cases where stand-off measurement are required, a LIBS instrument could be used to remove dust contamination from the surface. The effect of surface dust should be investigated to determine under what conditions quality data can be obtained, and if this limitation is mitigated by other laser wavelengths.

A component of this project has been instrument development, increasing the breadboard capabilities over time. Iterations of the 266 nm instrument over the course of this degree have improved optics, added water cooling, added microscopic

imaging capabilities, and improved automation. There are several opportunities for improving the instrument, which could lead to more collaboration with other researchers and acquisition of data that can be better related to other systems. A few possible instrument improvements are the addition of a higher powered laser to increase the laser power from 1-2 mW to between 5-10 mW, redesigning the microscopic optics to reduce the beam size from abbout 20 μm to <5 μm, improvement of the quality of the observation window obtained by the ancillary camera, and adding a motorized grating and rotating beamsplitter wheel to easily switch between Raman and fluorescence modes.

Developing a method to work with thin sections, 30 μm thick samples slices adhered to microscope slides, would be a significant advancement. Thin sections can be analyzed using transmitted light, yielding mineralogical information not possible with bulk rock samples. Currently, the glass foundation and epoxy glue common in thin sections, used to bind the sample to the slide, both prohibit analysis with ultraviolet Raman systems. Thin sections can be prepared on quartz slides, addressing the fluorescence and absorption issues caused by glass, however no good replacement for epoxy has been found. The common epoxy used in thin sections not only fluoresces very intensely, but also exhibits Raman peaks due to the organic content that overlaps with the organic signature of interest in the rock. A combination of improved microscopic optics with thin-section capability would provide a significant improvement in sample classification and the performance characterization of ultraviolet wavelengths by allowing Raman measurements to be correlated with petrographic imaging and other techniques at the micron level.

References

[1] R. S. Afzal. Review of solid-state lasers for space applications. In *Proceedings of SPIE - The International Society for Optical Engineering*, volume 6100, 2006.

[2] J.R. Albani. Origin of tryptophan fluorescence lifetimes part 1. fluorescence lifetimes origin of tryptophan free in solution. *Journal of fluorescence*, 24(1):93–104, 2014.

[3] A.E. Aliaga, I. Osorio-Roman, C. Garrido, P. Leyton, J. Cárcamo, E. Clavijo, J.S. Gómez-Jeria, G. Díaz F., and M.M. Campos-Vallette. Surface enhanced Raman scattering study of l-lysine. *Vibrational Spectroscopy*, 50(1):131–135, 2009.

[4] D. T. Andersen, C. P. McKay, R. A. Wharton, and J. D. Rummel. Testing A Mars Science Outpost In The Antarctic Dry Valleys. *Adv. Space Res.*, 12(5), 1992.

[5] D. T. Andersen, W. H. Pollard, C. P. McKay, and J. Heldmann. Cold springs in permafrost on Earth and Mars. *Journal of Geophysical Research E: Planets*, 107, 2002.

[6] R. E. Arvidson, S. W. Ruff, R. V. Morris, D. W. Ming, L. S. Crumpler, A. S. Yen, S. W. Squyres, R. J. Sullivan, J. F. Bell III, N. A. Cabrol, B. C. Clark, W. H. Farrand, R. Gellert, R. Greenberger, J. A. Grant, E. A. Guinness, K. E. Herkenhoff, J. A. Hurowitz, J. R. Johnson, G. Klingelhofer, K. W. Lewis, R. Li, T. J. McCoy, J. Moersch, H. Y. McSween, S. L. Murchie, M. Schmid, C. Schroder, A. Wang, S. Wiseman, M. B. Madsen, W. Goetz, and S. M. McLennan. Spirit Mars Rover Mission to the Columbia Hills, Gusev Crater:

Misison overview and selected results from the Cumberland Ridge to Home Plate. *Journal of Geophysical Research*, 113, 2008.

[7] S.A. Asher and C.R. Johnson. Raman spectroscopy of a coal liquid shows that fluorescence interference is minimized with ultraviolet excitation. *Science*, 225(4659):311–313, 1984.

[8] N.A. Atamas, A.M. Yaremko, T. Seeger, A. Leipertz, A. Bienko, Z. Latajka, H. Ratajczak, and A.J. Barnes. A study of the Raman spectra of alkanes in the Fermi-resonance region. *Journal of Molecular Structure*, 708(1-3):189–195, 2004.

[9] L. Becker, D.P. Glavin, and J.L. Bada. Polycyclic aromatic hydrocarbons (pahs) in antarctic martian meteorites, carbonaceous chondrites and polar ice. volume 3111, pages 36–50, 1997.

[10] L.W. Beegle, R. Bhartia, L. DeFlores, M. White, S. Asher, A. Burton, S. Clegg, P.G. Conrad, K. Edgett, B. Ehlmann, F. Langenhorst, M. Fries, W. Hug, K. Nealson, J. Popp, P. Sobron, A. Steele, R. Wiens, and K. Williford. Sherloc: Scanning habitable environments with raman and luminescence for organics and chemicals, an investigation for 2020, 2015.

[11] R. Bhartia, W.F. Hug, E.C. Salas, R.D. Reid, K.K. Suapati, A. Tsapin, W. Abbey, K.H. Nealson, A.L. Lane, and P.G. Conrad. Classification of organic and biological materials with deep ultraviolet excitation. *Applied Spectroscopy*, 62(10):1070–1077, 2008.

[12] Jean-Pierre Bibring, Yves Langevin, John F. Mustard, François Poulet, Raymond Arvidson, Aline Gendrin, Brigitte Gondet, Nicolas Mangold, P. Pinet,

F. Forget, Michel Berthé, Jean-Pierre Bibring, Aline Gendrin, Cécile Gomez, Brigitte Gondet, Denis Jouglet, François Poulet, Alain Soufflot, Mathieu Vincendon, Michel Combes, Pierre Drossart, Thérèse Encrenaz, Thierry Fouchet, Riccardo Merchiorri, GianCarlo Belluci, Francesca Altieri, Vittorio Formisano, Fabricio Capaccioni, Pricilla Cerroni, Angioletta Coradini, Sergio Fonti, Oleg Korablev, Volodia Kottsov, Nikolai Ignatiev, Vassili Moroz, Dimitri Titov, Ludmilla Zasova, Damien Loiseau, Nicolas Mangold, Patrick Pinet, Sylvain Douté, Bernard Schmitt, Christophe Sotin, Ernst Hauber, Harald Hoffmann, Ralf Jaumann, Uwe Keller, Ray Arvidson, John F. Mustard, Tom Duxbury, François Forget, and G. Neukum. Global mineralogical and aqueous mars history derived from omega/mars express data. *Science*, 312(5772):400–404, 2006.

[13] Janice L. Bishop, Damien Loizeau, Nancy K. McKeown, Lee Saper, M. Darby Dyar, David J. Des Marais, Mario Parente, and Scott L. Murchie. What the ancient phyllosilicates at mawrth vallis can tell us about possible habitability on early mars. *Planetary and Space Science*, 86:130 – 149, 2013.

[14] J. Blacksberg, G.R. Rossman, and A. Gleckler. Time-resolved raman spectroscopy for in situ planetary mineralogy. *Applied Optics*, 49(26):4951–4962, 2010.

[15] L. E. Borg, D. J. Des Marais, D. W. Beaty, O. Aharonson, S. A. Benner, D. D. Bogard, J. C. Bridges, C. J. Budney, W. N. Calvin, B. C. Clark, J. L. Eigenbrode, M. M. Grady, J. W. Head, S. R. Hemming, N. W. Hinners, V. Hipkin, G. J. MacPherson, L. Marinangeli, S. M. McLennan, H. Y. McSween, J. E. Moersch, K. H. Nealson, L. M. Pratt, K. Righter, S. W. Ruff, C. K. Shearer, A. Steele, D. Y. Sumner, S. J. Symes, J. L. Vago, and F. Westall. Science priorities for Mars sample return. *Astrobiology*, 8(3):489–535, 2008.

[16] W. V. Boynton, D. S. Lauretta, E. Beshore, O. Barnouin, E. B. Bierhaus, R. Binzel, P. R. Christensen, M. Daly, J. Grindlay, V. Hamilton, A. R. Hildebrand, G. Mehall, D. Reuter, B. Rizk, A. Simon-Miller, and P. S. Smith. The OSIRIS-REx mission to RQ36: nature of the remote sensing observations. In *European Planetary Science Congress 2012*, page 875, September 2012.

[17] A.L. Brady, G. Druschel, L. Leoni, D.S.S. Lim, and G.F. Slater. Isotopic biosignatures in carbonate-rich, cyanobacteria-dominated microbial mats of the cariboo plateau, b.c. *Geobiology*, 11(5):437–456, 2013.

[18] V. Chevrier and P. E. Mathe. Mineralogy and evolution of the surface of mars: A review. *Planetary and Space Science*, 55(3):289–314, 2007.

[19] E. Cloutis, P. Szymanski, and D. Applin. Raman (532nm) spectroscopy of polycyclic aromatic hydrocarbons. *45th Lunar and Planetary Science Conference*, 1996, 2014.

[20] Charles S. Cockell, David C. Catling, Wanda L. Davis, Kelly Snook, Ray L. Kepner, Pascal Lee, and Christopher P. McKay. The ultraviolet environment of mars: Biological implications past, present, and future. *Icarus*, 146:343–359, 2000.

[21] L. Colangeli, V. Mennella, G. A. Baratta, E. Bussoletti, and G. Strazzula. Raman and infrared spectra of polycyclic aromatic hydrocarbon molecules of possible astrophysical interest. *Astrophysical Journal Letters*, 396(1):369–377, 1992.

[22] L.R. Dartnell and M.R. Patel. Degradation of microbial fluorescence biosignatures by solar ultraviolet radiation on mars. *International Journal of Astrobiology*, 13(2):112–123, 2014.

[23] L.R. Dartnell, M.R. Patel, M.C. Storrie-Lombardi, J.M. Ward, and J.-P. Muller. Experimental determination of photostability and fluorescence-based detection of pahs on the martian surface. *Meteoritics and Planetary Science*, 47(5):806–819, 2012.

[24] L.R. Dartnell, M.C. Storrie-Lombardi, and J.M. Ward. Complete fluorescent fingerprints of extremophilic and photosynthetic microbes. *International Journal of Astrobiology*, 9(4):245–257, 2010.

[25] E. Diaz, A. G. Moral, C. P. Canora, G. Ramos, O. Barcos, and J. A. R. Prieto. ExoMars raman laser spectrometer breadboard overview. *Proceedings of SPIE - The International Society for Optical Engineering*, 2011.

[26] H. Dong, J.A. Rech, H. Jiang, H. Sun, and B.J. Buck. Endolithnic cyanobacteria in soil gypsum: Occurences in Atacama (Chile), Mojave (United States), and Al-Jafr Basin (Jordan) Deserts. *Journal of Geophysical Research G: Biogeosciences*, 112(2), 2007.

[27] J.T. Edsall, J.W. Otvos, and A. Rich. Raman spectra of amino acids and related compounds. VII. Glycylglycine, cysteine, cystine and other amino acids. *Journal of the American Chemical Society*, 72(1):474–477, 1950.

[28] H. G. M. Edwards. Question 2: Raman spectroscopic approach to analytical astrobiology: The detection of key biomolecular markers in the search for life. *Origins of Life and Evolution of Biospheres*, 37(4-5):335–339, 2007.

[29] H. G. M. Edwards, B. Herschy, K. Page, T. Munshi, and I. J. Scowen. Raman spectra of biomarkers of relevance to analytical astrobiological exploration: Hopanoids, sterols and steranes. *Spectrochimica Acta - Part A: Molecular and Biomolecular Spectroscopy*, 78(1):191–195, 2011.

[30] P. Ehrenfreund, W.F.M. Röling, C.S. Thiel, R. Quinn, M.A. Sephton, C. Stoker, J.M. Kotler, S.O.L. Direito, Z. Martins, G.E. Orzechowska, R.D. Kidd, C.A. Van Sluis, and B.H. Foing. Astrobiology and habitability studies in preparation for future mars missions: Trends from investigating minerals, organics and biota. *International Journal of Astrobiology*, 10(3):239–253, 2011.

[31] A. Ellery, D. Wynn-Williams, J. Parnell, H. G. M. Edwards, and D. Dickensheets. The role of Raman spectroscopy as an astrobiological tool in the exploration of Mars. *Journal of Raman Spectroscopy*, 35(6):441–457, 2004.

[32] E. Eshelman, M.G. Daly, G. Slater, P. Dietrich, and J.-F. Gravel. An ultraviolet raman wavelength for the in-situ analysis of organic compounds relevant to astrobiology. *Planetary and Space Science*, 93-94:65–70, 2014.

[33] Alberto G. Fairen, Alfonso F. Davila, and et al. Astrobiology through the Ages of Mars: The Study of Terrestrial Analogues to Understand the Habitability of Mars. *ASTROBIOLOGY*, 10(8), 2010.

[34] K. A. Farley, C. Malespin, P. Mahaffy, J. P. Grotzinger, P. M. Vasconcelos, R. E. Milliken, M. Malin, K. S. Edgett, A. A. Pavlov, J. A. Hurowitz, J. A. Grant, H. B. Miller, R. Arvidson, L. Beegle, F. Calef, P. G. Conrad, W. E. Dietrich, J. Eigenbrode, R. Gellert, S. Gupta, V. Hamilton, D. M. Hassler, K.W. Lewis, S. M. McLennan, D. Ming, R. Navarro-González, S. P. Schwenzer, A. Steele, E. M. Stolper, D. Y. Sumner, D. Vaniman, A. Vasavada, K. Williford, R. F. Wimmer-Schweingruber, and . In situ radiometric and exposure age dating of the martian surface. *Science*, 343(6169), 2014.

[35] M.R. Fisk, M.C. Storrie-Lombardi, S. Douglas, R. Popa, G. McDonald, and C. Di Meo-Savoie. Evidence of biological activity in hawaiian subsurface basalts. *Geochemistry, Geophysics, Geosystems*, 4(12), 2003.

[36] S.P.A. Fodor, R.P. Rava, T.R. Hays, and T.G. Spiro. Ultraviolet resonance raman spectroscopy of the nucleotides with 266-, 240-, 218-, and 200-nm pulsed laser excitation. *Journal of the American Chemical Society*, 107(6):1520–1529, 1985.

[37] O. Frank, J. Jehlička, and H.G.M. Edwards. Raman spectroscopy as tool for the characterization of thio-polyaromatic hydrocarbons in organic minerals. *Spectrochimica Acta - Part A: Molecular and Biomolecular Spectroscopy*, 68(4):1065–1069, 2007.

[38] C. Freissinet, D. P. Glavin, P. R. Mahaffy, K. E. Miller, J. L. Eigenbrode, R. E. Summons, A. E. Brunner, A. Buch, C. Szopa, P. D. Archer, H. B. Franz, S. K. Atreya, W. B. Brinckerhoff, M. Cabane, P. Coll, P. G. Conrad, D. J. Des Marais, J. P. Dworkin, A. G. Fairén, P. François, J. P. Grotzinger, S. Kashyap, I. L. ten Kate, L. A. Leshin, C. A. Malespin, M. G. Martin, F. J. Martin-Torres, A. C. McAdam, D. W. Ming, R. Navarro-González, A. A. Pavlov, B. D. Prats, S. W. Squyres, A. Steele, J. C. Stern, D. Y. Sumner, B. Sutter, M.-P. Zorzano, and the MSL Science Team. Organic molecules in the sheepbed mudstone, gale crater, mars. *Journal of Geophysical Research: Planets*, 120(3):495–514, 2015.

[39] C. Freissinet, D.P. Glavin, P.R. Mahaffy, K.E. Miller, J.L. Eigenbrode, R.E. Summons, A.E. Brunner, A. Buch, C. Szopa, Jr. Archer, P.D., H.B. Franz, S.K. Atreya, W.B. Brinckerhoff, M. Cabane, P. Coll, P.G. Conrad, D.J. Des Marais, J.P. Dworkin, A.G. Fairén, P. François, J.P. Grotzinger, S. Kashyap, I.L.

Ten Kate, L.A. Leshin, C.A. Malespin, M.G. Martin, F.J. Martin-Torres, A.C. Mcadam, D.W. Ming, R. Navarro-González, A.A. Pavlov, B.D. Prats, S.W. Squyres, A. Steele, J.C. Stern, D.Y. Sumner, B. Sutter, and M.-P. Zorzano. Organic molecules in the sheepbed mudstone, gale crater, mars. *Journal of Geophysical Research E: Planets*, 120(3):495–514, 2015.

[40] T. Frosch, N. Tarcea, M. Schmitt, H. Thiele, F. Langenhorst, and J. Popp. UV Raman imaging - A promising tool for astrobiology: Comparative Raman studies with different excitation wavelengths on SNC Martian meteorites. *Analytical Chemistry*, 79(3):1101–1108, 2007.

[41] T. Frosch, N. Tarcea, M. Schmitt, H. Thiele, F. Langenhorst, and J. Popp. UV Raman imaging - A promising tool for astrobiology: Comparative Raman studies with different excitation wavelengths on SNC Martian meteorites. *Analytical Chemistry*, 79(3):1101–1108, 2007.

[42] M. Gaft and G. Panczer. Laser-induced time-resolved luminescence spectroscopy of minerals: A powerful tool for studying the nature of emission centres. *Mineralogy and Petrology*, 107(3):363–372, 2013.

[43] Rafael Navarro Gonzalez, Edgar Vargas, Jose de la Rosa, Alejandro C. Raga, and Christopher P. McKay. Reanalysis of the viking results suggests perchlorate and organics at midlatitudes on mars. *Journal of Geophysical Research E: Planets*, 116, 2011.

[44] Belen Hernandez, Fernando Pfluger, Mama Nsangou, and Mahmoud Ghomi. Vibrational Analysis of Amino Acids and Short Peptides in Hydrated Media. *J. Phys. Chem. B*, 113:3169–3178, 2009.

[45] J. A. Hiscox. An overview of the origin of life: The case for biological prospecting on mars. *Earth, Moon and Planets*, 87(3):191–212, 1999.

[46] N.K. Howell, G. Arteaga, S. Nakai, and E.C.Y. Li-Chan. Raman spectral analysis in the C - H stretching region of proteins and amino acids for investigation of hydrophobic interactions. *Journal of Agricultural and Food Chemistry*, 47(3):924–933, 1999.

[47] W.F. Hug, R. Bhartia, A. Taspin, A. Lane, P. Conrad, K. Sijapati, and R.D. Reid. Status of miniature integrated uv resonance fluorescence and raman sensors for detection and identification of biochemical warfare agents. volume 5994, 2005.

[48] M.R.M. Izawa, D.M. Applin, L. Norman, and E.A. Cloutis. Reflectance spectroscopy (350-2500 nm) of solid-state polycyclic aromatic hydrocarbons (pahs). *Icarus*, 237:159–181, 2014.

[49] S. Jarmelo, P. R. Carey, and R. Fausto. The Raman spectra of serine and 3,3-dideutero-serine in aqueous solution. *Vibrational Spectroscopy*, 43:104–110, 2007.

[50] J. Jehlička, H. G. M. Edwards, and P. Vítek. Assessment of Raman spectroscopy as a tool for the non-destructive identification of organic minerals and biomolecules for Mars studies. *Planetary and Space Science*, 57(5-6):606–613, 2009.

[51] J. Jehlička, H.G.M. Edwards, S.E. Jorge Villar, and O. Frank. Raman spectroscopic study of the complex aromatic mineral idrialite. *Journal of Raman Spectroscopy*, 37(7):771–776, 2006.

[52] J. Jehlička, P. Vítek, H.G.M. Edwards, M. Heagraves, and T. Čapoun. Application of portable raman instruments for fast and non-destructive detection of minerals on outcrops. *Spectrochimica Acta - Part A: Molecular and Biomolecular Spectroscopy*, 73(3):410–419, 2009.

[53] R.B. Johns, F.D. Looney, and D.J. Whelan. Photochemistry of biological molecules. i. photolysis of amino acids in the solid state. *BBA - Protein Structure*, 147(2):369–380, 1967.

[54] J. R. Johnson. MEPAG (2010), Mars Scientific Goals, Objectives, Investigations, and Priorities. Technical report, Mars Exploration Program Analysis Group (MEPAG), 2010.

[55] Bent Jørgensen, Yuri Goegebeur, and Module Chemometrics. Department of statistics st02: Multivariate data analysis and chemometrics. 2007.

[56] R.A. Kerr. Search for martian life clears another hurdle. *Science*, 343(6178):1419, 2014.

[57] P. Klaeboe, S.J. Cyvin, A.Phongsatha Asbjørnsen, and B.N. Cyvin. Condensed aromatics—XIV. Fluoranthene. *Spectrochimica Acta Part A: Molecular Spectroscopy*, 37(8):655–661, 1981.

[58] Santosh Kumar, Amareshwar Kumar Rai, S. B. Rai, K. D. Rai, A. N. Singh, and V. B. Singh. Infrared, Raman and electronic spectra of alanine: A comparison with ab inito calculation. *Journal of Molecular Structure*, 791:23–29, 2006.

[59] Joseph R. Lakowicz. *Principles of Fluorescence Spectroscopy*. Springer, 3rd edition edition, 2006.

[60] Daimay Lin-Vien, Norman B. Colthup, William G. Fateley, and Jeanette G. Grasselli. *The Handbook of Infrared and Raman Characteristic Frequencies of Organic Molecules*. Academic Press, Inc., 1991.

[61] J.L. Lippert and W.L. Peticolas. Raman active vibrations in long-chain fatty acids and phospholipid sonicates. *Biochimica et Biophysica Acta (BBA) - Biomembranes*, 282(0):8–17, 1972.

[62] Derek A. Long. *The Raman Effect: A Unified Treatment of the Theory of Raman Scattering by Molecules*. John Wiley and Sons, Ltd, 2002.

[63] G. Ma, N. Mincu, F. Lesage, P. Gallant, and L. McIntosh. System irf impact on fluorescence lifetime fitting in turbid medium. volume 5699, pages 263–273, 2005.

[64] W.F. Maddams and I.A.M. Royaud. The characterization of polycyclic aromatic hydrocarbons by Raman spectroscopy. *Spectrochimica Acta*, 46A(2):309–314, 1990.

[65] W.F. Maddams and I.A.M. Royaud. The characterization of polycyclic aromatic hydrocarbons by Raman spectroscopy. *Spectrochimica Acta Part A: Molecular Spectroscopy*, 46(2):309–314, 1990.

[66] C. P. Marshall, S. Leuko, C. M. Coyle, M. R. Walter, B. P. Burns, and B. A. Neilan. Carotenoid analysis of halophilic archaea by resonanace Raman spectroscopy. *Astrobiology*, 7, 2007.

[67] Craig P. Marshall and Alian Wang. Considerations for the collection of Raman spectra of potential Martian biosignatures. *Book of Abstracts: GeoRaman 2010*, 2010.

[68] P Marshall, Howell G.M. Edwards, and Jan Jehlicka. Understanding the Application of Raman Spectroscopy to the Detection of Traces of Life. *Astrobiology*, 10(2):229–243, 2010.

[69] C.P. McKay. An approach to searching for life on mars, europa, and enceladus. *Space Science Reviews*, 135(1-4):49–54, 2008.

[70] A. D. McNaught and A. Wilkinson. Iupac. *Compendium of Chemical Terminology, 2nd ed. (the "Gold Book")*, 1997.

[71] S.L. Meloni and S. Matsika. Theoretical studies of the excited states of p-cyanophenylalanine and comparisons with the natural amino acids phenylalanine and tyrosine. *Theoretical Chemistry Accounts*, 133(7):1–13, 2014.

[72] A.K. Misra, S.K. Sharma, T.E. Acosta, J.N. Porter, and D.E. Bates. Single-pulse standoff raman detection of chemicals from 120 m distance during daytime. *Applied Spectroscopy*, 66(11):1279–1285, 2012.

[73] MRR-SAG. Mars Astrobiology Explorer-Cacher: A potential rover mission for 2018, Final report. Technical report, MEPAG MRR-SAG, 2009.

[74] H. Okabayashi and T. Kitagawa. Assignments of the CH Stretching Raman Lines of Hydrocarbon Chains. Raman Spectra of Normal Cn-1H2n-1COOK (n=3,4,6,7,10,12,14,16, and 18) and Their Specifically Deuterated Derivatives. *The Journal of Physical Chemistry*, 82(16), 1978.

[75] Gordon R. Osinski, Richard Leveil-le, Alain Berinstain, Martin Lebeuf, and Matthew Bamsey. Terrestrial Analogues to Mars and the Moon: Canada's Role. *Geoscience Canada*, 33(4), 2006.

[76] J. Parnell, D. Cullen, M.R. Sims, S. Bowden, C.S. Cockell, R. Court, P. Ehrenfreund, F. Gaubert, W. Grant, V. Parro, M. Rohmer, M. Sephton, H. Stan-Lother, A. Steele, J. Toporski, and J. Vago. Searching for life on mars: Selection of molecular targets for esa's aurora exomars mission. *Astrobiology*, 7(4):578–604, 2007.

[77] V.A. Petryshyn, D. Lim, B.L. Laval, A. Brady, G. Slater, and A.K. Tripati. Reconstruction of limnology and microbialite formation conditions from carbonate clumped isotope thermometry. *Geobiology*, 13(1):53–67, 2015.

[78] I. Porat, B.W. Waters, Q. Teng, and W.B. Whitman. Two biosynthetic pathways for aromatic amino acids in the archaeon methanococcus maripaludis. *Journal of Bacteriology*, 186(15):4940–4950, 2004.

[79] C.V. Raman and K.S. Krishnan. A New Type of Secondary Radiation. *Nature*, 121, 1928.

[80] R. P. Rava and T. G. Spiro. Resonance enhancement in the ultraviolet Raman spectra of aromatic amino acids. *Journal of Physical Chemistry*, 89(10):1856–1861, 1985.

[81] Eric Le Ru and Pablo Etchegoin. *Principles of Surface-Enhanced Raman Spectroscopy and related plasmonic effects*. Elsevier, 2009.

[82] Robert K. Sato and Paul F. McMillan. An Infrared and Raman Study of the Isotopic Species of alpha-Quartz. *American Chemical Society*, 43:908, 1958.

[83] S.P. Schwenzer, O. Abramov, C.C. Allen, J.C. Bridges, S.M. Clifford, J. Filiberto, D.A. Kring, J. Lasue, P.J. McGovern, H.E. Newsom, A.H. Treiman, D.T. Vaniman, R.C. Wiens, and A. Wittmann. Gale crater: Formation and

post-impact hydrous environments. *Planetary and Space Science*, 70(1):84 – 95, 2012.

[84] S. K. Sharma, P. G. Lucey, M. Ghosh, H. W. Hubble, and K. A. Horton. Stand-off Raman spectroscopic detection of minerals on planetary surfaces. *Spectrochimica Acta - Part A: Molecular and Biomolecular Spectroscopy*, 59(10):2391–2407, 2003.

[85] S.K. Sharma. New trends in telescopic remote raman spectroscopic instrumentation. *Spectrochimica Acta - Part A: Molecular and Biomolecular Spectroscopy*, 68(4):1008–1022, 2007.

[86] S.K. Sharma, A.K. Misra, T.E. Acosta, and P.G. Lucey. Time-resolved remote raman and fluorescence spectrometers for planetary exploration. volume 8379, 2012.

[87] D. F. Shriver and J. B. R. Dunn. The backscattering geometry for raman spectroscopy of colored materials. *Applied Spectroscopy*, 28(4):319–323, 1974.

[88] A. Sidike, X.-M. Wang, A. Sawuti, H.-J. Zhu, I. Kusachi, and N. Yamashita. Energy transfer among pb, ce and mn in fluorescent calcite from kuerle, xinjiang, china. *Physics and Chemistry of Minerals*, 33(8-9):559–566, 2006.

[89] W. L. Sjogren and W. R. Wollenhaupt. Lunar shape via the Apollo laser altimeter. *Science*, 179(4070):275–278, 1973.

[90] R. G. Snyder, S. L. Hsu, and S. Krimm. Vibrational spectra in the C-H stretching region and the structure of the polymethylene chain. *Spectrochimica Acta*, 34A:395–406, 1978.

[91] George Socrates. *Infrared and Raman Characteristic Group Frequencies*. John Wiley and Sons, Ltd, 2001.

[92] S.M. Som and B.H. Foing. Thermal degradation of organic material by portable laser raman spectrometry. *International Journal of Astrobiology*, 11(3):177–186, 2012.

[93] Fabien Stalport, Patrice Coll, Michael Cabane, Alain Person, Rafael Navarro Gonzalez, Francois Raulin, Marie Jo Vaulay, Patrick Ausset, Chris P. McKay, Cyril Szopa, and John Zarnecki. Search for past life on Mars: Physical and chemical characterization of minerals of biotic and abiotic origin: part 1 - Calcite. *Geophysical Research Letters*, 32, 2005.

[94] G. G. Stokes. On the change of refrangibility of light. *Philisophical Transactions of The Royal Society of London*, 142:463–562, 1852.

[95] M.C. Storrie-Lombardi, W.F. Hug, G.D. McDonald, A.I. Tsapin, and K.H. Nealson. Hollow cathode ion lasers for deep ultraviolet raman spectroscopy and fluorescence imaging. *Review of Scientific Instruments*, 72(12):4452–4459, 2001.

[96] M.C. Storrie-Lombardi, J.P. Muller, M.R. Fisk, C. Cousins, B. Sattler, A.D. Griffiths, and A.J. Coates. Laser-induced fluorescence emission (l.i.f.e.): searching for mars organics with a uv-enhanced pancam. *Astrobiology*, 9(10):953–964, 2009.

[97] S. J. Strickler and R. A. Berg. Relationship between absorption intensity and fluorescence lifetime of molecules. *J. Chem. Phys*, 37(4):814–822, 1962.

[98] Wade R. Thompson and Jeanne E. Pemberton. Characterization of Octadecylsilane and Stearic Acid Layers on Al2O3 Surfaces by Raman Spectroscopy. *Langmuir*, 11:1720–1725, 1995.

[99] Marvin C. Tobin. *Laser Raman Spectroscopy*, volume 35. Robert E. Krieger Publishing Company, 2nd edition, 1982.

[100] H.E. Van Wart and H.A. Scheraga. Raman spectra of cystine-related disulfides. Effect of rotational isomerism about carbon-sulfur bonds on sulfur-sulfur stretching frequencies. *Journal of Physical Chemistry*, 80(16):1812–1823, 1976.

[101] P. Vandenabeele. Evaluation of a spectral searching algorithm for the comparison of raman band positions. *Spectrochimica Acta - Part A: Molecular and Biomolecular Spectroscopy*, 80(1):27–31, 2011.

[102] P. Vandenabeele and J. Jehlička. Mobile raman spectroscopy in astrobiology research. *Philosophical Transactions of the Royal Society A: Mathematical, Physical and Engineering Sciences*, 372(2030), 2014.

[103] P. Vandenabeele, J. Jehlička, P. Vítek, and H.G.M. Edwards. On the definition of raman spectroscopic detection limits for the analysis of biomarkers in solid matrices. *Planetary and Space Science*, 62(1):48–54, 2012.

[104] A. Varagnat, G. Cairns, and G. Hancock. Smarter ICCD cameras exploit their speed potential. *Laser Focus World*, 47(9):46–49, 2011.

[105] C.M. Vetromile and D.M. Jameson. Frequency domain fluorometry: Theory and application. *Methods in Molecular Biology*, 1076:77–95, 2014.

[106] S. E. J. Villar, H. G. M. Edwards, and M. R. Worland. Comparative evaluation of Raman spectroscopy at different wavelengths for extremophile exemplars. *Origins of Life and Evolution of the Biosphere*, 35(5):489–506, 2005.

[107] P. Vitek, E. Ali, H. G. M. Edwards, J. Jehlicka, R. Cox, and K. Page. Evaluation of portable raman spectrometer with 1064 nm excitation for geological and forensic applications. *Spectrochimica Acta - Part A: Molecular and Biomolecular Spectroscopy*, 86:320–327, 2012.

[108] P. Vitek, H. G. M. Edwards, J. Jehlicka, C. Ascaso, A. De Los Rios, S. Valea, S. E. Jorge-Villar, A. F. Davila, and J. Wierzchos. Microbial colonization of halite from the hyper-arid Atacama Desert studied by Raman Spectroscopy. *Philisophical Transactions of The Royal Society A*, (368):3205–3221, 2010.

[109] P. Vítek, J. Jehlička, C. Ascaso, V. Mašek, B. Gómez-Silva, H. Olivares, and J. Wierzchos. Distribution of scytonemin in endolithic microbial communities from halite crusts in the hyperarid zone of the atacama desert, chile. *FEMS Microbiology Ecology*, 90(2):351–366, 2014.

[110] S. De Vries and Cajo J.F. Ter Braak. Prediction error in partial least squares regression: a critique on the deviation used in the unscrambler. *Chemometrics and Intelligent Laboratory Systems*, 30:239–245, 1995.

[111] M. Wahl, H.-J. Rahn, U. Ortmann, R. Erdmann, M. Böhmer, and J. Enderlein. Fluorescence lifetime imaging system with nm-resolution and single molecule sensitivity. volume 4634, pages 104–111, 2002.

[112] James Whiteway, Michael Daly, Allan Carswell, Thomas Duck, Cameron Dickinson, Leonce Komguem, and Clive Cook. Lidar on the Phoenix mission to Mars. *Journal of Geophysical Research: Planets (1991–2012)*, 113(E3), 2008.

[113] J. Wierzchos, B. Camara, A. De Los Rios, A. F. Davila, I. M. Sanchez Almazo, O. Artieda, K. Wierzchos, B. Gomez-Silva, C. McKay, and C. Ascaso. Microbial colonization of Ca-sulfate crusts in the hyperarid core of the Atacama Desert: implications for the search for life on Mars. *Geobiology*, 9:44–60, 2011.

[114] E. Wilson, J. Decius, and P. Cross. *Molecular Vibrations: The Theory of Infrared and Raman Vibrational Spectra*. McGraw-Hill Book Company, New York, 1955.

[115] Zili Wo, Chao Zhang, and Peter C. Stair. Influence of absorption on quantitative analysis in raman spectroscopy. *Catalysis Today*, 113:40–47, 2006.

[116] D. D. Wynn-Williams and H. G. M. Edwards. Proximal Analysis of Regolith Habitats and Protective Biomolecules in Situ by Laser Raman Spectroscopy: Overview of Terrestrial Antarctic Habitats and Mars Analogs. *Icarus*, 144(2):486–503, 2000.

[117] G. Zhu, X. Zhu, Q. Fan, and X. Wan. Raman spectra of amino acids and their aqueous solutions. *Spectrochimica Acta - Part A: Molecular and Biomolecular Spectroscopy*, 78(3):1187–1195, 2011.

[118] Lori A. Ziolkowski, Jacek Wiezchos, Alfonso F. Davila, and Gregory F. Slater. Radiocarbon evidence of active endolithic microbial communities in the hyperarid core of the atacama desert. *Astrobiology*, 13(7):607–616, 2013.

8 Appendices

8.1 ICCD overview

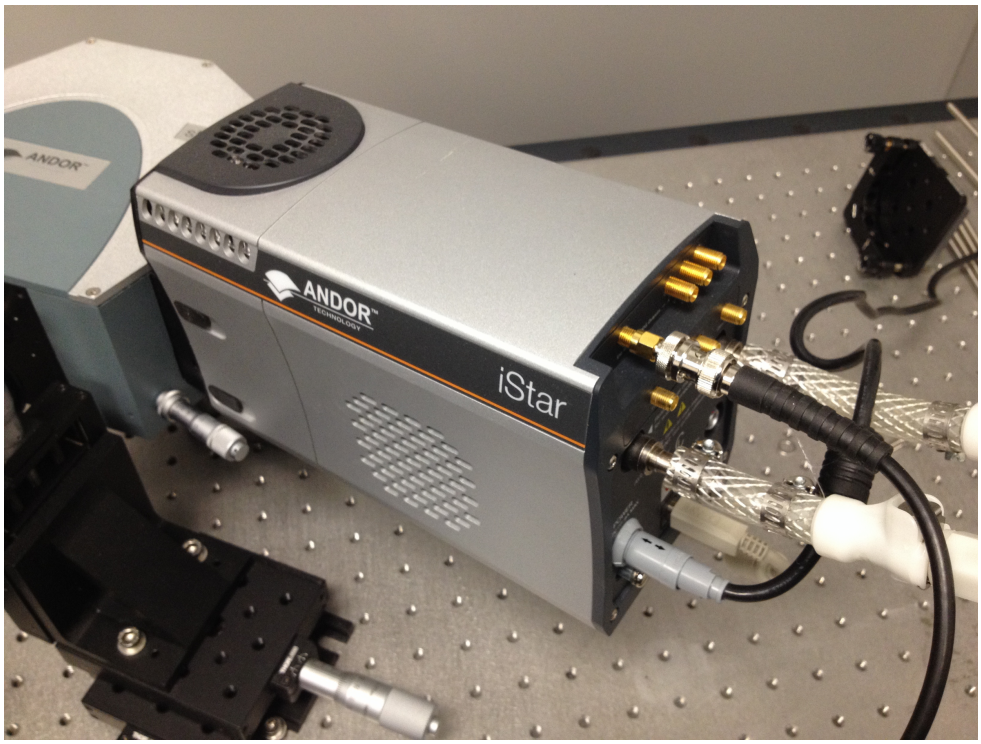

Figure 50: Andor iCCD detector incorporated into the 266 nm Raman instrument breadboard

Raman and fluorescence photons are detected using an intensified CCD (Andor iStar 334T) water-cooled to -38^{o}C. Light entering the detector is directed onto an Ø18 mm photocathode, generating photoelectrons which are amplified in an intensifier tube. A phosphor converts the intensified electron cloud into visible photons detectable by the 1024 x 1024 pixel CCD with 13 μm pixels. Intensified CCD detectors have capabilities distinct from both traditional CCDs and PMTs. The purpose of this appendix is to detail the manner in which incident photons are converted to digital spectra using diagrams reproduced from the camera manufacturer, and to define terms used throughout this work unique to ICCDs.

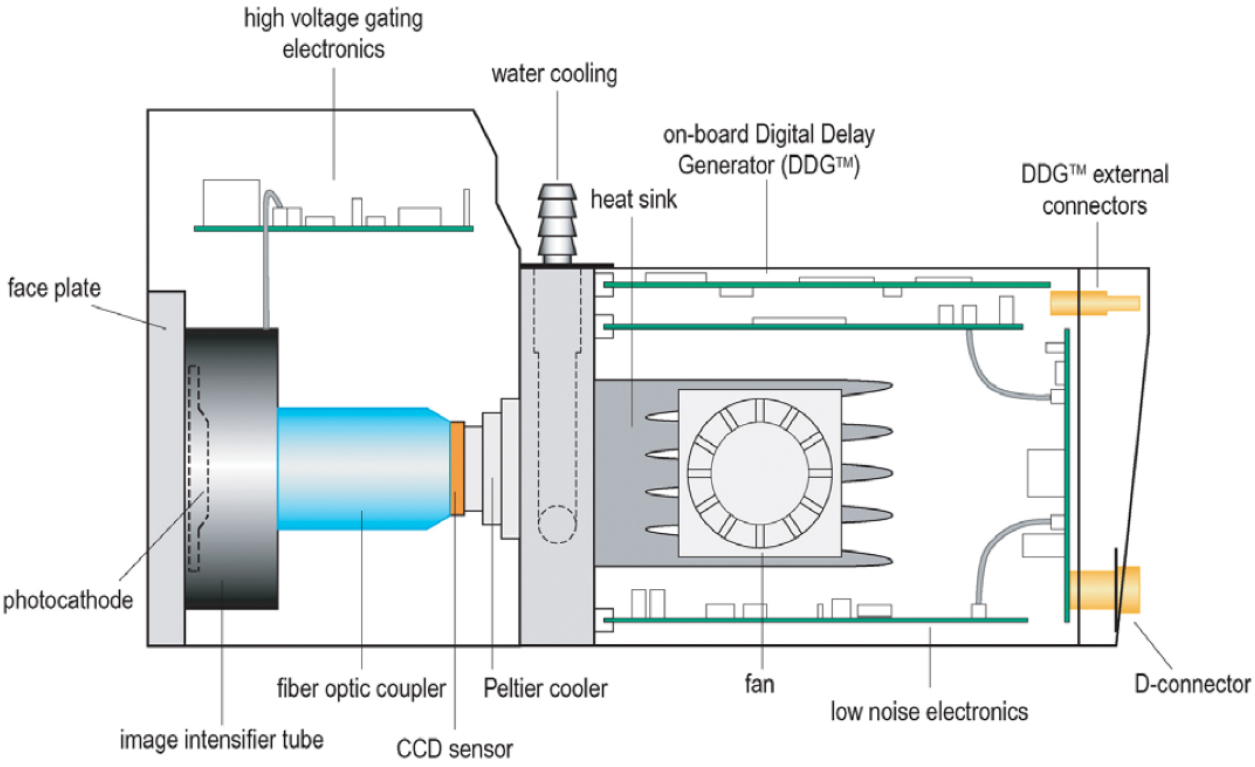

Figure 51: Andor iCCD schematic, reproduced from the Andor iStar manual

Figure 50 shows the Andor iStar USB model iCCD 334T-18U-E3, integrated into the 266 nm Raman breadboard and attached to the grating spectrometer. The inputs attached to the back of the camera, from top to bottom, are the external trigger for the digital delay generator (DDG), input and output for the chiller/water recirculator, camera power, and a USB connection to the computer. The internals of the detector are presented in Figure 51, reprinted from the manufacturer. The pathway from incident photon to charge on the CCD involves, in order, the image intensifier, fiber coupler, and CCD sensor.

Image intensifier tube

Photons entering the detector are projected onto the photocathode, the first component of the image intensifier tube, by the grating spectrometer. The interior of the intensifier is evacuated, and electrons produced at the photocathode are directed by an electric field towards the Micro Channel Plate (MCP), a thin disk consisting of micron-scale channels with a strong voltage potential between the two ends. This potential causes the electrons to cascade through the MCP, generating a cloud of electrons in the process and amplifying the signal. Exiting the MCP, the electron cloud is further accelerated by a strong potential towards phosphor, which generates visible-wavelength photons when struck by the electron cloud. The gain of the acquired signal can be controlled by changing the voltage across the MCP, affecting the production of secondary electrons. With voltage across the channel at its lowest value, a gain of zero is possible and the iCCD sensitivity is reduced to approximately the sensitivity of a traditional CCD. With a maximum gain, the signal can be amplified up to 10^4 and single photons can be detected. The quantum efficiency of the detector is dependent on the photocathode, the component that interacts with incident light. Figure 52 presents the QE curve for the photocathode used in this work (-E3), which provides a QE above 20% in the ultraviolet. Background noise from the intensifier is less than 0.02 photoelectrons/pixel/sec.

Fiber coupler and CCD

The CCD that obtains the image is attached to the phosphor using a fiber coupler, allowing high efficiencies and low amounts of optical distortion. The CCD is cooled using a water-assisted thermoelectric cooler. While the photocathode will open and close once for every laser pulse, and therefore light will strike the CCD once per

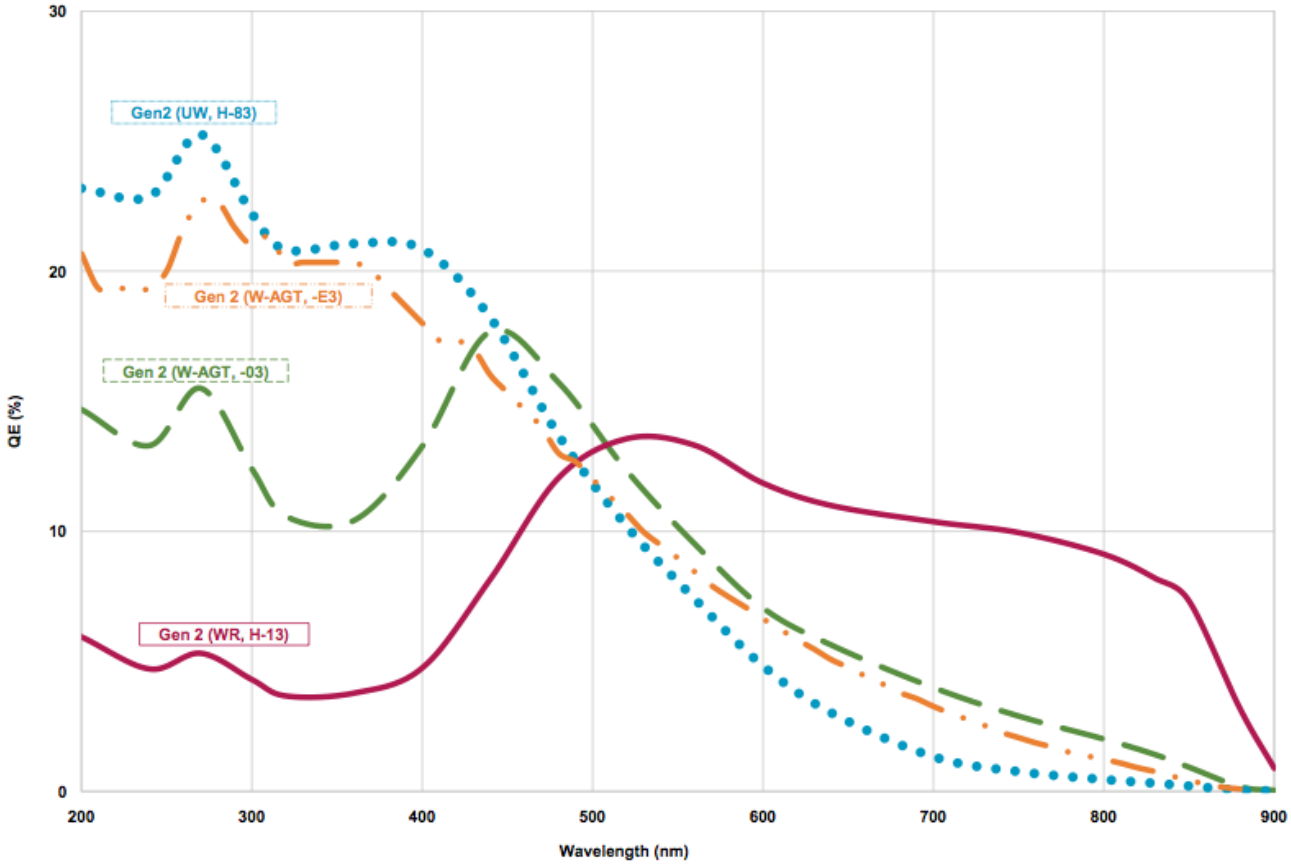

Figure 52: Andor photocathode quantum efficiency curves, reproduced from the Andor iStar manual

pulse, it is not ideal to read the CCD charge out to the computer every pulse, as this would introduce large amounts of readout-noise. Instead, charge is accumulated on the CCD over 50-250 pulses (depending on the laser repetition rate) and read out to the computer every 0.05 seconds. To further reduce readout noise, charge on the CCD is not read out per pixel, but instead the integrated charge on the CCD is summed along vertical columns of pixels, and a single 1x1024 array of data is read out to the computer. The dynamic range of the CCD is highest (16 bits) when the gain is low, but is reduced by a factor of 1000 when the gain is maximized as the saturation point of the CCD remains constant regardless of the size of the photon cloud.

Digital Delay Generator (DDG)

The sub-nanosecond timing of the opening and closing of the photocathode to match the incoming light pulse is accomplished by a trigger signal sent to the DDG when a laser pulse fires. Successful acquisition of a signal is contingent on the trigger signal reaching the detector at least 40 ns before the Raman or fluorescence light, allowing the electronics in the DDG to wait until the moment the laser pulse arrives at the photocathode, and open the gate for the duration of the pulse. The three controllable parameters that dictate this timing are the distance photons travel from the laser to the sample and to the detector, the gate delay, and the gate width. In this work the photon travel time from the laser exit to the sample and then to the photocathode, assuming instantaneous scattering off the sample, is around 45-50 ns. The gate delay may then be set to between 5 and 10 ns, and the gate width to 2.9-20 ns depending on the experiment. Both the gate delay and gate width have a resolution of 25 ps, with a minimum gate width of 1.5 ns.

Converting counts to incident photons

Intensity is read out to the computer in units of 'counts'. The relation between incoming photons and counts is given below.

$$\gamma = \frac{(\text{Counts} - \text{Offset}) \times \text{Sensitivity}}{\text{Gain}_{\text{MCP}} \times \text{QE}(\lambda)} \tag{35}$$

The offset and sensitivity were calibrated by the manufacturer, and a performance curve provided.

Instrument parameters

A table of typical detector parameters that was saved alongside each acquisition is presented below.

Parameter	Typical value
Date and Time	-
Software Version	4.20.30007.0
Temperature (C)	-38 C
Model	DH334t_FI_18mm
Data Type	Counts
Acquisition Mode	Accumulate
Trigger Mode	External
Exposure Time (secs)	0.05
Number of Accumulations	2000
Readout Mode	Full Vertical Binning
Vertical Shift Speed (usecs)	6.5
Pixel Readout Rate (MHz)	5
Serial Number	5159
Pre-Amplifier Gain	4
Trigger level (V)	0.5
Gain level	3000
Insertion delay	ultra fast
Intelligate	off
Integrate on chip	on
IOC frequency (Hz)	5e+05
Gate Mode	DDG on
Gate Width (nsecs)	5
Gate Delay (nsecs)	1.5

Table 8: Typical acquisition parameters and data saved alongside each acquisition

8.2 PLS algorithm

The goal of the PLS algorithm is to determine the relationship between a matrix $\mathbf{X}$ containing the spectral information and a matrix $\mathbf{y}$ containing the responses - such as concentration, decay lifetime, or other experimental quantity. $\mathbf{X}$ is an $n \times k$ matrix, where k contains the spectral data, and n represents the number of responses in the model (20 in this case). $\mathbf{y}$ is a $1 \times n$ matrix which contains the response information. Score vectors are then computed that contain information on how $\mathbf{X}$ and $\mathbf{y}$ are connected, and a number of latent variables is selected to represent the information in the model.

As an example of the benefits of multivariate models compared to uni-variate models (using only one Raman peak), limits of detection were calculated for a mixture of L-alanine and water using both multivariate and univariate methods, calculated using the accepted methodology defined by the International Union of Pure and Applied Chemistry (IUPAC). The limit of detection calculated using the multivariate calibration was found to be 0.12%, while the limit of detection calculated using the univariate calibration was 0.16%.

An overview of the PLS algorithm is presented below, reproduced from Jørgensen et al. [55].

$$\mathbf{w}_j = \frac{\mathbf{X}_j^T \mathbf{y}_j}{\left\| \mathbf{X}_j^T \mathbf{y}_j \right\|} \tag{36}$$

First, the unit vector $\mathbf{w}_j$, $k \times 1$, defines the direction in the spectral information with the largest covariance.

$$\mathbf{t}_j = \mathbf{X}_j \mathbf{w}_j \tag{37}$$

The score vector $\mathbf{t}_j$, $n \times 1$, is formed, also called a latent vector. The regression coefficient, $\hat{c}_j$, is formed by regression of the responses on the latent vector.

$$\hat{c}_j = \frac{\mathbf{t}_j^\top \mathbf{y}_j}{t_j^\top t_j} \tag{38}$$

$$p_j = \frac{\mathbf{X}_j^\top \mathbf{t}_j}{\mathbf{t}_j^\top \mathbf{t}_j} \tag{39}$$

$$\mathbf{X}_{j+1} = \mathbf{X}_j - \mathbf{t}_j \mathbf{p}_j^\top \tag{40}$$

$$\mathbf{y}_{j+1} = \mathbf{y}_j - \mathbf{t}_j \hat{c}_j \tag{41}$$

Equation 41 contains the residuals after regressing the spectral data on t, and Equation 42 represents the y residuals. These steps are iterated using the residuals any number of times, generating multiple latent (score) vectors.

$$\hat{\mathbf{y}} = \mathbf{T}\hat{\mathbf{c}} \tag{42}$$

The final result of the PLS algorithm is the relation in Equation 43, relating the responses to a matrix of score vectors and the regression coefficient. A Mathematica implementation of this algorithm is provided below.

```
(* PLS1 Algorithm to identify the relative concentrations
of two compounds in a mixture. If more than two compounds
are mixed, use PLS2 instead. *)
Needs["VectorAnalysis`"];
Needs["NonlinearRegression`"];
```

```
numberLatentVars = 2;
W = {};
P = {};
T = {};
cList = {};
Do[{
   (* unit vector w gives direction in space of X with
   biggest covariance between X and y *)
   w = (X.y)/Norm[X.y];
   AppendTo[W, w];
   (* score vector t is formed as a linear combination
   of columns of X with weights w *)
   tList = w[[1, 1]] X[[1]];
   Do[{
      tList = tList + w[[i, 1]]
      X[[i]];
   }, {i, 2, len}];
   AppendTo[T, tList];

   (* regression coefficient c calculated by linear regression
   of y on t*)
   c = tList.y/(tList.tList);
   AppendTo[cList, c];
   (* p is transpose of vector of regression coefficients
   obtained from linear regressions of columns of X on t *)
   p = X.tList/(tList.tList);
```

```
    AppendTo[P, p];
    (* residual after regressing X on t *)
    X = X - Outer[Times, p, tList];

    (* residual after regressing y on t *)
    y = y - (tList c[[1]]);
}, {j, 1, numberLatentVars}];
yPre = Transpose[T].cList;
```

8.3 LabVIEW acquisition software

LabVIEW software was developed to automate data collection when performing Raman and fluorescence mapping across rock samples. As the datasets may be composed of thousands of spectra, acquisition times can take up to 10 hours to complete and manually readjusting the motors every few seconds would be unfeasible. A brief schematic of the program flow is presented below.

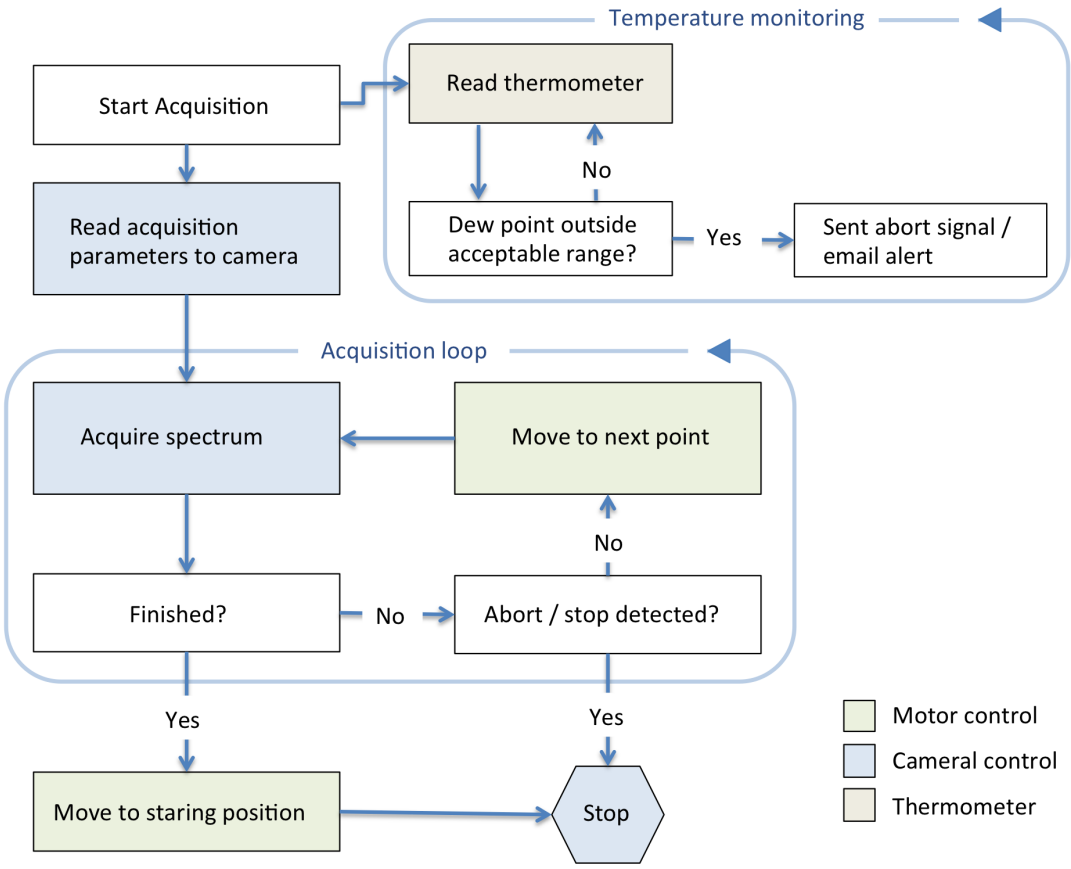

Figure 53: LabVIEW detector and motor control program flow schematic

When an acquisition starts, all camera parameters are read to the camera. The motorized sample stage is subsequently coordinated with the detector to obtain an

acquisition, move the motors, and repeat for the rows and columns across the sampling area. If desired, the height of the stage can be refocused at each spot, in which case a record will be kept of the z-height of the stage at each acquisition point. If at any time the room temperature and humidity reach a preset level, typically several degrees above the dew point, the acquisition is aborted and an email alert is sent to the operator. If the coolant temperature falls below the dew point, condensation can form and damage the detector.

Figure 54 shows the three primary LabVIEW front panels responsible for setting the detector parameters, controlling the motors, and viewing the collected data.

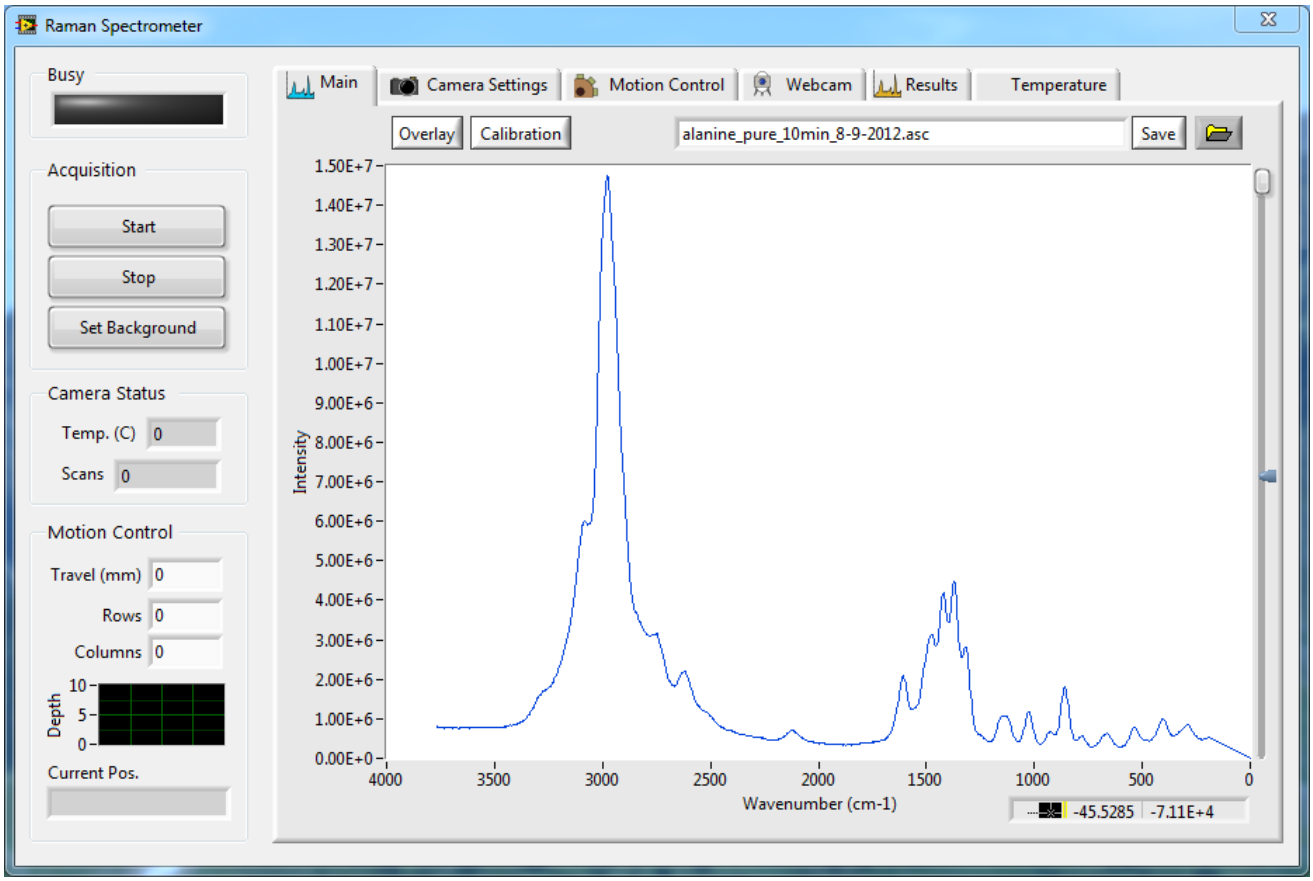

Figure 54: LabVIEW front panel diagrams for the main acquisition window

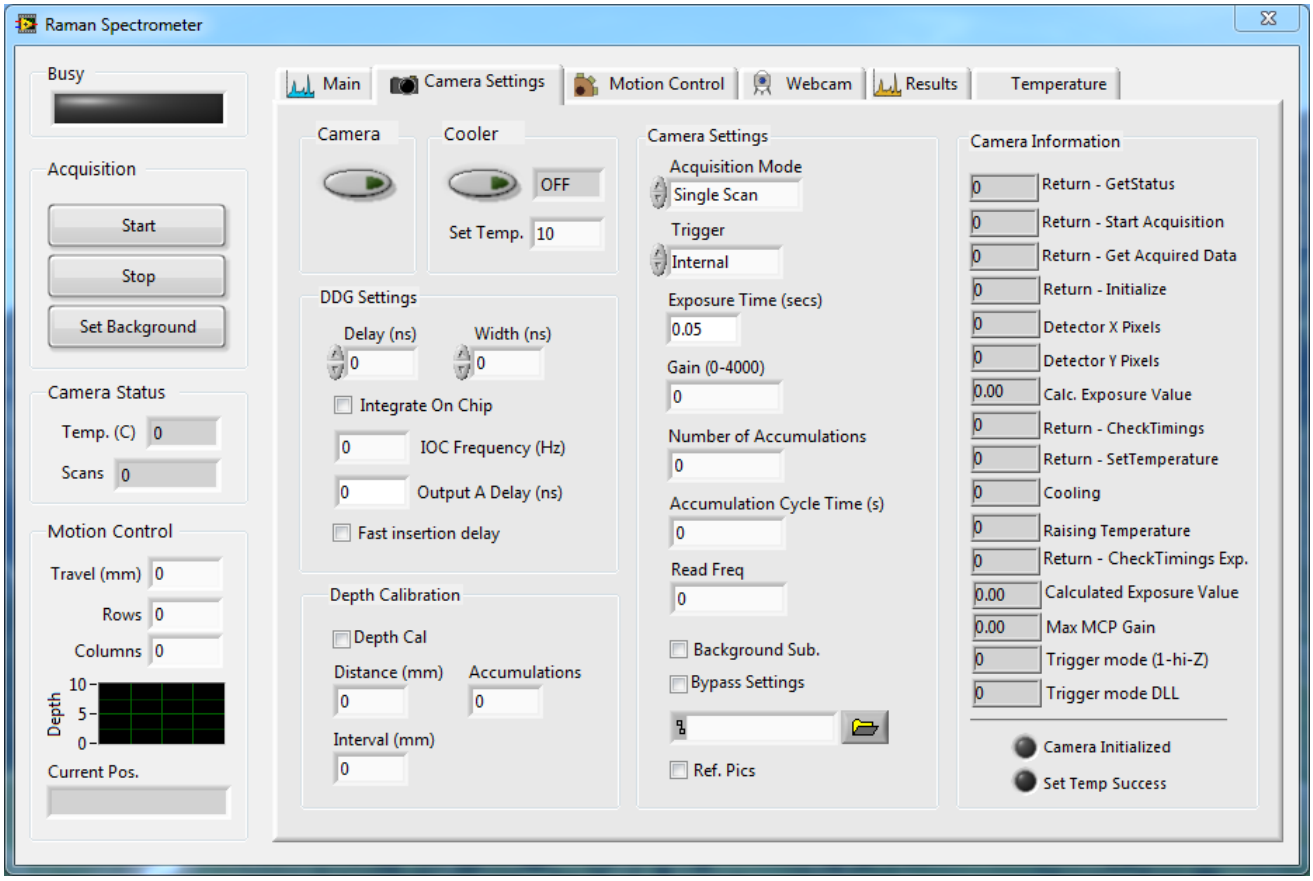

Figure 55: LabVIEW front panel diagrams for the camera setup window

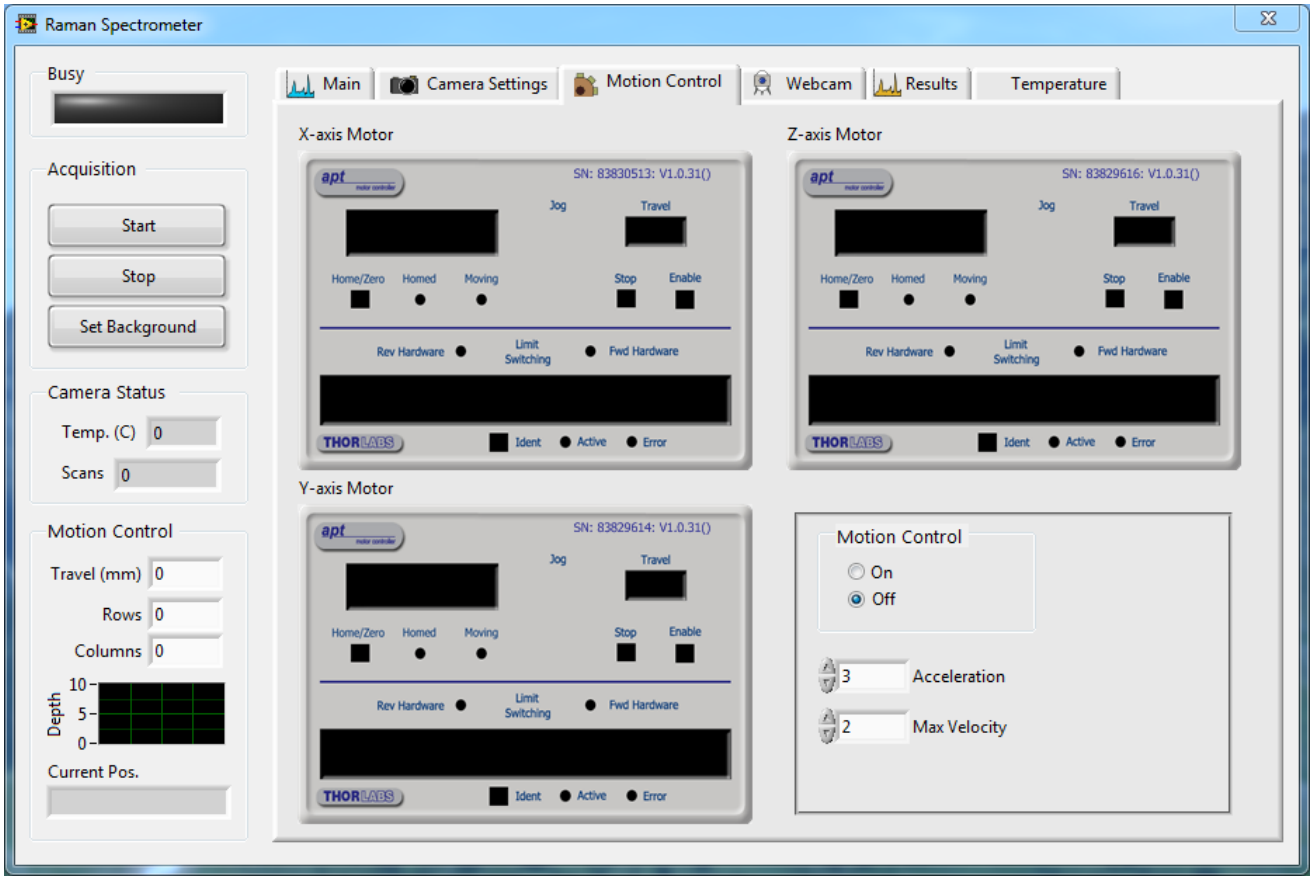

Figure 56: LabVIEW front panel diagrams for the motor control window

The LabVIEW program uses a event-driven state machine programming structure. The two event cases responsible for the acquisition and motor movements are presented in Figure 57 and Figure 58.

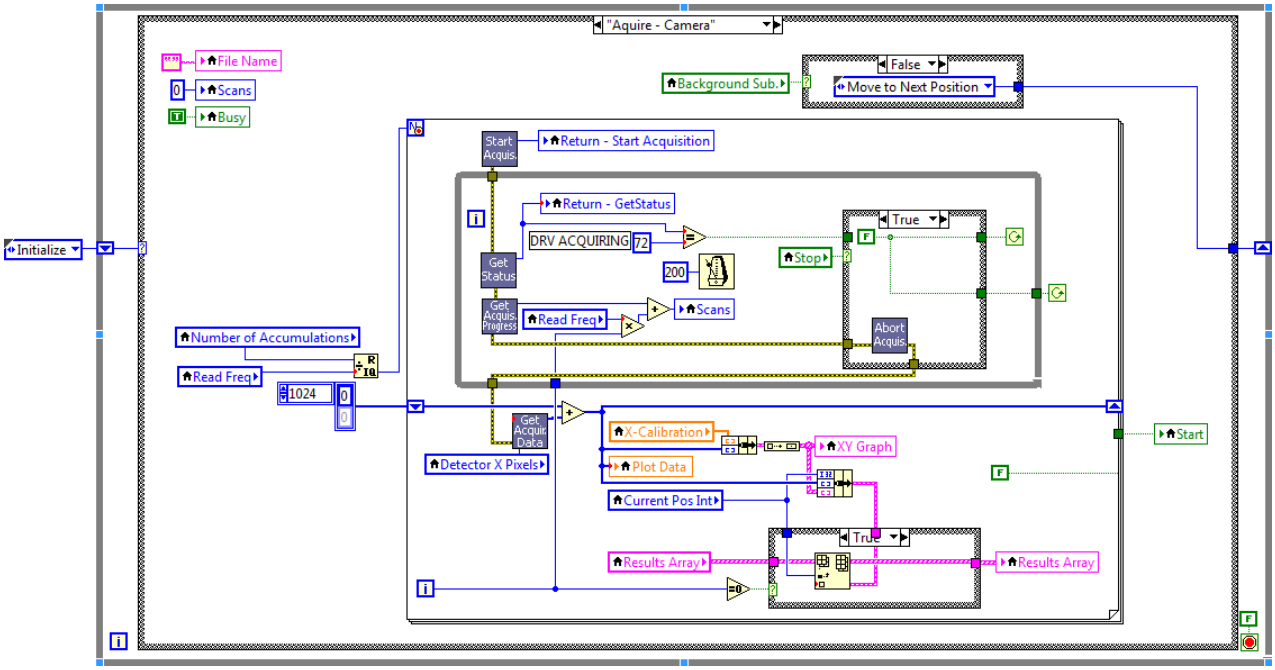

Figure 57: LabVIEW block diagram detailing camera acquisition

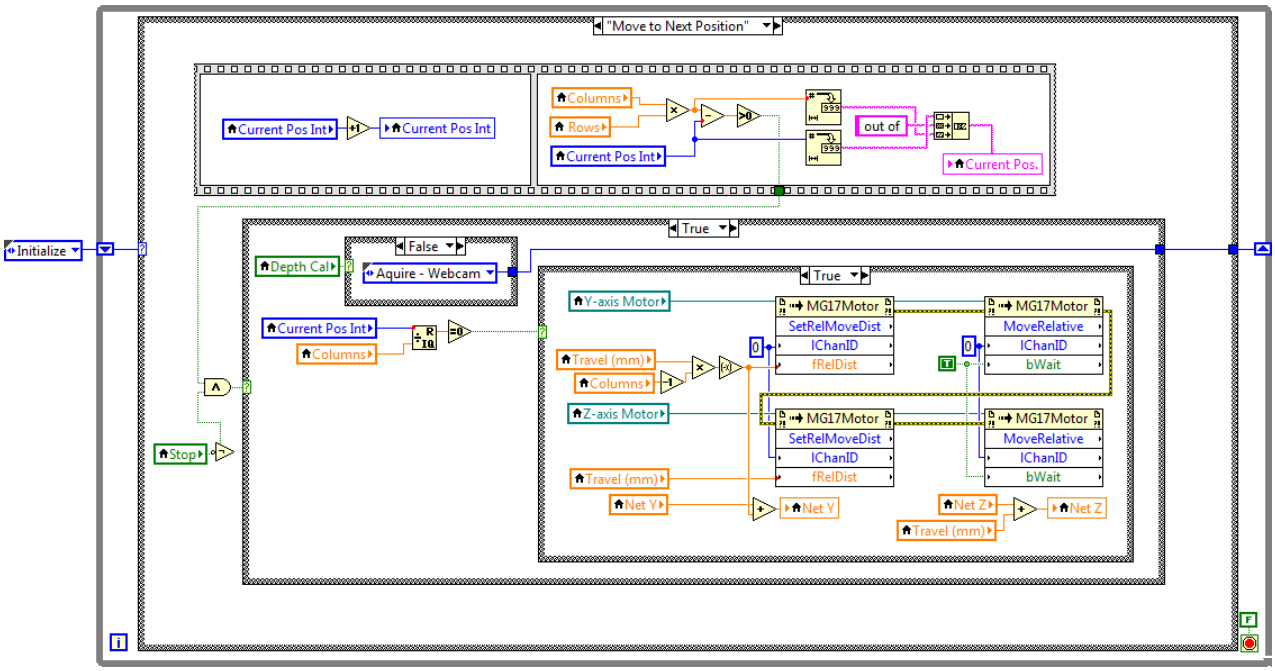

Figure 58: LabVIEW block diagram detailing motor control

8.4 A comparison of ultraviolet Raman wavelengths

This appendix presents data supplemental to section 1.5. Absorption in the ultraviolet is a competing process with Raman scattering, and if a sample exhibits absorption at the laser wavelength the Raman signal may be weakened, resulting in a non-linear relationship between sample concentration and scattering intensity. This decrease in signal can in some cases be more than offset by the fourth-power frequency dependence on scattering intensity, or by resonance Raman scattering wherein certain Raman bands will be strongly amplified when the laser excitation is close to an electronic transition in the molecule. In fact, resonance Raman effects are dependent on the incident laser energy being close to an electronic transition of the molecule.

Some organics that display poor Raman scattering in the ultraviolet compared to longer wavelengths are affected by this tradeoff between resonance enhancement and absorption. Aromatic molecules can exhibit this behavior, as the enhancement of breathing and C=C modes can be offset by absorption due to the presence of ring structures. During the course of this research, several organic compounds, all containing six-membered carbon rings, were found to display very weak Raman scattering at 266 nm, while the same compounds exhibited strong scattering at longer wavelengths including 532 nm. While a number of possible factors could not be completely ruled out, including photolytic damage due to the laser energy or loss of scatterers due to the shortness of the laser pulse, the most likely candidate for the poor signal is sample absorption. This is supported not only by the absorption spectra presented in the literature, but also by the ~1640 cm^{-1} wavenumber peaks that were visible at 266 nm. These would be the peaks expected due to resonance enhancement, which would occur at excitation energies close to electronic transitions.

The Raman spectra of l-alanine, thymine, phenylalanine, tyrosine, tryptophan,

b-carotene, and microbial mat are presented below. L-alanine was included as a baseline standard, as it contains no carbon rings and exhibits strong scattering at 266 nm. 266 nm spectra were obtained with the system presented in this work, while 355, 248, and 226 nm spectra were obtained using a separate system with a tunable ultraviolet laser. The spectrometer, grating, and detector, were similar for both sets of instrumentation. 266, 248, and 226 nm spectra were obtained with average power levels of about 2 mW, while 355 nm spectra were obtained with an average power of 360 mW. Some spectra were background subtracted to remove fluorescence that was observed in higher-wavenumber regions, and residual curve-fitting features are present.

In general, the Raman signal was weaker at shorter laser wavelengths. While some Raman peaks were not able to be observed at shorter wavelengths, the Raman feature around ~1640 cm^{-1}generally remained detectable. This feature is due to aromatic ring-breathing modes and C=C bonds which are expected to be resonantly enhanced with ultraviolet excitation.

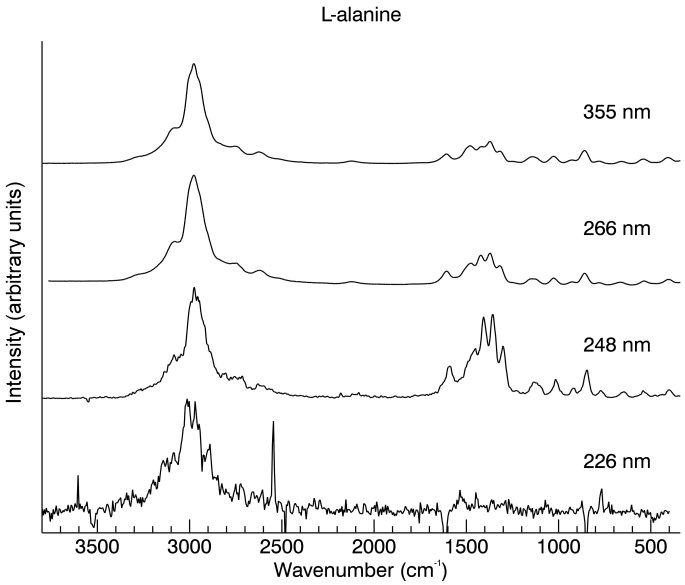

Figure 59: Raman spectrum of l-alanine obtained at various ultraviolet excitation wavelengths, used as a standard for performance as l-alanine exhibits strong Raman scattering at 266 nm.

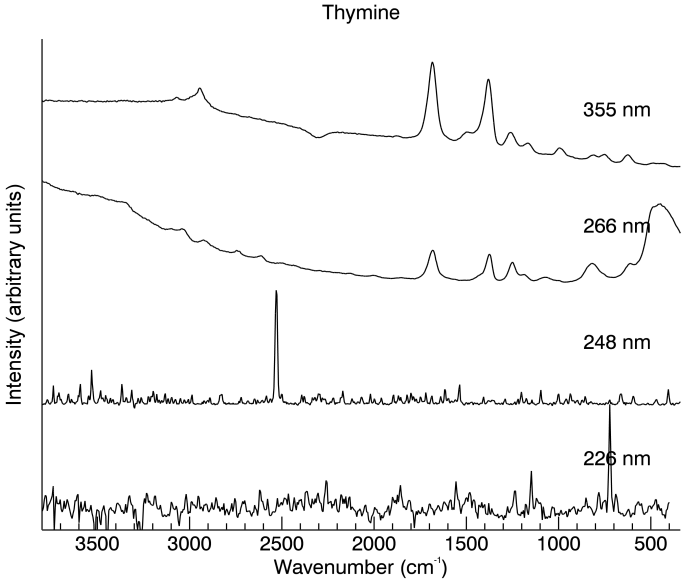

Figure 60: Raman spectrum of thymine obtained at various ultraviolet excitation wavelengths.

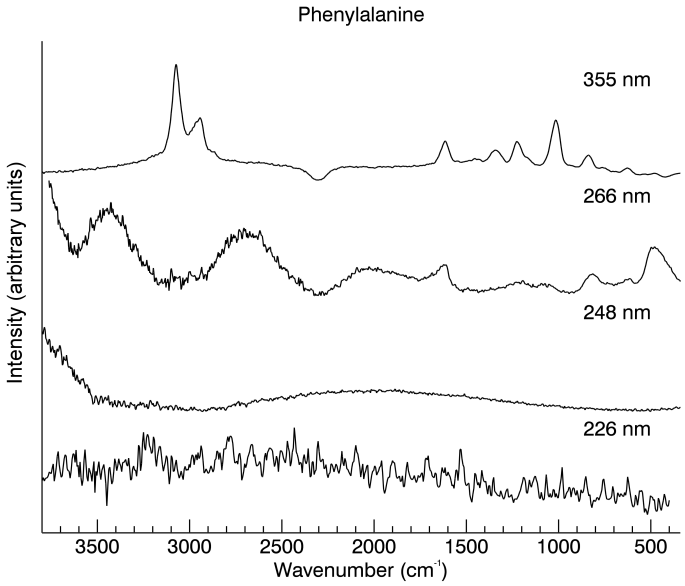

Figure 61: Raman spectrum of phenylalanine obtained at various ultraviolet excitation wavelengths.

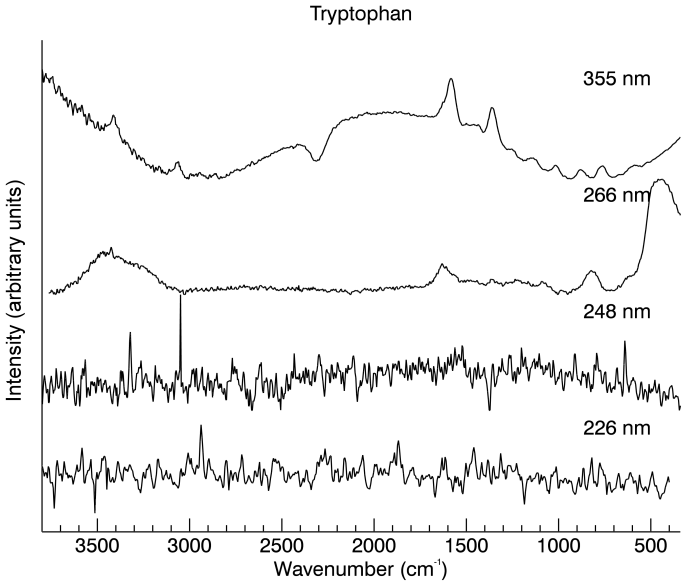

Figure 62: Raman spectrum of tryptophan obtained at various ultraviolet excitation wavelengths.

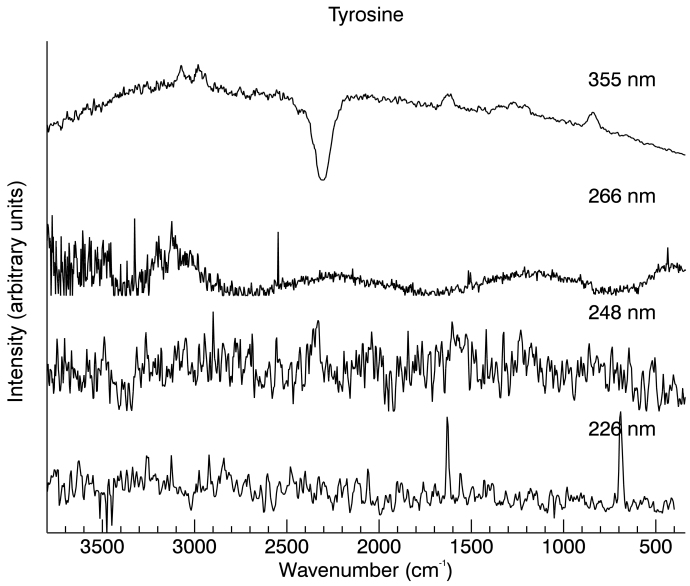

Figure 63: Raman spectrum of tyrosine obtained at various ultraviolet excitation wavelengths.

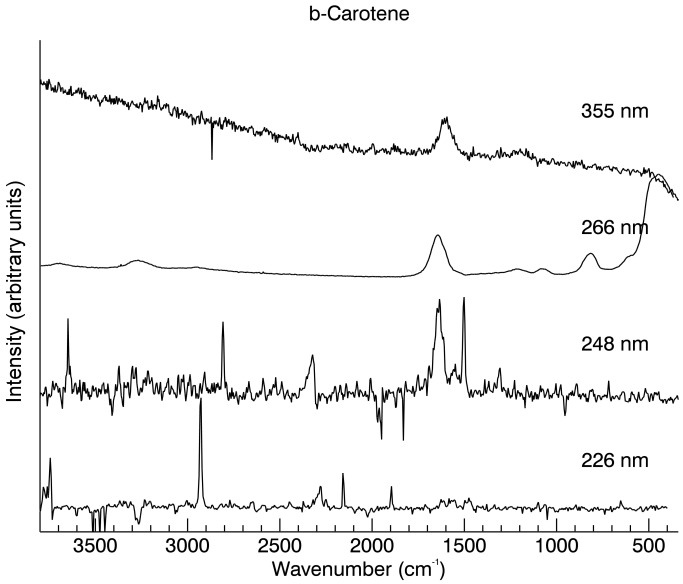

Figure 64: Raman spectrum of b-carotene obtained at various ultraviolet excitation wavelengths.

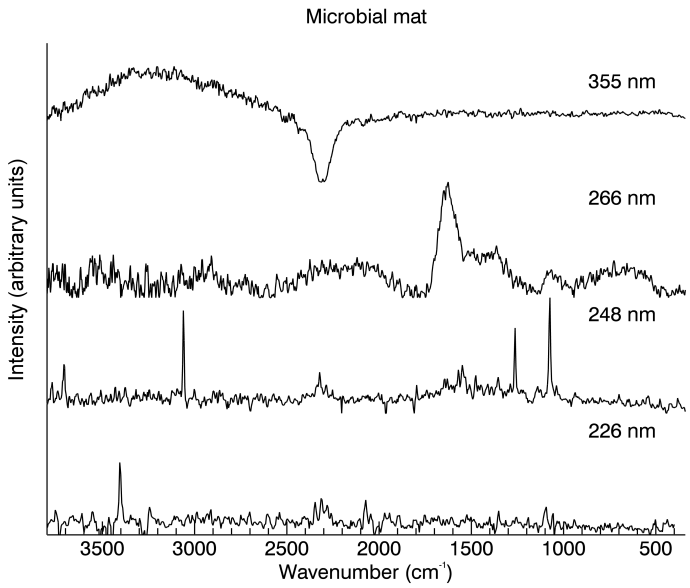

Figure 65: Raman spectrum of microbial mat obtained at various ultraviolet excitation wavelengths.